DOT/FAA/AR-10/23,P2

Air Traffic Organization
NextGen & Operations Planning
Office of Research and
Technology Development
Washington, DC 20591

Explicit Finite Element Modeling of Multilayer Composite Fabric for Gas Turbine Engine Containment Systems, Phase III

Part 2: Arizona State University Fabric Material Tests

January 2011

Final Report

This document is available to the U.S. public through the National Technical Information Services (NTIS), Springfield, Virginia 22161.

This document is also available from the Federal Aviation Administration William J. Hughes Technical Center at actlibrary.tc.faa.gov.

U.S. Department of Transportation
Federal Aviation Administration

NOTICE

This document is disseminated under the sponsorship of the U.S. Department of Transportation in the interest of information exchange. The United States Government assumes no liability for the contents or use thereof. The United States Government does not endorse products or manufacturers. Trade or manufacturer's names appear herein solely because they are considered essential to the objective of this report. The findings and conclusions in this report are those of the author(s) and do not necessarily represent the views of the funding agency. This document does not constitute FAA certification policy. Consult your local FAA aircraft certification office as to its use.

This report is available at the Federal Aviation Administration William J. Hughes Technical Center's Full-Text Technical Reports page: actlibrary.tc.faa.gov in Adobe Acrobat portable document format (PDF).

Technical Report Documentation Page

1. Report No.	2. Government Accession No.	3. Recipient's Catalog No.
DOT/FAA/AR-10/23,P2		

4. Title and Subtitle	5. Report Date
EXPLICIT FINITE ELEMENT MODELING OF MULTILAYER COMPOSITE FABRIC FOR GAS TURBINE ENGINE CONTAINMENT SYSTEMS, PHASE III, PART 2: ARIZONA STATE UNIVERSITY FABRIC MATERIAL TESTS	January 2011
	6. Performing Organization Code
7. Author(s)	8. Performing Organization Report No.
S.D. Rajan, B. Mobasher, Z. Stahlecker, S. Bansal, D. Zhu, M. Morea, and K. Dhandapani	
9. Performing Organization Name and Address	10. Work Unit No. (TRAIS)
Department of Civil and Environmental Engineering Arizona State University Tempe, AZ 85387-5306	
	11. Contract or Grant No. 06-G-007
12. Sponsoring Agency Name and Address	13. Type of Report and Period Covered
U.S. Department of Transportation Federal Aviation Administration Air Traffic Organization NextGen & Operations Planning Office of Research and Technology Development Washington, DC 20591	Final Report
	14. Sponsoring Agency Code ANE-110

15. Supplementary Notes

The Federal Aviation Administration Airport and Aircraft Safety R&D Division Technical Monitor was Donald Altobelli.

16. Abstract

Under a Federal Aviation Administration Grant, sponsored by the Aircraft Catastrophic Failure Prevention Program, a research team consisting of members from Arizona State University (ASU), the National Aeronautics and Space Administration Glenn Research Center, and SRI International collaborated to continue the development of test procedures and computational models for designing and evaluating fabric turbine engine containment structures. This report contains the details of additional tensile tests, including high strain rate tests, and single-yarn pullout tests on Kevlar® that were used to support the development of an ASU material model.

Experiments on quasi-static stress-strain relationship measurements via tensile tests and changes in the microlevel of Kevlar geometry were developed. Yarn-on-yarn interaction properties were also measured using single-yarn pullout tests. The geometrical deformation of a woven fabric swath subjected to direct tensile loading was measured by freezing the deformation of the yarns under an applied strain level using a vacuum impregnation process, followed by a thin sectioning procedure to measure the yard shape. Image processing techniques were used to obtain quantitative measures of the yarn geometry as a function of applied strain. Results indicate that cross-sections of fill and warp yarns undergo significant changes as applied strain is increased.

17. Key Words	18. Distribution Statement
Kevlar, Tensile, Engine containment, Yarn, Pullout, LS-DYNA, Impact, Fabric	This document is available to the U.S. public through the National Technical Information Service (NTIS), Springfield, Virginia 22161. This document is also available from the Federal Aviation Administration William J. Hughes Technical Center at actlibrary.tc.faa.gov.

19. Security Classif. (of this report)	20. Security Classif. (of this page)	21. No. of Pages	22. Price
Unclassified	Unclassified	112	

Form DOT F 1700.7 (8-72) Reproduction of completed page authorized

ACKNOWLEDGEMENTS

The investigators wish to thank Mr. William Emmerling, Mr. Donald Altobelli, and Mr. Chip Queitzsch of the Federal Aviation Administration for their technical and financial support. The authors also relied on technical collaborations with several other organizations, including Honeywell Engines & Systems (Phoenix), SRI International, and the National Aeronautics and Space Administration Glenn Research Center (NASA-GRC). Some of the individuals who contributed to this project included Dr. Jeff Simons of SRI International and Mr. J. M. Pereira of NASA-GRC. Their support and cooperation in meeting the research objectives was greatly appreciated.

TABLE OF CONTENTS

			Page
EXECUTIVE SUMMARY			xv
1.	INTRODUCTION		1
	1.1	Purpose	1
	1.2	Background	1
2.	KEVLAR GEOMETRY AND SINGLE-YARN TENSILE TESTS		3
	2.1	Overview	3
	2.2	Kevlar Geometry Computation	4
		2.2.1 Sample Preparation	5
		2.2.2 Image Analysis	10
	2.3	Kevlar Single-Yarn Tensile Tests	24
		2.3.1 Introduction	24
		2.3.2 Specimen Preparation and Fixture Details	25
		2.3.3 Specimen Test Procedure	26
		2.3.4 Results and Discussion	28
		2.3.5 Weibull Analysis	32
3.	KEVLAR 49 HIGH STRAIN RATE TESTS		34
	3.1	Overview	34
	3.2	High Strain Rate Testing System	36
		3.2.1 The MTS Test Frame	36
		3.2.2 Signal Conditioners and Control Panels	37
		3.2.3 Grip	39
		3.2.4 Force Measurement	39
		3.2.5 Data Acquisition	40
	3.3	Kevlar Fabric	41
		3.3.1 Sample Preparation and Test Setup	41
		3.3.2 Typical Stress-Strain Curve of Kevlar Fabric and Captured Images	42
		3.3.3 Image Analysis of High Strain Rate Test	43
		3.3.4 Kevlar Fabric Test Results and Discussion	47
		3.3.5 Key Parameters	56

3.4 Single Yarn 57

3.4.1 Specimen Preparation and Test Setup 57
3.4.2 Test Results and Discussion 59
3.4.3 Key Parameters Discussion and Summary 64

3.5 Comparison With Published Data 65

4. SINGLE-YARN PULLOUT TEST 66

4.1 Overview 66
4.2 Pullout Test 68

4.2.1 Test Setup 68
4.2.2 Description of Yarn Pullout 69
4.2.3 Test Results and Discussion 72

4.3 Pullout Model and Curve Fitting 80

4.3.1 Analytical Model 80
4.3.2 Pullout Curve Fitting 85

5. CONCLUSIONS AND RECOMMENDATIONS 93

6. REFERENCES 94

LIST OF FIGURES

Figure		Page
1	Microstructure of Woven Kevlar Textile	4
2	Overall Experimental Procedure	5
3	Fine Interstitial Spaces Between Packed Kevlar Filaments Within a Yarn	6
4	Stress-Strain Curve of Kevlar During Test	6
5	(a) Sample Held Under Constant Strain Level, (b) Vacuum Apparatus, (c) Polishing Equipment, (d) Finished Kevlar Samples, (e) Optical Microscopy Equipment, and (f) Typical Kevlar Yarn Model	7
6	Fill Yarn Longitudinal Cross-Section	9
7	Warp Yarn Longitudinal Cross-Section	10
8	Sinusoidal Curve Parameter Estimation	11
9	Cross-Section Approximation Using an Ellipse	11
10	Cross-Section Approximation Using a Square Wave Function	12
11	Comparison of Fill and Warp Cross-Sections (Sinusoidal Curve) at an Undeformed State	12
12	Comparison of Fill Cross-Section (Sinusoidal Curve) at Different Strain Levels	13
13	Fill Cross-Section (Undeformed) Ellipse Curve Fit Through Distribution Point	13
14	Comparison of Fill Cross-Section (Ellipse) at Different Strain Levels	15
15	Comparison of Warp Cross-Section (Ellipse) at Different Strain Levels	17
16	Comparison of Fill and Warp Cross-Sections (Ellipse) at Different Strain Levels	17
17	Fill Cross-Section (Sinusoidal Curve) of Undeformed, 1.0%, 1.5%, and 2.0% Strain Levels	19
18	Fill Yarn Sinusoidal Curve at Undeformed Shape and 2.0% Strain Level	20
19	Comparison of Fill Yarn Cross-Section (Sinusoidal Curve) at Different Strain Levels	20
20	Step Length and Step Height in Warp Yarn at Different Strain Levels	22
21	Comparison of Cross-Sections (Ellipses) of Undeformed Fill and Warp Yarns	23
22	Comparison of Longitudinal Cross-Sections of Undeformed Fill and Warp Yarns	23

23	Model Generation of a Yarn Using Longitudinal and Transverse Geometrical Parameters of Warp Yarn	24
24	Single-Yarn Test Setup	26
25	Single-Yarn Tensile Test	27
26	Stress-Strain Curves for G.L. = 2″, 5″, and 8″	28
27	Stress-Strain Curves for G.L. = 11″, 14″, and 17″	30
28	Comparison of Stress-Strain Curves of Different G.L.s	30
29	Microstructural Scales of Textile, Yarn, and Filament	31
30	Young's Modulus, Ultimate Strength, and Strain at Ultimate Strength vs G.L.	31
31	Comparison of Cumulative Failure Probability vs Peak Stress for Different G.L.s	34
32	High Strain Rate Test System: (a) Actual and (b) Schematic	36
33	(a) MTS Test Machine, (b) Servo Valve, and (c) Slack Adaptor	37
34	(a) MTS FlexTest SE Controller and (b) Personal Computer	37
35	Kistler® 5010B Dual-Mode Charge Amplifier	38
36	High-Rate Control Panel	39
37	Grip Set: (a) Actual and (b) Schematic	39
38	Piezoelectric Force Transducer	40
39	Four-Channel Data Acquisition Card	40
40	Constructed Test Specimens: (a) 2″ and (b) 1″ G.L.s	41
41	High Strain Rate Test Setup	41
42	Four Regions of Stress-Strain Curve Obtained From a Typical Test	42
43	Images of 25-mm G.L. Specimens at a Nominal Strain Rate of 38 s^{-1}	43
44	Specimen Sections: (a) 2″ and (b) 1″ G.L.s	44
45	(a) Maximum Strain of Image Analysis vs Nominal Strain Rate and (b) Correlation of Maximum Strain Between Image Analysis and LVDT Measurement	45
46	Correlation of Strain Rates Between Image Analysis and LVDT Measurement: (a) Strain Rate of Image Analysis vs Nominal Strain Rate and (b) Strain Rate of Image Analysis vs Actual Strain Rate	46

47 Comparison of Stress-Strain Curves Obtained by LVDT and Image Analysis at Nominal Strain Rates of (a) 21 s^{-1}, (b) 68 s^{-1}, (c) 101 s^{-1}, and (d) 170 s^{-1} 47

48 Response of 2″ Fabric at a Strain Rate of 28 s^{-1}: (a) Stress vs Time and (b) Stress vs Strain 48

49 Response of 2″ Fabric at a Strain Rate of 66 s^{-1}: (a) Stress vs Time and (b) Stress vs Strain 48

50 Response of 2″ Fabric at a Strain Rate of 96 s^{-1}: (a) Stress vs Time and (b) Stress vs Strain 49

51 Response of 2″ Fabric at a Strain Rate of 91 s^{-1}: (a) Stress vs Time and (b) Stress vs Strain 50

52 Response of 2″ Fabric at a Strain Rate of 19 s^{-1}: (a) Stress vs Time and (b) Stress vs Strain 51

53 Response of 2″ Fabric at a Strain Rate of 55 s^{-1}: (a) Stress vs Time and (b) Stress vs Strain 52

54 Response of 1″ Fabric at a Strain Rate of 113 s^{-1}: (a) Stress vs Time and (b) Stress vs Strain 53

55 Response of 1″ Fabric at a Strain Rate of 167 s^{-1}: (a) Stress vs Time and (b) Stress vs Strain 54

56 Response of 1″ Fabric at a Strain Rate of 29 s^{-1}: (a) Stress vs Time and (b) Stress vs Strain 55

57 Response of 1″ Fabric at a Strain Rate of 81 s^{-1}: (a) Stress vs Time and (b) Stress vs Strain 55

58 Strain Rate Effect on Dynamic Properties of Kevlar 49 Fabric: (a) Young's Modulus, (b) Tensile Strength, (c) Maximum Strain, and (d) Toughness 57

59 Single-Yarn Specimen: (a) 2″ and (b) 1″ G.L.s 58

60 (a) Stress-Strain Response of a Single Yarn and Identification of Points of Interest and (b) Twisted Yarn Images at a Strain Rate of 45 s^{-1} With a 100-μs Time Interval 59

61 Response of 2″ Single Yarn at a Strain Rate of 21 s^{-1}: (a) Stress vs Time and (b) Stress vs Strain 60

62 Response of 2″ Single Yarn at a Strain Rate of 62 s^{-1}: (a) Stress vs Time and (b) Stress vs Strain 60

63 Response of 1″ Single Yarn at a Strain Rate of 31 s^{-1}: (a) Stress vs Time and (b) Stress vs Strain 62

64 Response of 1″ Single Yarn at a Strain Rate of 47 s^{-1}: (a) Stress vs Time and (b) Stress vs Strain 62

65 Response of 1″ Single Yarn at a Strain Rate of 100 s^{-1}: (a) Stress vs Time and (b) Stress vs Strain 63

66 Strain Rate Effect on Dynamic Properties of Kevlar 49 Single Yarn: (a) Young's Modulus, (b) Tensile Strength, (c) Maximum Strain, and (d) Toughness 65

67 Comparison of Present Study With Literature Data: (a) Young's Modulus, (b) Tensile Strength, (c) Maximum Strain, and (d) Toughness 66

68 Experimental Setup of Yarn Pullout Tests 68

69 Photograph of Experimental Setup for Yarn Pullout Tests 69

70 Yarn Behavior During Pullout 70

71 Representative Single-Yarn Pullout Force vs Displacement Curve 70

72 Comparison of Pullout Force With Transverse Force 71

73 Peak Values of Post-Peak Pullout Force 71

74 Displacement Differences of Adjacent Peaks 72

75 Pullout and Transverse Force vs Displacement Curves of a 2.0″ Specimen 72

76 Pullout and Transverse Force vs Displacement Curves of a 2.5″ Specimen 73

77 Pullout and Transverse Force vs Displacement Curves of a 3.5″ Specimen 73

78 Behavior of a 2.0″ Specimen: (a) Pullout Force vs Displacement Curves and (b) Transverse Force vs Displacement Curves 74

79 Behavior of a 2.5″ Specimen: (a) Pullout Force vs Displacement Curves and (b) Transverse Force vs Displacement Curves 75

80 Behavior of a 3.5″ Specimen: (a) Pullout Force vs Displacement Curves and (b) Transverse Force vs Displacement Curves 75

81 Pullout Force vs Displacement Curves With 27-lb Peak Transverse Force 76

82 Pullout Force vs Displacement Curves With 52-lb Peak Transverse Force 76

83 Pullout Force vs Displacement Curves With 97-lb Peak Transverse Force 77

84 Peak Pullout Force vs Specimen Length 77

85 Peak Pullout Force vs Peak Transverse Force per Yarn 78

86	Peak Pullout Force per Unit Length vs Peak Transverse Force per Yarn	78
87	Energy Needed to Pull the Yarn Out vs Specimen Length	79
88	Energy Needed to Pull the Yarn Out per Unit Length vs Specimen Length	79
89	Pullout-Slip Response and Shear Strength Diagram	80
90	Shear Stress and Force Distribution Along Yarn for (a) Stage I (Uncrimping Stage) and (b) Stage II (Translation Stage)	82
91	Contact Area During Yarn Translation: (a) Contact Area at Different Stages (b) Sinusoidal Function Describing the Contact Area Change During Pullout With Maximum Value A_1 and Minimum Value A_2	84
92	Cross-Section of Kevlar Fabric	84
93	Cross-Section of Warp Yarn	84
94	Shear Stress vs Slip at 27-lb Peak Transverse Force for Different Specimen Lengths	86
95	Shear Stress vs Slip at 52-lb Peak Transverse Force for Different Specimen Lengths	86
96	Shear Stress vs Slip at 97-lb Peak Transverse Force for Different Specimen Lengths	87
97	Shear Stress vs Slip of 2.0″ Specimens at Different Transverse Forces	87
98	Shear Stress vs Slip of 2.5″ Specimens at Different Transverse Forces	88
99	Shear Stress vs Slip of 3.5″ Specimens at Different Transverse Forces	88
100	Maximum Shear Stress vs Specimen Length at Different Transverse Forces	89
101	Friction Shear Stress vs Specimen Length at Different Transverse Forces	89
102	Comparison of Test Data and Simulation for a 2.0″ Specimen	90
103	Comparison of Test Data and Simulation for a 2.5″ Specimen	90
104	Comparison of Test Data and Simulation for a 3.5″ Specimen	91
105	Correlation of Shear Stress and Nominal Shear Stress	91

LIST OF TABLES

Table		Page
1	Fill Direction Ellipse Curve Parameters	14
2	Warp Direction Ellipse Curve Parameters	16
3	Fill Direction Sinusoidal Curve Parameters	18
4	Warp Direction Sinusoidal Curve Parameters	21
5	Single-Yarn Test Plan	28
6	Single-Yarn Test Results	29
7	Single-Yarn Test Data	33
8	Weibull Parameters	33
9	Summary of 2″ Fabric Tests at a Strain Rate of 28 s^{-1}	49
10	Summary of 2″ Fabric Tests at a Strain Rate of 66 s^{-1}	49
11	Summary of 2″ Fabric Tests at a Strain Rate of 96 s^{-1}	50
12	Summary of 2″ Fabric Tests at a Strain Rate of 91 s^{-1}	51
13	Summary of 2″ Fabric Tests at a Strain Rate of 19 s^{-1}	52
14	Summary of 2″ Fabric Tests at a Strain Rate of 55 s^{-1}	53
15	Summary of 1″ Fabric Tests at a Strain Rate of 113 s^{-1}	54
16	Summary of 1″ Fabric Tests at a Strain Rate of 167 s^{-1}	54
17	Summary of 1″ Fabric Tests at a Strain Rate of 29 s^{-1}	56
18	Summary of 1″ Fabric Tests at a Strain Rate of 81 s^{-1}	56
19	Summary of 2″ Single-Yarn Tests at a Strain Rate of 21 s^{-1}	61
20	Summary of 2″ Single-Yarn Tests at a Strain Rate of 62 s^{-1}	61
21	Summary of 1″ Single-Yarn Tests at a Strain Rate of 31 s^{-1}	63
22	Summary of 1″ Single-Yarn Tests at a Strain Rate of 47 s^{-1}	64
23	Summary of 1″ Single-Yarn Tests at a Strain Rate of 100 s^{-1}	64
24	Geometry Parameter for Simulation	85
25	Single-Yarn Pullout Test and Simulation Results	92

LIST OF ACRONYMS

ASU	Arizona State University
D	Denier
FAA	Federal Aviation Administration
FBO	Fan blade-out
FE	Finite element
FEA	Finite element analysis
fps	Frames per second
G.L.	Gage length
LVDT	Linear-velocity differential transformer
MU	Mechanical unit
NASA-GRC	National Aeronautic and Space Administration Glenn Research Center
pC	Picocoulombs
SHTB	Split-Hopkinson tension bar
SEM	Scanning electron microscopy
SRI	SRI International

EXECUTIVE SUMMARY

A team consisting of Arizona State University (ASU), the National Aeronautics and Space Administration Glenn Research Center, and SRI International collaborated to continue development of computational models and verification tests for designing and evaluating turbine engine fan blade fabric containment structures. This phase of the research (Phase III) was conducted under a Federal Aviation Administration (FAA) Grant and was sponsored by the Aircraft Catastrophic Failure Prevention Program. The research was directed toward improving the modeling of a turbine engine fabric containment structure for an engine blade-out containment demonstration test required for certification of aircraft engines.

The first two phases of research yielded both modeling and experimental data characterizing the behavior of fabric materials for engine containment systems. The current study (Phase III) captures the details of the analytical and testing work done in the third phase of the ongoing FAA-sponsored research. Parts 1 and 2 of this report document research conducted through 2009. When Parts 3 and 4 are published, they will supplement Parts 1 and 2 with the results of ongoing work. The following tasks and objectives which correspond to this four-part report.

- Part 1: ASU Material Model and Numerical Simulations—This part of the report uses the knowledge and experimental data from the previous two phases and recent additional tests to develop a constitutive model suitable for implementing in an explicit finite element analysis. This includes relating the changes in stress to the changes in strain, and identifying and quantifying the modes of failure.

- Part 2: Fabric Material Tests—An improved macro model can result from a better understanding of the fabric behavior. The studies include understanding the geometry and behavior of individual yarns both under quasi-static and high strain rate effects, and the yarn-on-yarn interaction.

- Part 3: Improvements in ASU Material Model and Numerical Simulations—This part of the Phase III report will include improvements to the ASU material model based on additional testing and analysis.

- Part 4: Additional Fabric Material Tests—This part of the Phase III report will document additional material tests conducted at ASU that were used to improve the ASU material model.

This report documents Part 2 of 4 in which the experimental Kevlar® 49 fabric tests conducted by ASU are presented. Experiments on quasi-static stress-strain relationship measurements via tensile tests and changes in the microlevel of Kevlar geometry were developed. Yarn-on-yarn interaction properties were also measured using single-yarn pullout tests. The geometrical deformation of a woven fabric swath subjected to direct tensile loading was measured by freezing the deformation of the yarns under an applied strain level using a vacuum impregnation process, followed by a thin sectioning procedure to measure the yarn shape. Image processing techniques were used to obtain quantitative measures of the yarn geometry as a function of applied strain. Results indicate that cross-sections of fill and warp yarns undergo significant changes as applied strain is increased.

The longitudinal geometry of fill and warp yarns was also analyzed and parameters associated with geometry at undeformed and at 1.0%, 1.5%, and 2.0% strain levels were measured.

A literature search was conducted on the quasi-static strength of yarns under dynamic test conditions. A high strain rate servohydraulic tensile test system was developed and the components of the system described. High strain rate tests were conducted on Kevlar 49 fabric and single-yarn specimens at the strain rate range of 20 to 170 s^{-1} for two different gage lengths. The dynamic behavior of the fabric has four distinct regions during loading: crimp region, elastic region, nonlinear failure region, and post-peak region. In the crimp region, where the load essentially straightens the yarns by removing the crimp, the stress-strain graph shows a relatively large increase in strain for a very small increase in load. As the load increased in the elastic region, the straightened yarns took more load and the stress-strain graph exhibited an increased slope. Prior to the ultimate strength, the stress-strain response exhibited nonlinearity due to formation of the localized damage, and a rapid decrease in the stress beyond the ultimate strength that is characteristic of progressive yarn failure was observed.

Yarn slip in fabrics plays an important role in studying the impact of a projectile on a woven ballistic armor or in the forming of a fabric composite. Yarn slip also plays a key role in the concentration of yarn tensions near damaged regions in the fabric and in the propagation of damage. Yarn pullout experiments were conducted using a device that applied a transverse load to the yarn swath during testing.

The energy needed to pull the yarn out was normalized with respect to the specimen length. The specific energy for yarn pullout increased linearly with increasing specimen length at each transverse force. The energy needed to pull yarn out per unit length versus specimen length also experienced the same phenomena. Since the contact area between pulled yarn and fill yarns was not constant during pullout, a functional representation of the contact area was used in the analytical model. Results indicate that both maximum shear stress and friction shear stress increased with increasing transverse force.

1. INTRODUCTION.

1.1 PURPOSE.

This research study captures the details of the analytical work done in the third phase of the ongoing Federal Aviation Administration (FAA)-sponsored research on building a more sophisticated engine containment system model. The purpose of this research is to develop a robust finite element analysis (FEA) modeling methodology for a turbine engine fabric containment system that can benefit the design and certification for commercial aircraft engines.

1.2 BACKGROUND.

Composite fiber fabric wraps are widely used in the containment systems of aircraft gas turbine engines. They provide a cost-effective and lightweight method for mitigating engine debris during a fan blade-out event. These fabrics have a high strength per unit weight compared to the traditional metallic systems and are inexpensive to manufacture. To properly utilize this advantage, it is necessary to have a robust FEA modeling methodology for routine design tasks. Modeling a multilayer fabric composite for engine containment systems during a fan blade-out event has, however, been a difficult task. This report captures the details of the work done in the third phase of the ongoing FAA-sponsored research on building a more sophisticated engine containment system.

In the first phase of this research [1-4], progress was made in addressing the above-mentioned issues. The combined efforts of Honeywell Engines & Systems, SRI International (SRI), the National Aeronautics and Space Administration Glenn Research Center (NASA-GRC), and Arizona State University (ASU) resulted in the following major accomplishments:

- Experimental Characterization of Fabrics. Fabric material models were developed for Kevlar® and Zylon® fabrics. Independent laboratory tests conducted at ASU and SRI form the basis of these models. These material models are general enough to be used as the constitutive model for both static and dynamic/explicit FEAs.

- Static Ring Tests. Static tests of containment wraps subjected to loads through a blunt-nose impactor were conducted at ASU. Ballistic tests of containment wraps subjected to a high-velocity projectile were conducted at NASA-GRC. These tests have provided test cases (benchmark results) to validate the developed finite element (FE) methodology.

- FE Material Model Development. The material models were used by the research team in the FE simulation of static and ballistic tests. The static test results have been validated by ASU using the ABAQUS® FE program. The ballistic test results were validated by Honeywell and SRI, using the LS-DYNA® FE program.

- Engine Fan Blade-Out (FBO) Simulation. The knowledge gained from previous tasks was used by Honeywell for the numerical simulation of engine FBO events involving existing production engine models and compared against test results (employing Kevlar containment).

- Kevlar-Zylon Comparison. An understanding was reached of the relative comparison between Kevlar and Zylon materials in turbine engine FBO containment systems.

The second phase of research [2, 5, 6, and 7] brought a new level of capability to design and develop fan containment systems for turbine engines, thereby leading to more economical and safer containment system designs, such as the following.

- Robust FE Model Development. Improvements were made to the material models for 1420-Denier (D) Kevlar 49 17x17 weave (Kevlar) and 500-D Zylon AS 35x35 weave (Zylon), and thereby increased confidence that these models and methodologies can accurately predict design conditions.

- Improved FE Modeling Capability for Multilayer Fabric. In the Phase I program, most of the LS-DYNA models used a single element through the thickness to model the fabric, which ranged from 1 to 24 layers. Although this technique is simple, it did not provide the predictive capability of computing the number of fabric layers that are penetrated during a containment event. Therefore, the containment margin in terms of the number of unpenetrated layers versus the total number of layers cannot be accurately predicted. Multilayer models where multiple layers of fabric modeled using multiple layers of shell elements were developed to give a better understanding of fabrics used in containment systems.

- 1500-D Zylon Material Characterization. In the previous program, limited ballistic and static tests of 1500-D Zylon (17x17 weave) indicated that 1500-D Zylon has the potential to offer a 60% weight advantage over Kevlar for the same fragment energy. 1500-D Zylon enables a dramatic increase in fan containment safety margin, a decrease in engine weight, or a combination of both. Experiments were performed to find the basic material properties of 1500-D Zylon.

- Engine Simulations. As in the previous phase, FE simulations were performed to validate improvements to the material models and methods developed under this program as they relate to propulsion engine FBO containment. Fabric material models and modeling methods and improvements to the material models and methods were validated using fan containment test data.

The first two phases of research yielded experimental techniques and data, which characterize the behavior of fabric materials, especially Kevlar, for engine containment systems. Phase III of the research has the following tasks and objectives using 1420-D, 17x17 weave, Kevlar 49 fabric:

- Rational Development of Constitutive Model for Explicit FEA. The aim is to use the knowledge and experimental data from the previous two phases and develop a constitutive model suitable for implementing in an explicit FEA. This includes relating the changes in stress to the changes in strain, and identifying and quantifying the modes of failure.

- Experimental Techniques to Improve the Understanding of Fabric Behavior. An improved macro model can result from a better understanding of the fabric behavior. The studies include understanding the geometry and behavior of individual yarns both under quasi-static and high strain rate effects, and the yarn-on-yarn interaction.

The Kevlar geometry and the experimental procedure to find the basic (quasi-static) stress-strain relationship via tensile tests are discussed in section 2. In section 3, the test procedure for finding the strain rate-dependent tensile properties is detailed. Both single-yarn and fabric swath properties are obtained. The characterization of yarn properties continues in section 4 where yarn-on-yarn interaction properties are examined via single-yarn pullout tests.

2. KEVLAR GEOMETRY AND SINGLE-YARN TENSILE TESTS.

The properties of a single Kevlar 49 yarn from a woven fabric are discussed in this section. A single yarn contains hundreds of filaments and forms the basic building block of the Kevlar fabric. The methodology used to characterize the single yarn is general enough to be applicable to other fabric materials and types.

2.1 OVERVIEW.

To properly characterize the deformation patterns in a textile material and develop an explicit model of the individual yarn behavior in a woven fabric, the size, shape, and relative locations of the yarns in the fabric need to be verified as a function of the applied strain. This report presents an experimental procedure to characterize the geometrical deformation of woven fabric yarns as they are subjected to direct tensile loading. An experimental procedure was developed to capture the geometry of a 17x17 woven Kevlar 49 fabric both in undeformed and deformed states. The undeformed geometry of Kevlar is shown in figure 1. The procedure involved loading a fabric swath in tension and freezing the displacement by gluing the fabric yarns while under the applied strain level. A vacuum impregnation process was employed to make an impregnated solid out of the woven yarn. Thin sectioning and polishing of the sample was conducted in both the warp and fill directions, and the cross-sections were observed under both optical microscopy and scanning electron microscopy (SEM). By applying image processing techniques, quantitative measures of the geometry of the yarns were obtained as a function of the applied strain. The quantitative data was used to better calibrate the constitutive models used, such as FE models, at the single-yarn level. This procedure can also be applied to characterize the deformations that take place as yarns are subjected to biaxial and shear loads.

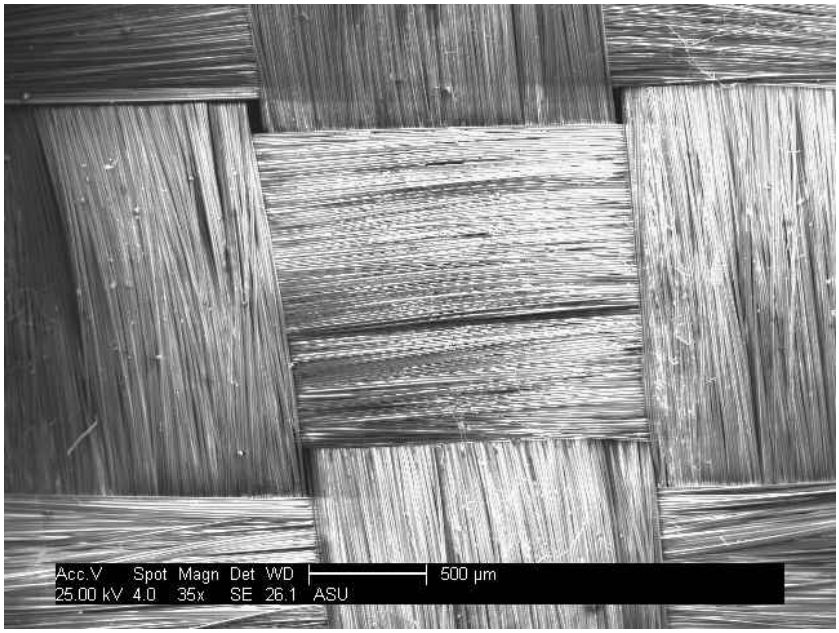

Figure 1. Microstructure of Woven Kevlar Textile

2.2 KEVLAR GEOMETRY COMPUTATION.

The schematic diagram of the experimental procedure for sample preparation and imaging Kevlar is shown in figure 2. Since it is difficult to cut a section of fabric without unraveling the filaments near the cut, a procedure was adopted to capture the geometry of the fabric consisting of several distinct steps. The samples were first loaded in tension up to a predefined strain level and held under this strain level while cyanoacrylate-based adhesive (KrazyGlue®) was applied to the samples and clamped through the thickness to restrain the geometry in this condition by freezing the displacement. The specimens were then removed from the test machine, sectioned into smaller pieces, and potted into low-viscosity epoxy (EPOTEK 301® made by Epoxy Technologies, Billerica, MA) under a vacuum chamber to impregnate the fabric with epoxy. After the epoxy had set, sections perpendicular to the warp and the fill yarns were obtained using a diamond-blade saw. Samples were polished using a variable-speed polisher, and images were taken using optical microscopy. Calibration procedures were conducted to verify the geometrical parameters and the scale of the features observed at the predetermined strain level. The details of these steps are described in following sections.

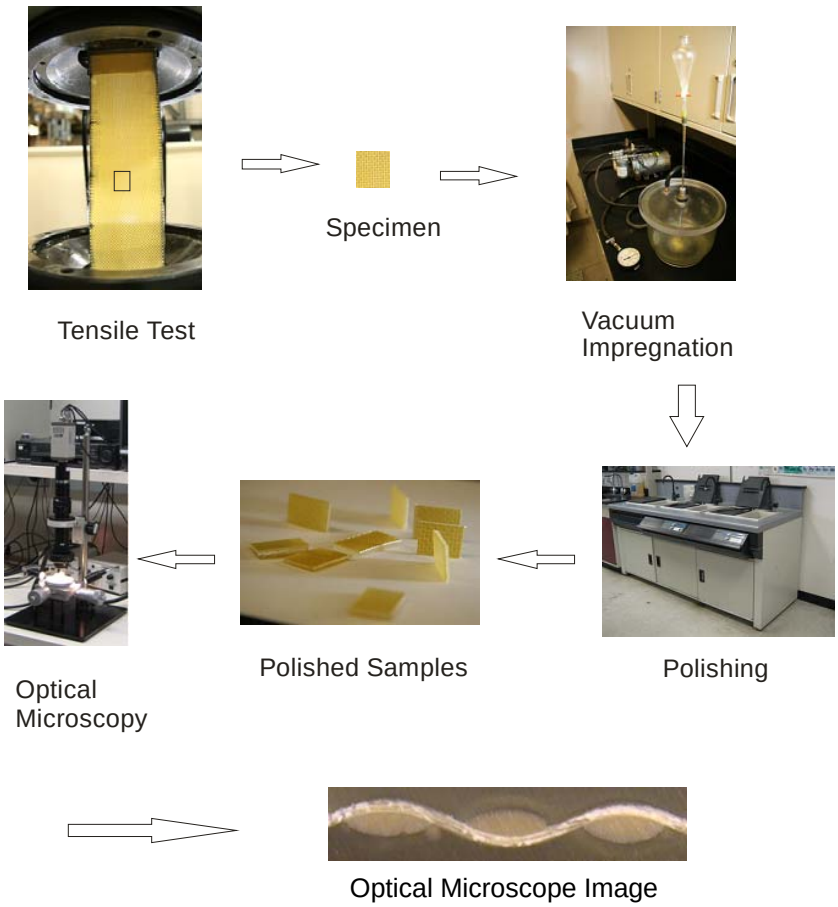

Figure 2. Overall Experimental Procedure

2.2.1 Sample Preparation.

Figure 3 shows an SEM photomicrograph of the Kevlar 49 filaments and their interstitial spaces. It is known that the filaments frictionally slip past one another as a function of applied strain, resulting in substantial changes in the general shape of the yarns. To capture the effect of loading on the geometry of the Kevlar, samples were loaded to three different strain levels. These strain levels were 1.0%, 1.5%, and 2.0%. The loading history is shown in figure 4. Tensile samples were 2.5″ by 10″ in size, and tests were conducted in displacement control condition with a stroke movement of 0.05 in/min while the samples were loaded up to the specified stain levels. At each designated strain level, the samples were held under constant load while a vice grip was clamped on the surface of the specimen to ensure a constant strain level during sample preparation. The surfaces of the vice grips were equipped with two flat Teflon® tapes with a low-viscosity, two-part epoxy smeared on their surfaces. Clamping the two sides of the specimen while under load allowed the epoxy to penetrate in between the interstitial spaces of the individual filaments. After the epoxy had set, the load was removed, and several smaller samples were obtained (approximately 2″ by 1.5″). These samples were subjected to vacuum impregnation using a low-viscosity epoxy (EPOTEK 301). Several control specimens were also selected from the stock material in an unstrained condition. These samples were also subjected to vacuum impregnation.

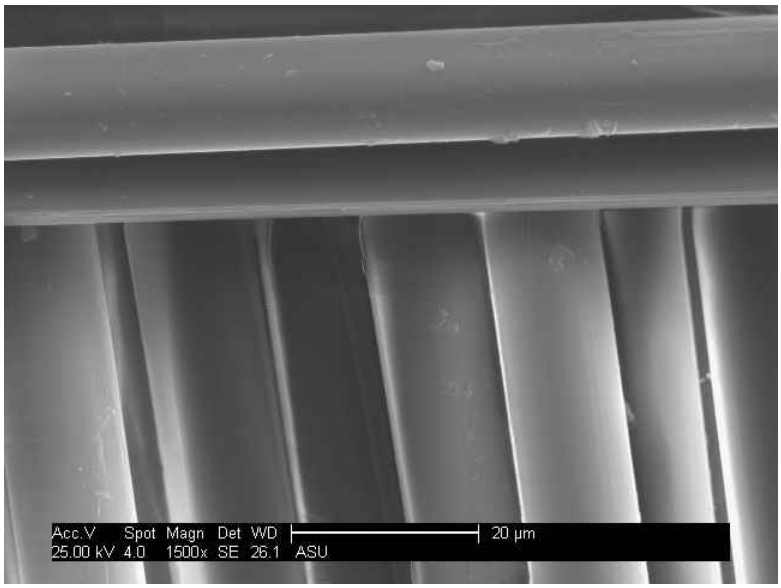

Figure 3. Fine Interstitial Spaces Between Packed Kevlar Filaments Within a Yarn

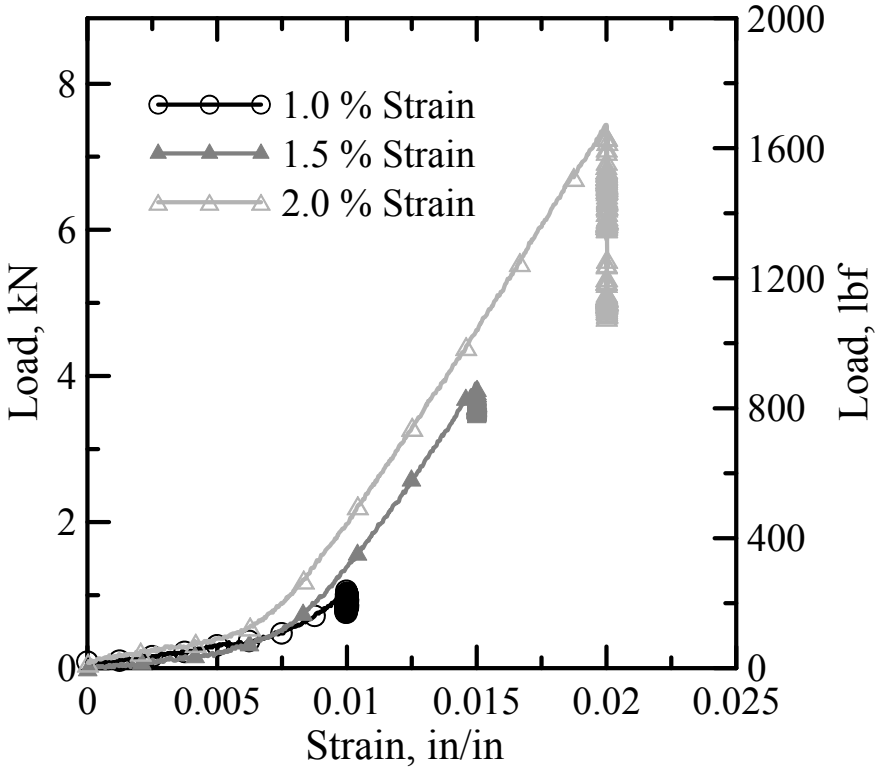

Figure 4. Stress-Strain Curve of Kevlar During Test

To avoid re-orientation of the yarns during sample unloading, several layers of glue were applied on both sides of the sample during a 15-minute interval under load. The hardened glue restricted the yarns from re-orientation during unloading. After the sample was removed from the test machine, the glued portions were cut and potted in the epoxy. Figure 5(a) shows the Kevlar

specimen during the test. The samples were then subjected to a constant vacuum of 25 inHg (-85 KPa) for 1 hour, followed by a 24-hour epoxy curing period. The vacuum apparatus is shown in figure 5(b).

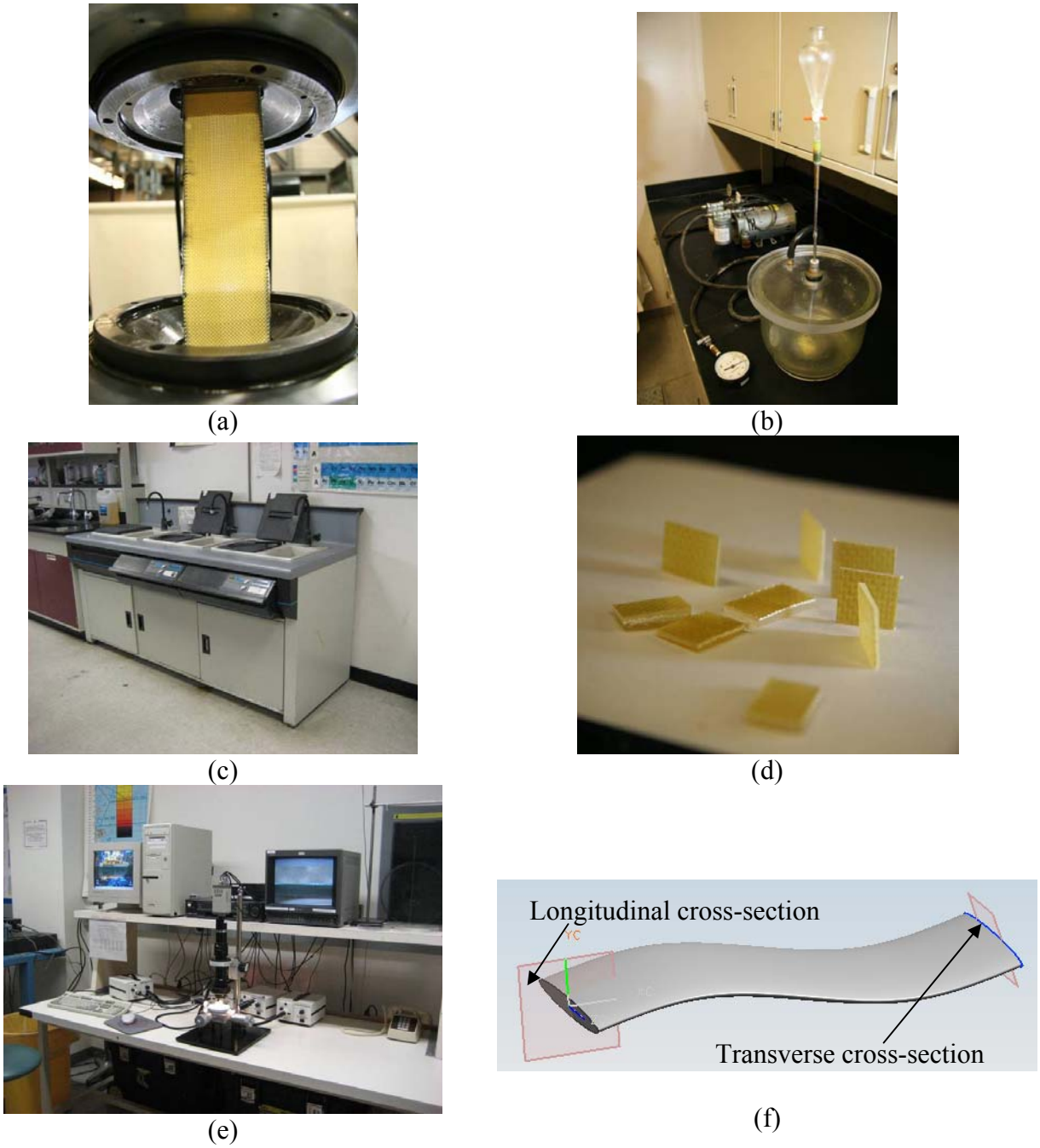

Figure 5. (a) Sample Held Under Constant Strain Level, (b) Vacuum Apparatus, (c) Polishing Equipment, (d) Finished Kevlar Samples, (e) Optical Microscopy Equipment, and (f) Typical Kevlar Yarn Model

Using a slow-speed, diamond-blade circular saw, the samples were sectioned into rectangular shapes with the long side representing the warp direction and the short side representing the fill direction. The edges were cut as parallel to yarns as possible. After sectioning, the samples were polished in two stages using a silicon carbide paper P#800 followed by a 1-micron polishing paper. The polishing machine is shown in figure 5(c). The finished samples are shown in figure 5(d).

Images of the polished sample cross-sections were taken by optical microscopy, as shown in figure 5(e). Image magnification was determined using the "image of an engineering scale" scanned at the same microscope settings. Figure 5(f) shows the transverse and longitudinal cuts used to perform the section analysis.

Figure 6(a-d) shows the longitudinal cross-section of fill yarn under different strain levels, and figure 7(a-d) shows the longitudinal cross-section of warp yarn under different strain levels. It is evident that both the fill and warp yarns can be represented as having elliptical cross-sections along their transverse cross-section and sinusoidal curves along the longitudinal cross-section.

As shown in figures 6 and 7, the cross-sections of fill and warp yarns undergo significant changes as an increasing strain level is applied. Images at increasing strain levels indicate that the fibers along the loaded direction (warp) straighten out, while the yarns in the perpendicular direction (fill) become wavier. The fill yarn waviness increases as the strain level increases, while the warp yarns assume a saw-tooth shape with an increasing strain level. The cross-section of the warp yarns convert from an elliptical shape to a more circular form, while the cross-section of fill yarns becomes flatter and distributes over the entire length of the warp yarns. At a strain of 2%, the warp yarns are completely covered by the fill yarns in a periodic support, as shown in figure 7(d). These deformations represent an increasing contact pressure between the two perpendicular yarns. The magnitude of these pressures are unknown at this point; however, it is expected that through proper calibration and FE modeling, a better understanding of these inter-yarn pressures may be obtained.

A qualitative image analysis was conducted to analyze the images and characterize the deformation patterns. The initial yarn cross-section for both the warp and fill directions were approximated as an ellipse in the cross-section, while the length of the yarn was projected to follow a sinusoidal curve. The parameters associated with these curves are estimated by fitting sinusoidal and elliptical curves to the cross-sections using the least square method. Several MATLAB® programs were written for curve-fitting procedures to capture the points along the curve and estimate its parameters. Furthermore, as the samples were loaded, the warp yarns straighten once crimp was removed and could no longer be approximated using a sinusoidal curve. The interfacial pressure between fill and warp yarns prohibits the warp yarns from completely straightening out, hence dips/valleys form, with dips at the location of fill yarns and valleys in between the fill yarns. This characteristic response was approximated using a step function. Warp yarns under high strain levels were fitted using step functions instead of sinusoidal curves. Parameters were computed separately for each sample at each strain level. The overall or average parameters were computed by fitting a single curve through all the selected points from different samples at a strain level.

(a) Undeformed Geometry

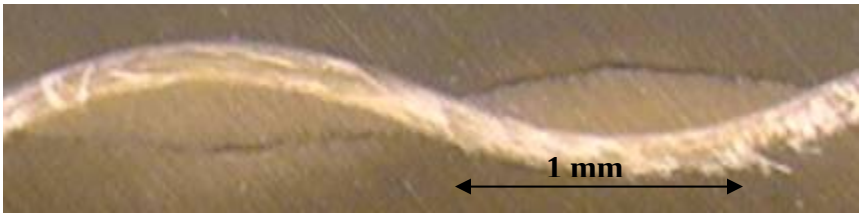

(b) Under 1.0% Strain Level

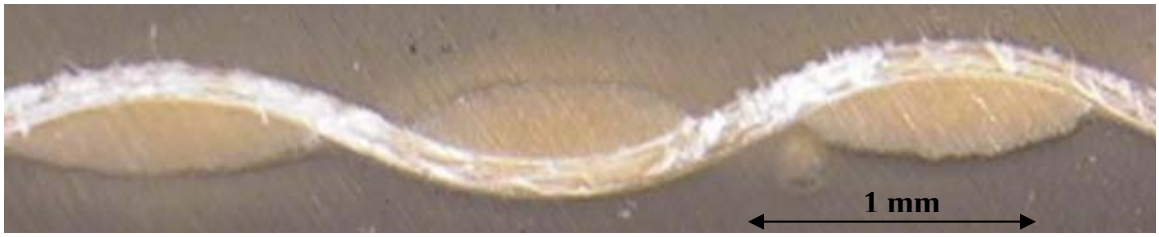

(c) Under 1.5% Strain Level

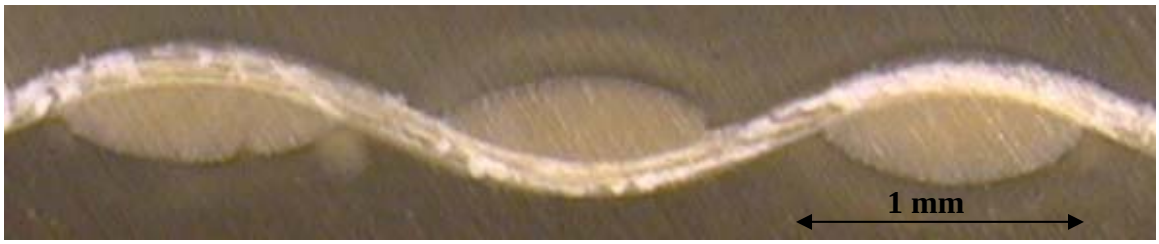

(d) Under 2.0% Strain Level

Figure 6. Fill Yarn Longitudinal Cross-Section

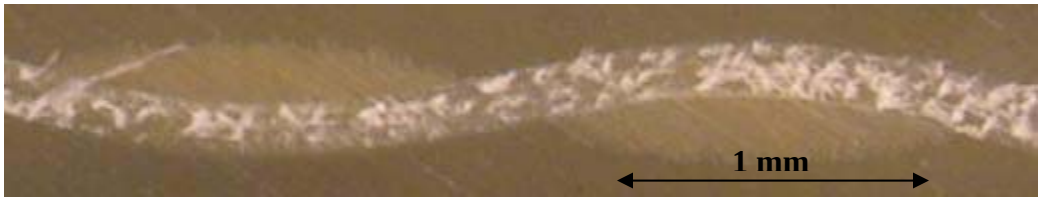

(a) Undeformed Geometry

(b) Under 1.0% Strain Level

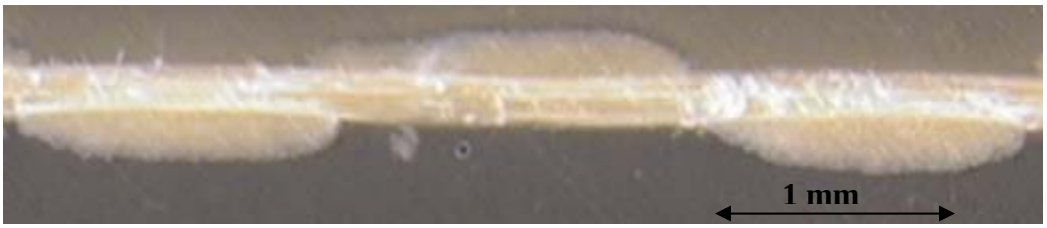

(c) Under 1.5% Strain Level

(d) Under 2.0% Strain Level

Figure 7. Warp Yarn Longitudinal Cross-Section

2.2.2 Image Analysis.

A general equation of a sinusoidal curve is given by

$$f(x) = A\sin(Bx + C) + D + Ex \tag{1}$$

where parameter A represents the amplitude, B is frequency, C is phase shift, D is the rigid-body shift along the y direction, and E is the slope of the baseline of the sinusoidal curve along the horizontal direction. The amplitude and frequency are the only parameters of interest in the approach since the other parameters correspond to rigid-body motion and the relative location of the image with respect to the starting point of the curve along the yarn length. Figure 8

represents a fill yarn in a fabric with the warp yarns under load. The sinusoidal curve (shown in black) represents the least square fit to this curve.

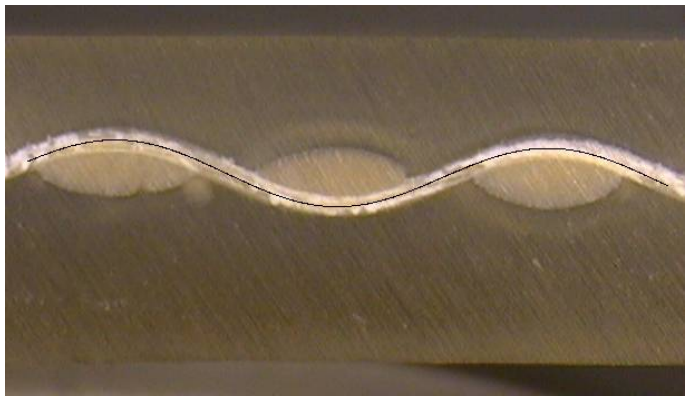

Figure 8. Sinusoidal Curve Parameter Estimation

To estimate sinusoidal curve parameters with better accuracy, a number of samples were prepared for each fill and warp direction at different strain levels. Points along the sinusoidal curve were selected using a MATLAB program, and the sinusoidal curve parameters were estimated. Points along an ellipse were also used in a curve-fit program for ellipsoidal sections. Similar to the sinusoidal curve fitting, the yarn cross-section was estimated by an elliptical approximation. The general equation of the ellipse in polar coordinates is given by

$$r = \frac{ab}{\sqrt{a^2 \sin^2 \theta + b^2 \cos^2 \theta}} \tag{2}$$

where r is the radius (distance of point from center), and θ is the independent variable representing the angle between the semi-major axis and a point on the circumference, a is the semi-major axis, and b is the semi-minor axis. Figure 9 shows all the selected points and fitted curve for the undeformed geometry of fill yarn. This procedure was repeated for every sample. To compute overall or average parameters, the selected points were plotted on a common scale, and a single sinusoidal curve fitting was performed.

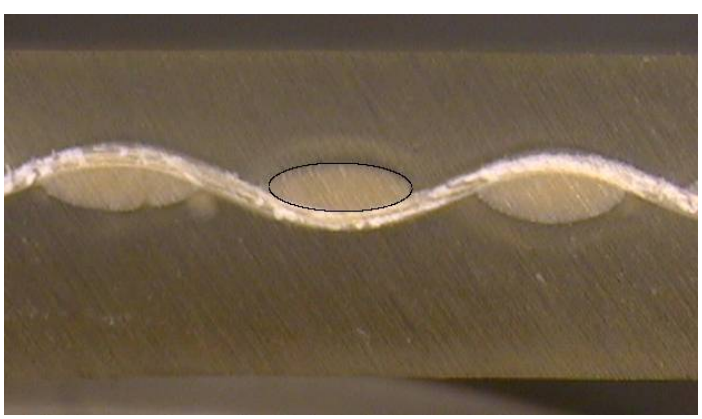

Figure 9. Cross-Section Approximation Using an Ellipse

The warp yarns under load can be approximated using a square wave function, as shown in figure 10. Since the square wave function is small and gets smaller as the load/strain level increases, it becomes increasingly difficult to fit a step function through the selected curves. Therefore, instead of fitting a step function as a single function in the curve, two straight lines were fitted through the selected points on the warp yarns. The distance between these two lines was taken as step height.

Figure 10. Cross-Section Approximation Using a Square Wave Function

Figure 11 compares the undeformed geometry of the fill and warp cross-sections (sinusoidal curve). Note that the fill yarns have a higher degree of waviness than the warp yarns. The effect of strain levels on the transverse geometry of the fill yarns is shown in figure 12. Note that, as the strain is increased, the fill yarn's curvature increases and the wavelength of the curves decreases.

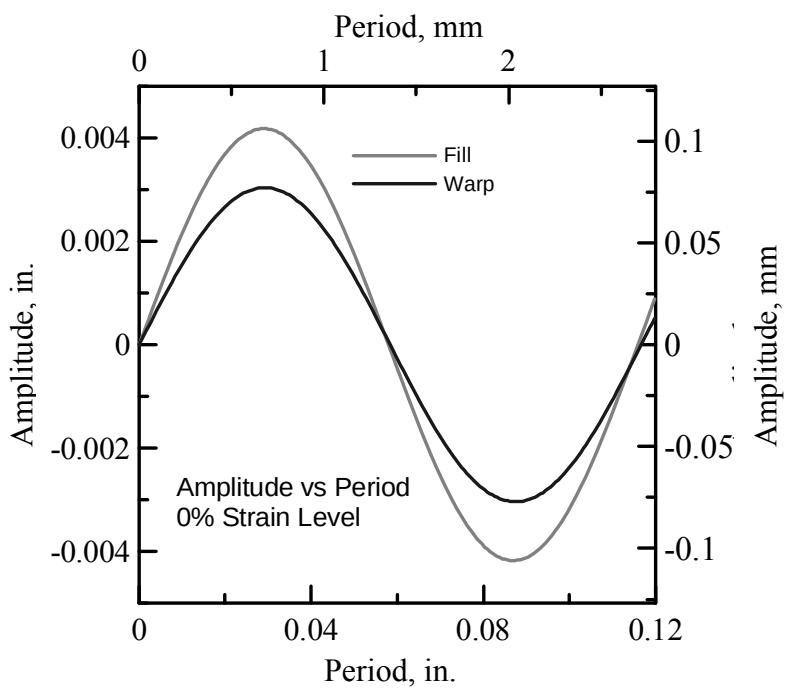

Figure 11. Comparison of Fill and Warp Cross-Sections (Sinusoidal Curve) at an Undeformed State

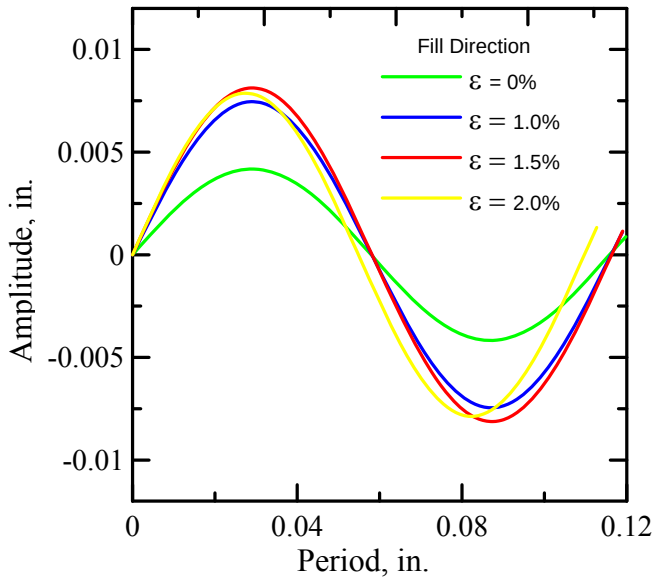

Figure 12. Comparison of Fill Cross-Section (Sinusoidal Curve) at Different Strain Levels

2.2.2.1 Fill Yarns—Transverse Cross-Section (Ellipse).

Images of Kevlar yarns, taken using optical microscopy, were used to estimate the geometrical parameters for fill and warp yarns for undeformed samples as well as 1.0%, 1.5%, and 2.0% strained samples. Figure 13 represents a typical distribution of points of the cross-section of a fill yarn. The sample is in an undeformed stage. The parameters of the curve fit can be obtained and used to generate a best-fit curve, as shown in the figure. The parameters for undeformed samples can be further used to generate a micromechanical model of the fabric. Parameters associated with transverse cross-section (elliptical) of fill yarns are presented in table 1.

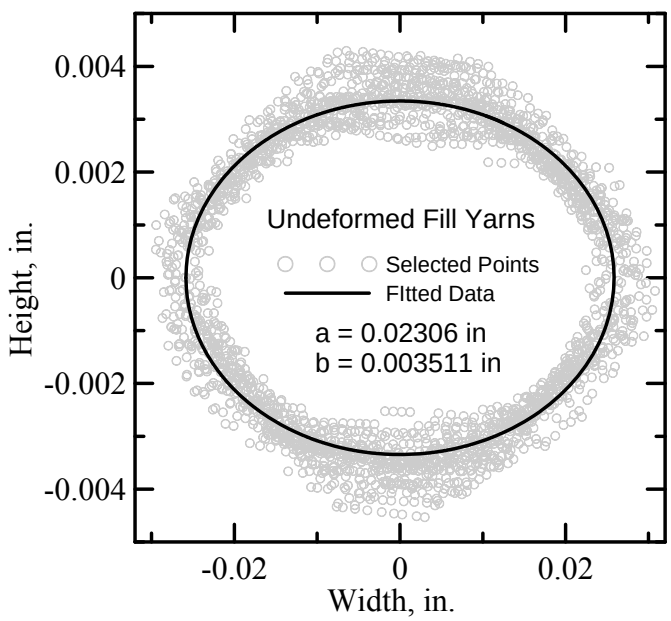

Figure 13. Fill Cross-Section (Undeformed) Ellipse Curve Fit Through Distribution Point

Table 1 summarizes the semi-major and semi-minor axis (*a* and *b*) parameters associated with the fill yarns for all samples at different strain (ε) levels. As the strain level increases, the ratio of semi-major to semi-minor axis increases, indicating that the yarns flatten with increasing strain level. This phenomenon can also be observed in figure 10.

Table 1. Fill Direction Ellipse Curve Parameters

Replicate No.	ε = 0.0%		ε = 1.0%		ε = 1.5%		ε = 2.0%	
	a (in.)	*b* (in.)	*a* (in.)	*b* (in.)	*a* (in.)	*b* (in.)	*a* (in.)	*b* (in.)
1	0.0245	0.0038	0.0249	0.0043	0.0295	0.0046	0.0289	0.0043
2	0.0237	0.0038	0.0274	0.0040	0.0284	0.0045	0.0300	0.0050
3	0.0238	0.0037	0.0266	0.0037	0.0255	0.0052	0.0293	0.0036
4	0.0241	0.0035	0.0299	0.0039	0.0316	0.0047	0.0313	0.0038
5	0.0245	0.0038	0.0268	0.0044	0.0339	0.0043	0.0318	0.0039
6	0.0246	0.0035	0.0264	0.0046	0.0306	0.0047	0.0314	0.0036
7	0.0237	0.0035	0.0285	0.0039	0.0323	0.0042	0.0329	0.0034
8	0.0228	0.0038	0.0253	0.0040	0.0258	0.0049	0.0263	0.0039
9	0.0233	0.0036	0.0291	0.0036	0.0317	0.0043	0.0282	0.0039
10	0.0231	0.0037	0.0262	0.0040	0.0300	0.0044	0.0294	0.0039
11	0.0236	0.0036	0.0308	0.0040	0.0283	0.0047	0.0294	0.0033
12	0.0221	0.0036	0.0241	0.0045	0.0343	0.0039	0.0266	0.0038
13	0.0240	0.0037	0.0247	0.0050	0.0256	0.0058	0.0263	0.0039
14	0.0224	0.0035	0.0285	0.0050	0.0308	0.0042	0.0270	0.0037
15	0.0242	0.0035	0.0219	0.0045	0.0313	0.0048	0.0272	0.0041
16	0.0231	0.0034	0.0259	0.0051	0.0248	0.0043	0.0299	0.0035
17	0.0242	0.0036	0.0260	0.0052	0.0236	0.0047	0.0297	0.0041
18	0.0226	0.0036	0.0248	0.0049	0.0259	0.0040	0.0260	0.0051
19	0.0236	0.0036	0.0268	0.0047	0.0226	0.0048	0.0296	0.0044
20	0.0238	0.0037	0.0242	0.0043	0.0225	0.0047	0.0302	0.0036
Average	0.0236	0.0036	0.0264	0.0044	0.0285	0.0046	0.0291	0.0039
Standard deviation	0.0007	0.0001	0.0027	0.0005	0.0037	0.0004	0.002	0.0001
Parameter computed using point cloud	0.0231	0.0035	0.0264	0.0044	0.0281	0.0046	0.0288	0.0040

Figure 14 shows the effect of strain on the semi-major and semi-minor axes of the fill yarns. The semi-major axis of yarns increases with increasing strain level. Figure 14 also indicates that the increase in the semi-major axis rises to about 1.5%, and remains relatively constant beyond this level. The semi-minor axis of the fill yarns increases as the strain level increases. This means the fill yarn density reduces or the voids between fibers increase. Further, since the fill yarns become flat or more rectangular in the cross-section under load, the approximation of the transverse cross-section with an ellipse also added some error in the estimation. The equation of the fitted curve describing the strain effect on the yarn geometry as represented by the semi-major and semi-minor axes can be represented by equation 3.

$$a = 0.289\,\varepsilon + 0.0235$$
$$b = 0.0035 + 0.17\,\varepsilon - 7.32\,\varepsilon^2 \qquad (3)$$

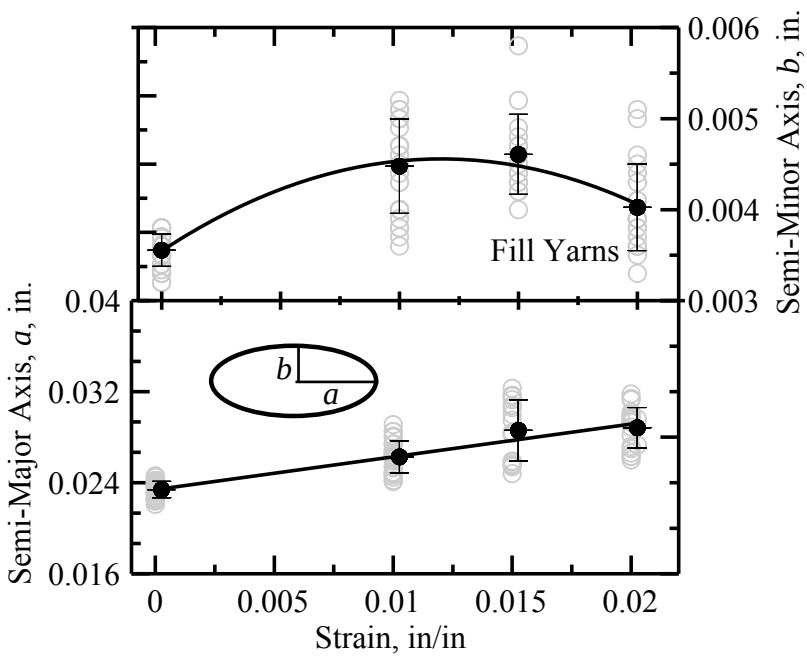

Figure 14. Comparison of Fill Cross-Section (Ellipse) at Different Strain Levels

2.2.2.2 Warp Yarns—Transverse Cross-Section (Ellipse).

Table 2 summarizes the parameters of the warp yarns for various loading conditions. The semi-major axis (*a*) and semi-minor axis (*b*) are shown for all samples at different strain levels. As the strain level increases, the semi-major axis of warp yarns decreases while the semi-minor axis increases. This means the yarns become more circular with increasing strain. This phenomenon can also be observed in figure 8.

Table 2. Warp Direction Ellipse Curve Parameters

Sample No.	0.0% Strain Level		1.0% Strain Level		1.5% Strain Level		2.0% Strain Level	
	a (in.)	*b* (in.)	*a* (in.)	*b* (in.)	*a* (in.)	*b* (in.)	*a* (in.)	*b* (in.)
1	0.0235	0.0034	0.0232	0.0041	0.0198	0.0054	0.0178	0.0063
2	0.0256	0.003	0.0209	0.0042	0.0216	0.0049	0.0192	0.0055
3	0.0234	0.0037	0.0224	0.0042	0.0198	0.0056	0.0194	0.0063
4	0.0246	0.0036	0.0216	0.0041	0.0201	0.0054	0.019	0.0065
5	0.0262	0.0032	0.0228	0.0044	0.0194	0.0054	0.0178	0.006
6	0.0255	0.0034	0.0216	0.0041	0.0205	0.0055	0.0198	0.0051
7	0.0275	0.0029	0.0217	0.004	0.0195	0.0058	0.019	0.0051
8	0.0253	0.0035	0.0215	0.0041	0.0206	0.0054	0.0174	0.0058
9	0.0276	0.003	0.0213	0.0044	0.0207	0.0046	0.0181	0.0055
10	0.0237	0.0034	0.0224	0.0045	0.0205	0.0056	0.0188	0.0054
11	0.0277	0.003	0.0211	0.0045	0.0209	0.0053	0.0181	0.0056
12	0.0238	0.0033	0.021	0.0041	0.0201	0.0059		
13	0.0278	0.003	0.0228	0.0044	0.0197	0.0058		
14	0.0241	0.0035	0.0223	0.0043	0.0202	0.0051		
15	0.0282	0.0032	0.0213	0.0043	0.0202	0.0056		
16	0.0268	0.0033	0.0219	0.0047	0.0216	0.0057		
17	0.0282	0.0031	0.0227	0.0045	0.0199	0.006		
18	0.0262	0.0036	0.0209	0.0044	0.021	0.0058		
19	0.0241	0.0036	0.0206	0.0046	0.0213	0.0057		
20	0.024	0.0033	0.0225	0.0043	0.0213	0.0056		
Average	0.02557	0.00330	0.02176	0.00432	0.02036	0.00547	0.01858	0.00574
Standard deviation	0.00177	0.00024	0.00080	0.00019	0.00075	0.00037	0.00078	0.00048
Parameters computed using point cloud	0.025847	0.003345	0.02192	0.00432	0.02040	0.00541	0.01860	0.00571

Figure 15 shows the effect of strain on the semi-major and semi-minor axes of the warp yarns. The semi-major axis of yarns decreases with an increase in the strain level. It is interesting to note that the effect of the loading on the semi-major axis can be represented by linear curve. The semi-minor axis of the warp yarns increases as the strain level increases. The effect of strain on the semi-major and semi-minor axes (all units in inches) can be represented by equation 4.

$$\begin{aligned} a &= -0.364\,\varepsilon + 0.02572 \\ b &= 0.124\,\varepsilon + 0.0033 \end{aligned} \tag{4}$$

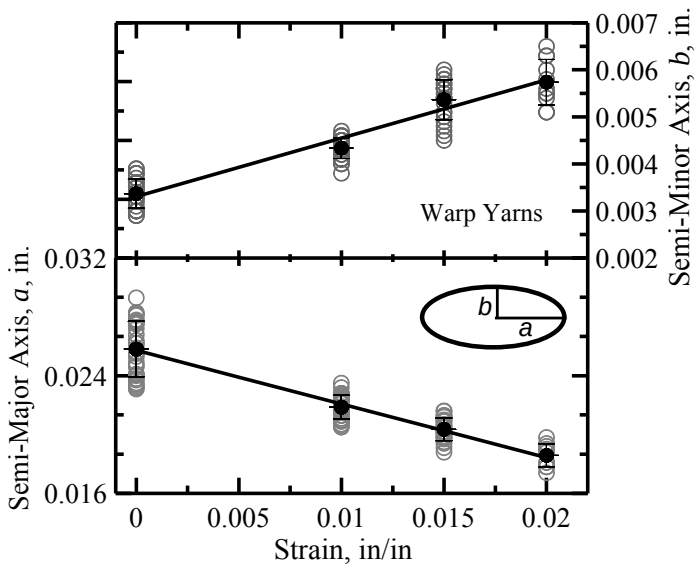

Figure 15. Comparison of Warp Cross-Section (Ellipse) at Different Strain Levels

Figure 16 shows the gradual change in the shape of the fill and warp yarns' cross-sections under loading. As the strain level increases, the yarn's semi-major axis increases significantly while there is little increase in the semi-minor axis, indicating that the yarns become sparser with a decrease in the density of the fill yarns as the warp yarns are loaded.

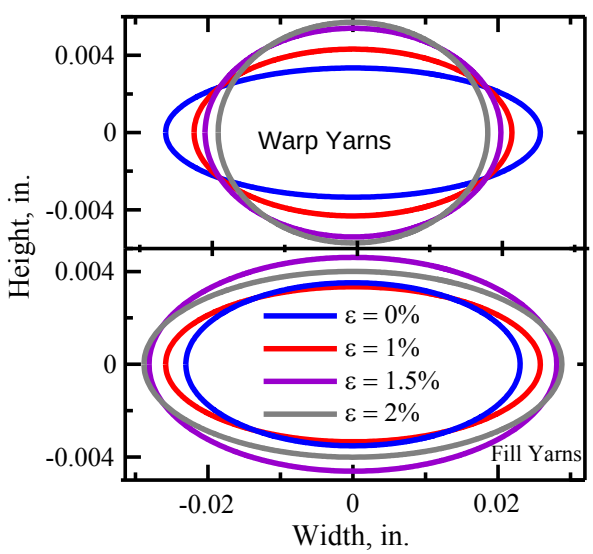

Figure 16. Comparison of Fill and Warp Cross-Sections (Ellipse) at Different Strain Levels

2.2.2.3 Fill Yarns—Longitudinal Cross-Section (Sinusoidal Curve).

The longitudinal geometry of fill yarns was analyzed, and the parameters associated with the geometry are listed in table 3. Figure 17 shows the fill yarn geometry at undeformed, 1.0%, 1.5%, and 2.0% strain levels. The amplitude indicates the waviness of the shape of the sinusoidal curve, and the period corresponds to the average strain in the warp direction. The

amplitude and period associated with each sample was computed using image analysis and was plotted on a common scale. It can be observed that as the warp yarns were loaded, the fill yarns became wavier, as indicated by the increase in the amplitude of the sinusoidal curve. This phenomenon can be observed in the transfer of the slack from the warp yarns to the fill yarns. Further, the increase in the amplitude is much greater during the initial phase of loading than after. A curve fitted through the amplitude at different strain levels can be used to estimate its parameters. A change in the sinusoidal curve period is directly correlated with the average strain in the warp direction, as shown in figure 18. This compares the undeformed shape of the fill yarns with the shape after a strain of 2% was applied in the warp direction.

Table 3. Fill Direction Sinusoidal Curve Parameters

Sample No.	$\varepsilon = 0.0\%$		$\varepsilon = 1.0\%$		$\varepsilon = 1.5\%$		$\varepsilon = 2.0\%$	
	Amplitude (in.)	Period (in.)	Amplitude (in.)	Period (in.)	Amplitude (in.)	Period (in.)	Amplitude (in.)	Period (in.)
1	0.003006	0.10996	0.006905	0.11354	0.008731	0.11889	0.008242	0.10910
2	0.003534	0.11562	0.006812	0.11244	0.007468	0.11207	0.007523	0.10806
3	0.003492	0.11452	0.006740	0.11582	0.007978	0.11226	0.007586	0.11071
4	0.003486	0.11575	0.007026	0.11248	0.008043	0.11315	0.008045	0.10441
5	0.004141	0.11956	0.007645	0.11436	0.008119	0.11169	0.007729	0.10949
6	0.003415	0.11592	0.007574	0.11384	0.008480	0.11592	0.007794	0.10889
7	0.003327	0.11815	0.006905	0.11234	0.008404	0.11812	0.007397	0.10721
8	0.003116	0.11349	0.006895	0.11234	0.007892	0.11814	0.007566	0.11084
9	0.003773	0.12338	0.007047	0.11026	0.007571	0.11734	0.008683	0.11215
10	0.003628	0.11605	0.007968	0.11544	0.007897	0.12118	0.008169	0.11232
11	0.003326	0.12180	0.007095	0.11237	0.008990	0.11995	0.007937	0.11087
12			0.007317	0.11354	0.008538	0.11743	0.007744	0.11268
13			0.007325	0.11240	0.008160	0.12124		
14			0.007423	0.11422	0.008907	0.12045		
15			0.008324	0.12426	0.009868	0.12496		
Average	0.003477	0.11675	0.007147	0.11320	0.008143	0.11625	0.007879	0.10946
Standard deviation	0.000309	0.00380	0.000399	0.00160	0.000468	0.00342	0.000383	0.00232
Parameter computed using point cloud	0.003410	0.11740	0.007360	0.11742	0.008068	0.11714	0.007780	0.10993

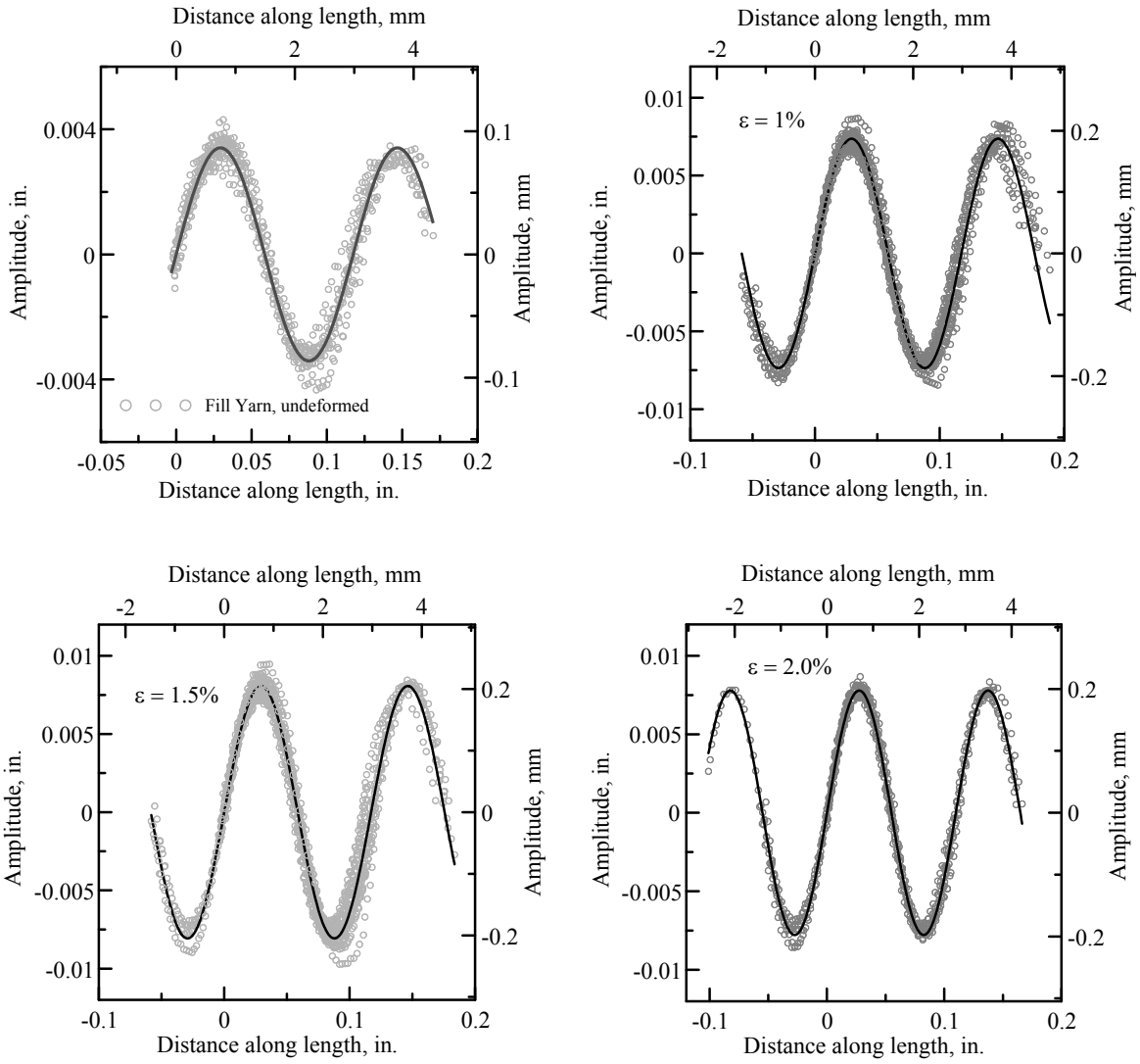

Figure 17. Fill Cross-Section (Sinusoidal Curve) at Undeformed, 1.0%, 1.5%, and 2.0% Strain Levels

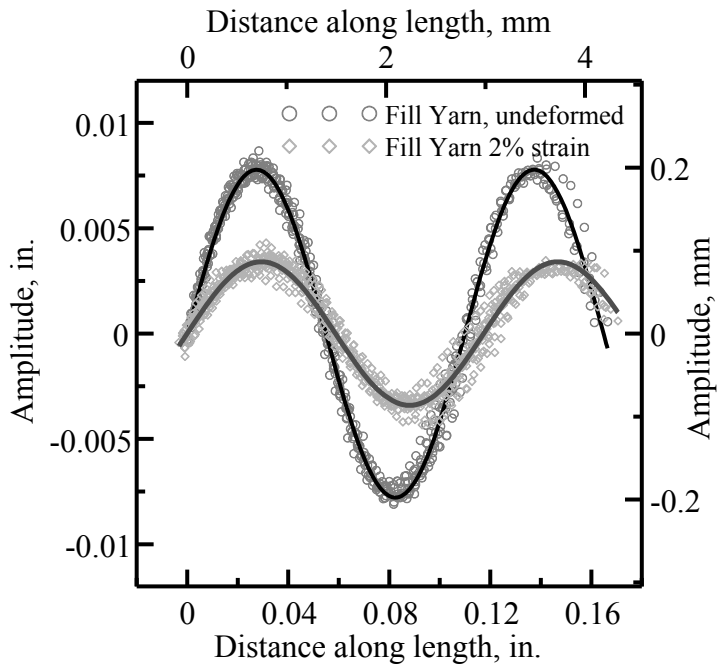

Figure 18. Fill Yarn Sinusoidal Curve at Undeformed Shape and 2.0% Strain Level

Figure 19 shows the effect of warp yarn loading on sinusoidal curve, representing the longitudinal cross-section of the fill yarn. A slight change in the period was observed; this can be attributed to the reorientation of yarns under load. The equation of the amplitude and frequency fitted curves are obtained as

$$A = 0.001 \ln\varepsilon + 0.0121$$
$$f = 54.2 - 215.4\,\varepsilon + 16538.9\,\varepsilon^2 \tag{5}$$

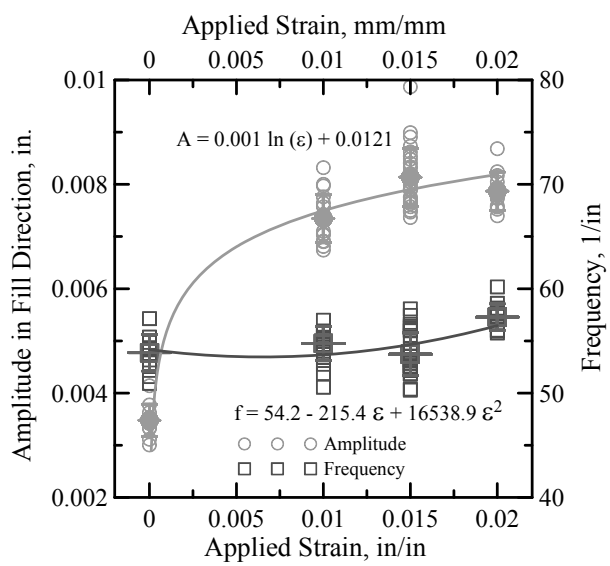

Figure 19. Comparison of Fill Yarn Cross-Section (Sinusoidal Curve) at Different Strain Levels

2.2.2.4 Warp Yarn—Longitudinal Cross-Section (Sinusoidal Curve).

The longitudinal geometry of warp yarns was analyzed, and the parameters associated with the geometry were computed using images. As discussed earlier, the undeformed warp yarns follow a sinusoidal curve, and as these yarns are loaded, they try to become flatter and approximately represent a step function. Therefore, deformed warp yarns are approximated using a step function. Parameters associated with sinusoidal curve for undeformed geometry and a step function for deformed geometry were computed and are listed in table 4. The amplitude indicates the waviness or peak of the sinusoidal curve, and period indicates the length of the complete sinusoidal curve. The length and height of the step function are also shown in the table. The amplitude and period associated with each sample was computed using image analysis and was plotted on a common scale. A curve fitted through all the points selected for various samples gives the overall estimation of the parameters. It can be observed that, as the warp yarns were loaded, they became flatter. This is due to the application of the load.

Table 4. Warp Direction Sinusoidal Curve Parameters

Sample No.	Undeformed		1.0% Strain Level		1.5% Strain Level		2.0% Strain Level	
	Amplitude (in.)	Period (in.)	Step Length (in.)	Step Height (in.)	Step Length (in.)	Step Height (in.)	Step Length (in.)	Step Height (in.)
1	0.00469	0.12107	0.05013	0.00231	0.05946	0.00251	0.05817	0.00144
2	0.00487	0.12256	0.05042	0.00340	0.05442	0.00267	0.05770	0.00171
3	0.00468	0.12299	0.04815	0.00307	0.05795	0.00318	0.05188	0.00181
4	0.00430	0.11615	0.04966	0.00193	0.05358	0.00223	0.06040	0.00041
5	0.00451	0.11574	0.05193	0.00311	0.05543	0.00179	0.05760	0.00165
6	0.00447	0.11807	0.05031	0.00265	0.05459	0.00203	0.05683	0.00081
7	0.00484	0.11899	0.05000	0.00267	0.05410	0.00251	0.05321	0.00026
8	0.00425	0.11910	0.05626	0.00184	0.06131	0.00223	0.05264	0.00044
9	0.00434	0.11758	0.05152	0.00200	0.05206	0.00220	0.05378	0.00020
10	0.00455	0.11613	0.05262	0.00310	0.04965	0.00215	0.05449	0.00008
11	0.00444	0.11788	0.05404	0.00280	0.05248	0.00181		
12	0.00388	0.11415	0.05808	0.00295	0.05526	0.00122		
13	0.00389	0.11705	0.05133	0.00150	0.05257	0.00161		
14	0.00407	0.11243	0.05069	0.00161	0.05586	0.00155		
15	0.00425	0.11539	0.05521	0.00285	0.05600	0.00131		
Average	0.00454	0.11875	0.05137	0.00263	0.05500	0.00230	0.05567	0.00088
Standard deviation	0.00021	0.00252	0.00227	0.00054	0.00340	0.00040	0.00284	0.00070

Figure 20 shows the effect of strain on the step height and length of the step function representing the longitudinal cross-section of the warp yarns under load. The warp yarns became flatter as they were loaded. This was observed in the decrease in step height of the step function.

A curve fitted through step height at different strain levels can be used to estimate the step height for the intermediate strain levels. The equation of the fitted curve obtained is

$$\text{Step height} = 0.00079 + 0.329*\text{strain} - 16.23*(\text{strain})^2 \quad (6)$$

As the strain level increased, the step length also increased. The equation representing this change is

$$\text{Step length} = 0.3496*\text{strain} + 0.04905 \quad (7)$$

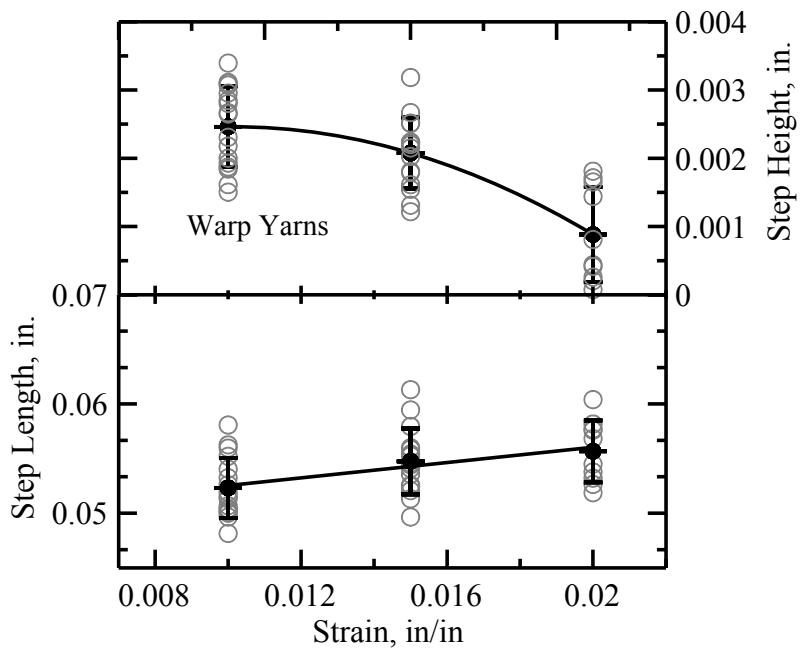

Figure 20. Step Length and Step Height in Warp Yarn at Different Strain Levels

2.2.2.5 Comparison of Fill and Warp Yarns.

The image analysis of longitudinal and transverse cross-sections of Kevlar warp and fill yarns has shown that there are basic differences in the geometry of these two yarns. These differences can be attributed to the weave pattern and the weaving process itself. Figure 21 shows the comparison of cross-sections (ellipses) of the fill and warp yarns. The warp yarns have greater semi-major axis while slightly less semi-minor axis compared to fill yarns. Initially, warp yarns have more area of cross-section than fill yarns.

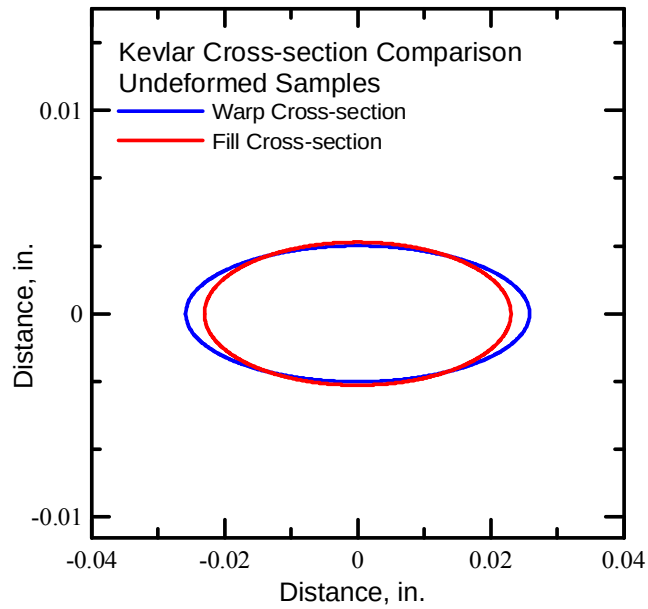

Figure 21. Comparison of Cross-Sections (Ellipses) of Undeformed Fill and Warp Yarns

Figure 22 shows the longitudinal cross-sections of warp and fill yarns. It is interesting to note that both yarns have the same period. This means both sides have the same number of yarns per inch. The number of fill and warp yarns per inch of fabric computed based on period is approximately 17 (yarn/inch), which is the same as the manufacturer's specification. Further, the warp yarns have greater amplitude than the fill yarns or, in other words, warp yarns have greater slack than fill yarns. This was also observed during the swath test in the warp and fill directions.

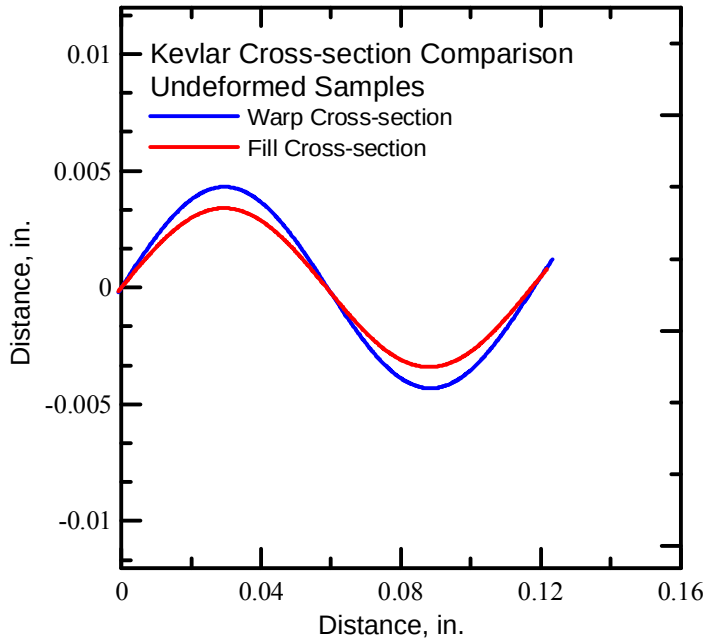

Figure 22. Comparison of Longitudinal Cross-Sections of Undeformed Fill and Warp Yarns

2.3 KEVLAR SINGLE-YARN TENSILE TESTS.

2.3.1 Introduction.

The computed geometrical parameters can be used to build an FE model of the Kevlar yarns; however, to simulate Kevlar fabric using explicit analysis, it was important to initially verify the single-yarn properties. Using the data generated in the previous section, the elliptical and sinusoidal representations of a yarn were used to build a Kevlar warp yarn model, as shown in figure 23.

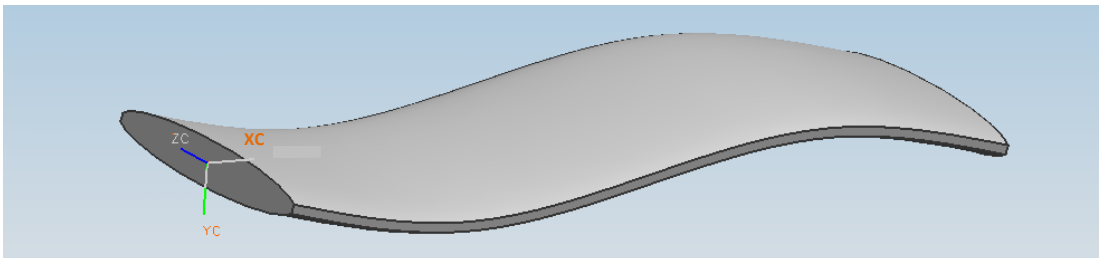

Figure 23. Model Generation of a Yarn Using Longitudinal and Transverse Geometrical Parameters of Warp Yarn

A user subroutine was developed for solid elements to simulate the material behavior of Kevlar yarns for use with the LS-DYNA explicit analysis software package. By assuming that the mechanical properties have no significant deviation among directions perpendicular to the yarn axis, Kevlar yarn can be assumed to be transversely isotropic. If the direction "1" is normal to the plane of material isotropy (i.e., along the yarn axis), the constitutive relationship of a Kevlar yarn can be represented as

$$\begin{bmatrix} \Delta\varepsilon_{11} \\ \Delta\varepsilon_{22} \\ \Delta\varepsilon_{33} \\ \Delta\varepsilon_{12} \\ \Delta\varepsilon_{31} \\ \Delta\varepsilon_{23} \end{bmatrix} = \begin{bmatrix} \frac{1}{E_{11}} & 0 & 0 & 0 & 0 & 0 \\ 0 & \frac{1}{E_{22}} & 0 & 0 & 0 & 0 \\ 0 & 0 & \frac{1}{E_{33}} & 0 & 0 & 0 \\ 0 & 0 & 0 & \frac{1}{2G_{12}} & 0 & 0 \\ 0 & 0 & 0 & 0 & \frac{1}{2G_{31}} & 0 \\ 0 & 0 & 0 & 0 & 0 & \frac{1}{2G_{23}} \end{bmatrix} \begin{bmatrix} \Delta\sigma_{11} \\ \Delta\sigma_{22} \\ \Delta\sigma_{33} \\ \Delta\sigma_{12} \\ \Delta\sigma_{31} \\ \Delta\sigma_{23} \end{bmatrix} \tag{8}$$

To estimate the material properties of the yarn, statistical parameters for the strength, strain capacity, and longitudinal Young's modulus were measured using single-yarn tensile tests extracted from fabric swaths.

The single-yarn tensile test objectives were to

- measure the tensile response of Kevlar 49 single yarns under uniaxial tensile loading.
- provide estimation of strain capacity and longitudinal stiffness of the yarn.
- capture the effect of gage length (G.L.) on failure stress.

2.3.2 Specimen Preparation and Fixture Details.

Samples for single-yarn tensile tests were obtained by removing warp direction yarns from the woven fabric. Yarns were removed cautiously without damage or dislocation of their relative position. The following steps were followed:

1. Cut along the length of the fabric based on G.L. required for the test sample.
2. Cut the sample sides along the warp direction to remove stitches on fabric edges.
3. Remove fill yarns from both ends of the fabric to simplify removal of warp yarns.
4. Apply KrazyGlue on both ends of the warp yarns to allow removal without fraying.
5. After glue is dried, remove the yarns one by one with care.

After removal, the single-yarn samples were handled with care so as not to damage filaments during setup.

The single-yarn test setup is shown in figure 24. A low-capacity load cell was used during the test to record the load. A universal joint was connected to the test frame to allow rotation of the grip and remove any potential bending moment. The universal joint also helped to align the yarn during the test. To avoid any slipping of the test sample during the test, the yarn was fed and wrapped around the upper mandrel. After the cross head was moved to the G.L. position, the yarn was aligned and wrapped along the bottom grip mandrel. The yarn was then secured in the mandrel using frictional wedge screws. A laser beam was used to check the sample alignment during the test, as shown in figure 24.

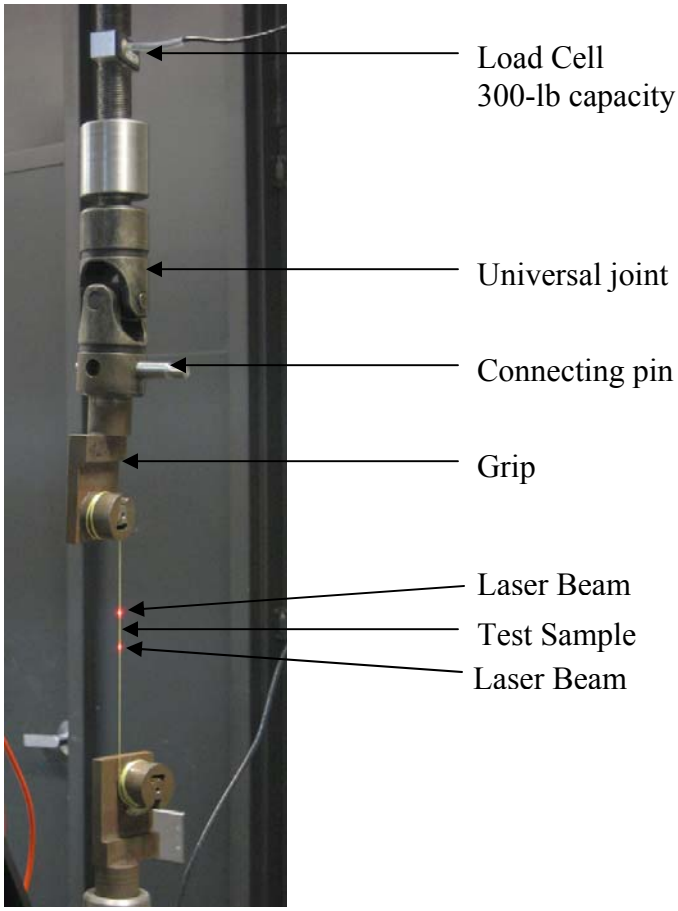

Figure 24. Single-Yarn Test Setup

2.3.3 Specimen Test Procedure.

The single-yarn test specimens were tested on an MTS tensile test machine frame under displacement control, resulting in a strain rate of 4.167×10^{-4} s^{-1}. Figure 25 shows the sample during the test. The sample was not perfectly vertical before the test. This was due to the free tilt of the fixture in the presence of a universal joint. However, as the test started and the load increased, the sample aligned itself. During the test, the sample remained vertical, which was confirmed by the laser light on the specimen.

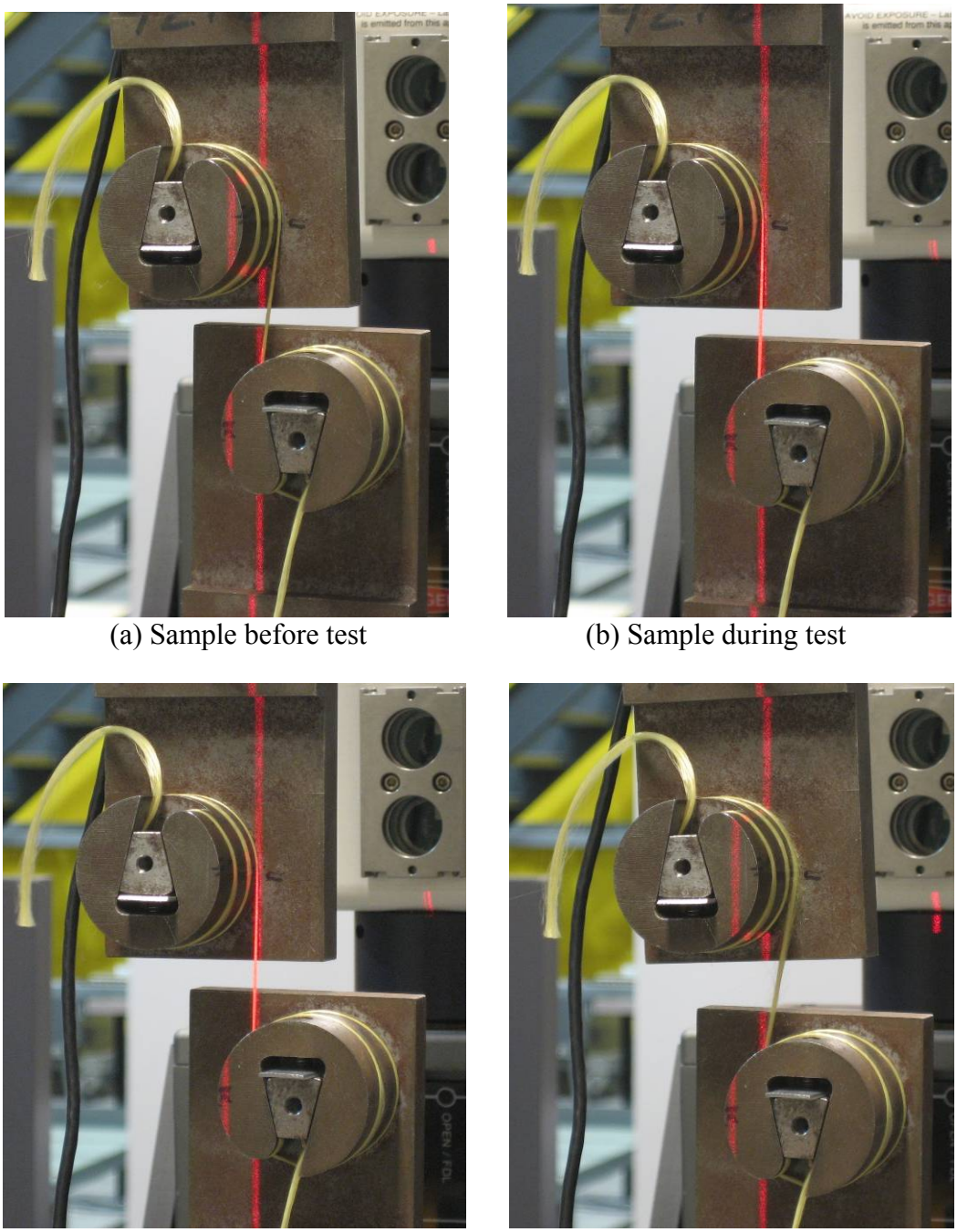

(a) Sample before test (b) Sample during test

(c) Sample during test (d) Sample after failure

Figure 25. Single-Yarn Tensile Test

Table 5 shows the test plan used during the single-yarn tensile tests. Ten replicate samples of six different specimen G.L.s (2″, 5″, 8″, 11″, 14″, and 17″) were tested. During all the tests, the strain rate was maintained constant by changing the displacement rate as a function of specimen length. The effect of G.L. on the peak stress, Young's modulus, and strain at ultimate strength were measured.

Table 5. Single-Yarn Test Plan

Sample No.	Gage Length (in.)	Strain Rate (/min)	Stroke Displacement Rate (in/min)	Number of Replicates
1	2	0.025	0.05	10
2	5	0.025	0.125	10
3	8	0.025	0.2	10
4	11	0.025	0.275	10
5	14	0.025	0.35	10
6	17	0.025	0.425	10

2.3.4 Results and Discussion.

2.3.4.1 Kevlar Single-Yarn Test Results.

The stress-strain curve obtained from the test with 2″, 5″, and 8″ G.L.s (L_0) are shown in figure 26. The variation among the test results is small, which ensures repeatability. The Young's modulus computed for the 2″ long samples is 3304 ksi, average peak stress is 275 ksi, and strain at peak stress is estimated to be 0.12 in/in.

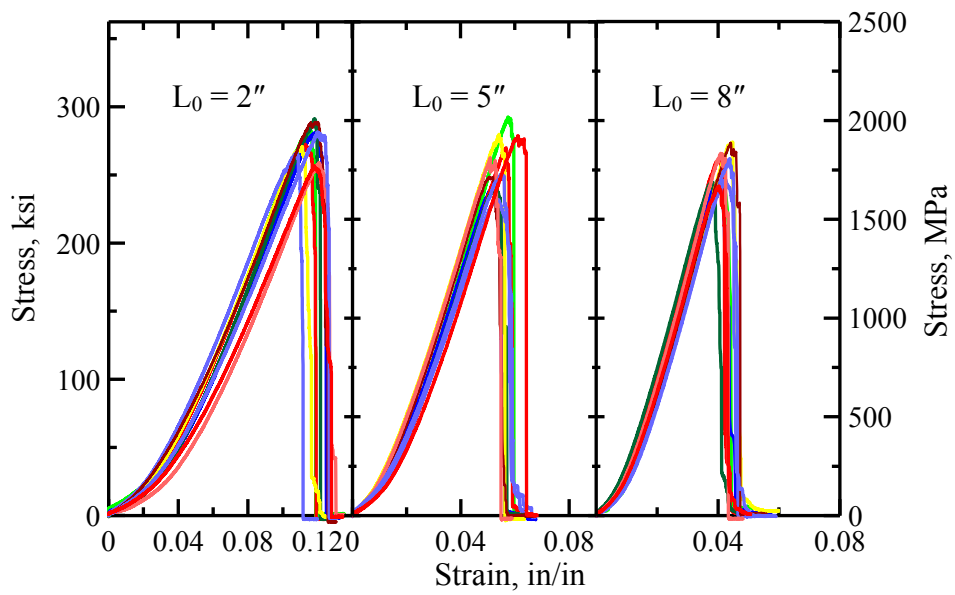

Figure 26. Stress-Strain Curves for G.L. = 2″, 5″, and 8″

The Young's modulus increases as the G.L. increases. As the G.L. increases from 5″ to 8″, the Young's modulus increases from 6342 to 8400 ksi, the average ultimate strength decreases from 260 to 256 ksi, and the strain at this level decreases from 0.054 to 0.042 in/in. The material properties obtained are shown in table 6. The stress-strain curve obtained from the test with 11″, 14″, and 17″ G.L.s are shown in figure 27. The Young's modulus computed for these G.L.s

ranged from 9,741 to 11,232 ksi, the average peak stress was 246-230 ksi, and the strain at peak stress was estimated to be 0.034-0.026 in/in. Note that, as the yarn length is increased, the stiffness increased; however, the ultimate strength and strain capacity marginally decreased.

Table 6. Single-Yarn Test Results

Sample No.	L_0=2″			L_0=5″			L_0=8″		
	E (ksi)	Ultimate Strength (ksi)	Strain at Ultimate Strength	*E* (ksi)	Ultimate Strength (ksi)	Strain at Ultimate Strength	*E* (ksi)	Ultimate Strength (ksi)	Strain at Ultimate Strength
1	3438	283	0.115	6698	293	0.058	8441	245	0.041
2	3393	281	0.118	6194	242	0.052	8506	246	0.040
3	3301	274	0.112	6422	270	0.057	8524	262	0.040
4	3482	291	0.119	6263	241	0.053	8357	245	0.038
5	3343	271	0.111	6463	280	0.054	8677	275	0.045
6	3296	266	0.108	5953	232	0.053	8084	247	0.042
7	3310	289	0.120	6427	249	0.051	8253	274	0.044
8	3221	259	0.121	6539	263	0.051	8547	266	0.041
9	3167	282	0.120	6173	251	0.055	8321	262	0.044
10	3080	257	0.118	6269	279	0.061	8265	242	0.040
Maximum	3482	291	0.121	6698	293	0.061	8677	275	0.045
Minimum	3080	257	0.108	5953	232	0.051	8084	242	0.038
Mean	3303	275	0.116	6340	260	0.054	8397	256	0.042
Standard Deviation	122	12	0.004	213	20	0.003	174	13	0.002

Sample No.	L_0=11″			L_0=14″			L_0=17″		
	E (ksi)	Ultimate Strength (ksi)	Strain at Ultimate Strength	*E* (ksi)	Ultimate Strength (ksi)	Strain at Ultimate Strength	*E* (ksi)	Ultimate Strength (ksi)	Strain at Ultimate Strength
1	9,222	229	0.030	10,682	210	0.024	11,081	221	0.024
2	9,873	266	0.035	10,333	262	0.033	11,220	259	0.029
3	9,902	243	0.032	10,678	218	0.027	10,747	211	0.025
4	9,521	247	0.035	11,066	285	0.032	11,794	261	0.027
5	9,673	234	0.034	11,045	265	0.032	11,140	215	0.025
6	10,128	279	0.036	9,819	211	0.029	11,959	253	0.027
7	9,315	219	0.033	11,079	264	0.030	10,845	213	0.026
8	10,031	257	0.034	10,877	224	0.026	11,727	257	0.027
9	9,911	230	0.032	10,613	241	0.030	10,586	179	0.022
10	9,808	259	0.035	10,805	248	0.029	11,189	232	0.026
Maximum	10,128	279	0.036	11,079	285	0.033	11,959	261	0.029
Minimum	9,222	219	0.030	9,819	210	0.024	10,586	179	0.022
Mean	9,738	246	0.034	10,700	243	0.029	11,229	230	0.026
Standard Deviation	301	19	0.002	389	26	0.003	462	27	0.002

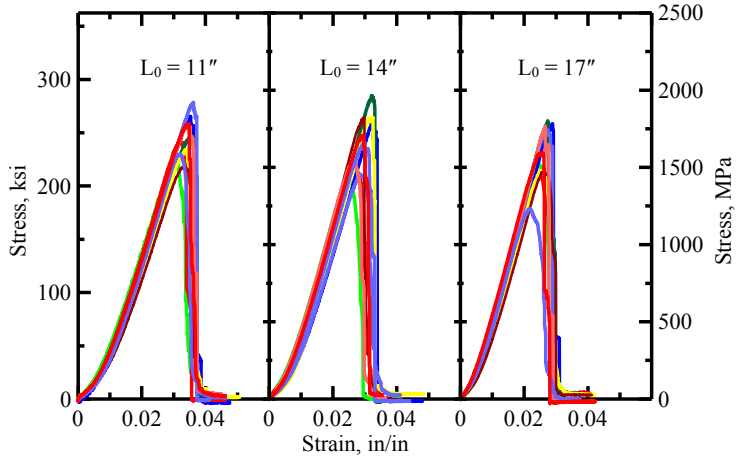

Figure 27. Stress-Strain Curves for G.L. = 11″, 14″, and 17″

The effect of G.L. on Kevlar yarn properties is prominent. Figure 28 shows several typical stress-strain curves for the G.L.s tested. It can be observed that, as the G.L. increased, the Young's modulus increased, while peak stress reduced significantly. The reduction in the peak stress with increase in the G.L. can be attributed to the increase in imperfection with the increase in G.L. These variations are attributed to two factors: (1) the Weibull strength effect due to the fiber length and (2) the probability distribution of the flaws in larger lengths that leads to a decrease in strength as the fiber length increases. The second factor is the initial waviness in the length of the filaments, which leads to unequal stress distribution in the filament length. As the fiber length increases, there is more uniformity in the length, and the initial stretching and fiber alignment decreases. The effect of filament waviness on the strength has been addressed by Zohdi, et al., [8-10], as shown in figure 29. A quantitative analysis of the G.L. effect allows for the determination of Weibull parameters.

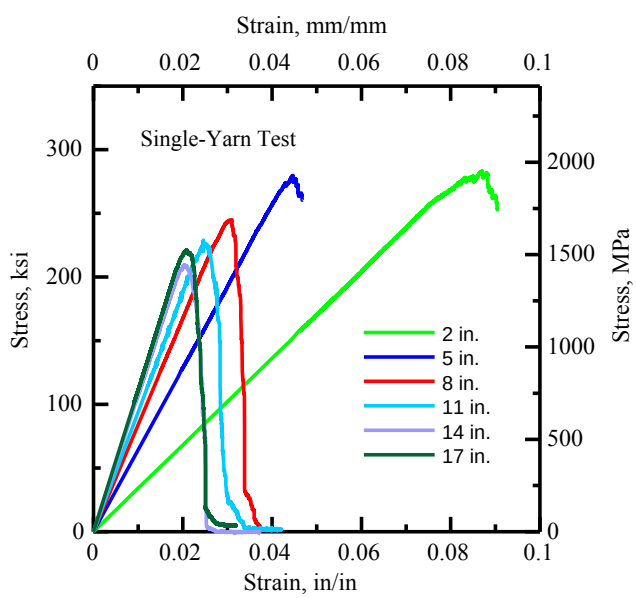

Figure 28. Comparison of Stress-Strain Curves of Different G.L.s

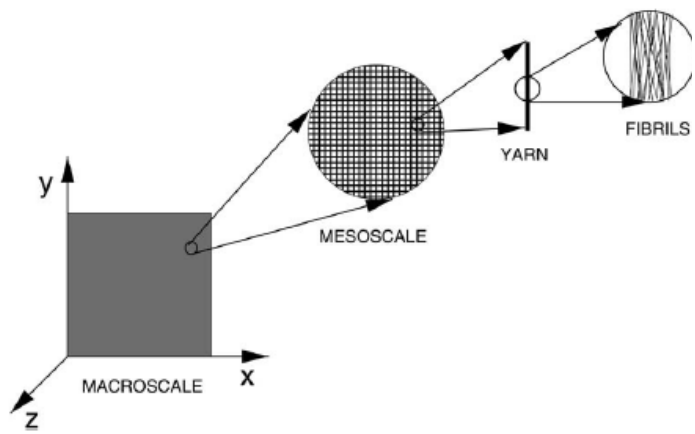

Figure 29. Microstructural Scales of Textile, Yarn, and Filament

Figure 30 shows the effect of G.L. on Young's modulus, ultimate yarn strength, and strain at ultimate strength. A linear relation between the strength and G.L. is observed. It is observed that as G.L. increases, Young's modulus of the yarns increases; on the other hand, strain at peak stress decreases. A second-order polynomial curve was used to empirically relate the effect of G.L. on the Young's modulus, whereas a log curve was used for the strain at ultimate strength. Equations governing these effects are shown below.

$$\sigma_{uts} = -19L_0 + 1916 \tag{9}$$

$$E = 8590 + 7950L_0 - 231L_0^{\,2} \tag{10}$$

$$ln\varepsilon_{uts} = -0.7 * lnL_0 - 1.7 \tag{11}$$

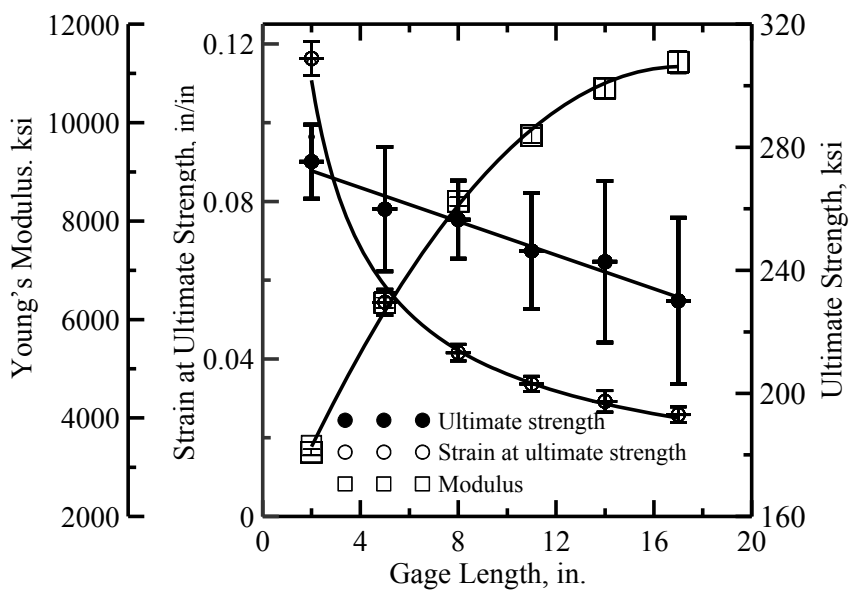

Figure 30. Young's Modulus, Ultimate Strength, and Strain at Ultimate Strength vs G.L.

2.3.5 Weibull Analysis.

2.3.5.1 Introduction.

The classic way to view the strength of the materials or structures is a deterministic one. That is, a true strength, single value that is characteristic of the material or structure, is supposed to exist. In experiments to determine this true strength, considerable scatter in the results is usually observed. As this is not considered to be a feature of the material or object itself, it is usually attributed to uncontrollable experimental variables. As a consequence, the standard deviation is interpreted as indicating the success of standardizing the experimental setup and procedures. Therefore, standard deviation can be considered to be an indicator of the quality of an experiment or test method.

The deterministic view has become much less popular in the technical sciences. If the deterministic view is valid, identical experiments performed on material specimens of different sizes should yield the same results for failure stress. However, it has been shown that for Kevlar yarns, larger specimens have a lower failure stress compared to smaller ones [11]. These systematic differences cannot be explained by random variations in experimental procedures, but by imperfections included in the yarn structure. Flaws can cause a material to fail long before its ideal strength is reached. Although this ideal strength could be interpreted as true strength, for practical purposes, it is more important to understand the actual strength of the material rather than the true strength. It is more logical, therefore, to accept imperfections as an integral part of a material or structure and to account for their presence when describing its strength. The distribution of imperfections within a structure is of a probabilistic nature. As a consequence, the strength of the structure itself is of a probabilistic nature. The Weibull analysis is widely used for this purpose and is used here to explain variation in Kevlar strength as a function of G.L. The basic form of the Weibull equation for cumulative probability density is

$$P(\sigma)=1-\exp\left[-\left(\frac{\sigma}{\sigma_0}\right)^m\right] \tag{12}$$

Where σ is the failure stress, σ_0 is the reference or scaling value related to the mean, and m is the Weibull modulus or shape parameter of a two-parameter Weibull model.

To include the length effect in the Weibull model, parameters related to G.L. or volume of the yarns can be introduced in the model. The modified three-parameter Weibull equation for cumulative probability density is given by

$$P(\sigma)=1-\exp\left[-\left(\frac{v}{v_0}\right)\left(\frac{\sigma}{\sigma_0}\right)^m\right] \tag{13}$$

Where ν represents the volume of the yarn and ν_0 represents the scaling value for the volume. These parameters can be represented as L and L_0, the length of the specimen and the characteristic length, respectfully.

2.3.5.2 Results and Discussion.

Table 7 shows the peak stress values obtained for each test case.

A MATLAB code was used to fit the single-yarn tensile data. Cumulative probability distribution of the test data was obtained, and the parameters are presented in table 8.

Table 7. Single-Yarn Test Data

Replicate No.	Ultimate Strength, psi					
	2 in.	5 in.	8 in.	11 in.	14 in.	17 in.
1	283,452	293,240	245,510	229,079	209,638	221,328
2	281,223	241,606	246,030	266,399	262,167	258,862
3	274,014	270,257	262,518	242,805	218,487	211,109
4	291,305	240,882	245,114	247,162	285,138	261,488
5	271,242	280,080	274,580	234,533	264,702	214,617
6	266,093	232,157	246,834	278,767	211,211	253,069
7	289,189	248,791	273,913	218,578	264,396	213,407
8	259,123	262,812	266,263	257,312	223,613	256,577
9	281,687	250,681	262,382	230,199	241,210	179,289
10	256,713	279,242	242,194	258,727	247,818	231,670

Table 8. Weibull Parameters

		G.L.s					
		2 in.	5 in.	8 in.	11 in.	14 in.	17 in.
Weibull Parameters	σ_0	280,130	265,140	260,160	249,790	250,160	239,370
	m	21.7	11.5	14.3	11.9	7.9	8.8

Figure 31 shows the Weibull curve fitting to experimental data using least square method. Note that when the G.L. of the sample increases, the cumulative probability plot shifts towards lower stress values, which is a clear indicator of dependence of peak stress on the G.L.

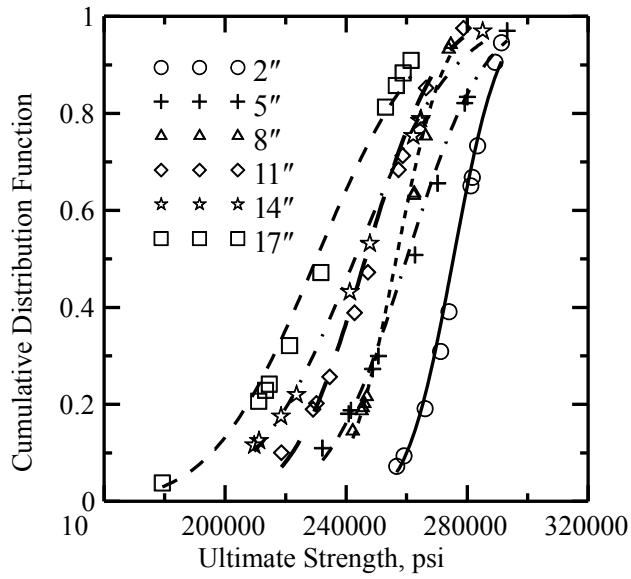

Figure 31. Comparison of Cumulative Failure Probability vs Peak Stress for Different G.L.s

3. KEVLAR 49 HIGH STRAIN RATE TESTS.

3.1 OVERVIEW.

Woven fibers and yarns are increasingly used in pure and woven form for ballistic protection clothing and confinement chambers for jet engines. These applications have created a demand for numerical modeling of the fabrics and more in-depth information about the behavior of fibrous materials and yarns. Yarn manufacturers usually provide quasi-static tensile strength for the single-fiber form of the material. However, this information cannot be scaled linearly for a yarn consisting of many fibers. Also, the strain rate at which this information is obtained is not in the same order of magnitude as the higher strain rates observed in ballistic applications.

Some research on quasi-static strength of yarns has been reported along with several dynamic strength studies. Schwartz, et al. [12], performed quasi-static tensile tests on Kevlar 29 and 49 single fibers at various G.L.s. The authors reported that the data indicated an increase in strength for a fiber at shorter G.L.s and the variability in the failure loads of fibers sampled from a yarn cross-section was greater than for fiber segments sampled along a single filament. Also, the log-log dependence of strength on fiber G.L. was not linear, as predicted from the weakest-link, Weibull failure model. Consequently, the Weibull shape parameter is probably not a material constant for aramid filament. Also, the Weibull shape parameter, calculated from varying G.L., was almost double that obtained from tension tests at a fixed G.L. Schwartz, et al. [13], observed that the strength of ultra-high polyethylene fibers generally increased with increasing strain rate within a range of 6.7×10^{-5} to 0.017 s^{-1}, but the behavior was bilinear. Wagner, et al. [14], reported that Kevlar 29, Kevlar 49, and Kevlar 149 fibers were insensitive to the strain rate at a range of 3×10^{-4} to 0.024 s^{-1}. They also stated that the strength of aramid fibers is found to closely follow the Weibull distribution at all strain rates. The shape and scale parameters are insensitive to strain rate. Amaniampong and Burgoyne [15] observed the effect of G.L. and strain rate on the failure stress and failure strain of Kevlar 49 yarns. They stated that the yam

strength decreases slightly as the G.L. increases, whereas the failure strain of the aramid yarns is found to be independent of the G.L. Also, the failure strain of the aramid yarns decrease slightly as the strain rate increases. The strength decreases with an increase in strain rate from $3x10^{-4}$ to 0.003 s^{-1}, which is contrary to theoretical predictions despite the fact that the Weibull distribution was found to be appropriate for both the failure load and strain of the yarns tested. The discrepancy may be because the failure process is not attributed to a statistical distribution of defects in the yarns, which is an implicit assumption in the theory. Sharda, et al. [16], and Rajan, et al. [1], studied the quasi-static properties of Kevlar 49 (17x17) and Zylon AS (35x35) fabric in tension at a strain rate of $1.4x10^{-4}$ s^{-1} and the load-deflection response of single- and multilayers in static penetration tests. The material behavior obtained from the experimental study was then used as the constitutive model in an FE simulation of the static test.

Xia and Wang [17] studied the strain rate dependence of Young's modulus, the failure stress, and the failure strain of Kevlar 49 over a strain rate range of 10^{-4} to 1350 s^{-1}. An increasing trend was reported for failure stress, strain, and Young's modulus with increasing strain rate. The "skin core" structure of Kevlar fiber and experimental Weibull data confirmed that there are two types of fracture modes in Kevlar fiber and the application of bimodal Weibull distribution is correct. Weibull shape parameters can be treated as constants for different strain rates, but scale parameters have sensitivity to strain rate, whose values increase with the increase of strain rate.

Mulkern and Raftenberg [18] performed quasi-static tests on nine yarn specimens of Kevlar KM2 containing 400 filaments at a 2″ G.L., carried out at a strain rate of 4×10^{-3} s^{-1}. They found the average strength of never-woven, untwisted yarn specimens was 2.66 ±0.04 GPa (385.8 ±5.8 ksi). They also investigated the twist effect on the failure strength. The twist multiplier was found to be 1.2, which agreed with that reported for Kevlar in Yang [19]. The strengths of extracted warp and fill yarns, tested in an untwisted state, were found to be 2.06 ±0.01 GPa (298.8 ±1.5 ksi) and 2.20 ±0.05 GPa (318 ±7.3 ksi), respectively. Substantial strength degradation was incurred during one or more of the weaving, finishing, and yarn extraction processes. Finally, 68-yarn-wide, single-ply specimens of plain-woven, 600-D KM2 fabric were tested in quasi-static, uniaxial tension. Warp- and fill-oriented fabric specimens had strengths of 2.23 ±0.04 GPa (323.4 ±5.8 ksi) and 2.67 ±0.04 GPa (387.3 ±5.8 ksi), respectively. These fabric strengths are larger than those found for extracted warp and fill yarns. The mechanism of frictional contact between adjacent yarns was speculated to account for the added strength in the woven fabric case.

Cheng and Chen [20] conducted a study on the mechanical properties of a single fiber of Kevlar KM2 over a range of strain rates (0.00127 to 2451 s^{-1}) by using an MTS 810 servohydraulic material test machine and a modified split-Hopkinson tension bar (SHTB) device. Loading rate effects were studied in both the longitudinal and transverse directions. Results showed that the mechanical behavior of the Kevlar KM2 fibers is insensitive to the loading rates in the range covered in that study and fibrillation was the major cause of failure of the Kevlar KM2 fibers at both quasi-static and dynamic loading rates.

Farsi, et al. [21], studied the parameters that affect the strength of yarns. The quasi-static and dynamic strength of five different yarns (Kevlar 129, Kevlar KM2, Kevlar LT, Twaron, and Zylon) were obtained using the servohydraulic and SHTB methods, and the rate dependency of

the failure strength of each yarn was quantified. The Kevlar products showed limited dependence on strain rate, while Twaron and Zylon showed a much more significant dependence on increasing strain rate. A study of the effect of specimen size on the failure stress was carried out for Kevlar 129. Single fibers were tested at five different G.L.s (0.2″, 0.64″, 1″, 2″, and 4″), and multifiber specimens were tested at various G.L.s (1″, 4″, 6″, and 8″). By studying the variation of statistical strength with increasing specimen size, a decreasing trend for the tensile strength was observed.

The following sections present a high strain rate test system and the test results of Kevlar 49 fabric and single-yarn specimens at the strain rate range of 20 to 170 s^{-1}. One- and two-inch G.L.s were chosen for both specimen types. Three sets of Kevlar 49 fabric specimens were tested on April 2007, July 2007, and March 2008, respectively. The test results of fabric specimens are presented and discussed in time sequence.

3.2 HIGH STRAIN RATE TEST SYSTEM.

The high strain rate test system, shown in figure 32, includes an MTS 5-kip servohydraulic tensile test machine, MTS Flex SE control panels, laser extensometer, and data acquisition system. Each of the components will be described in the following sections.

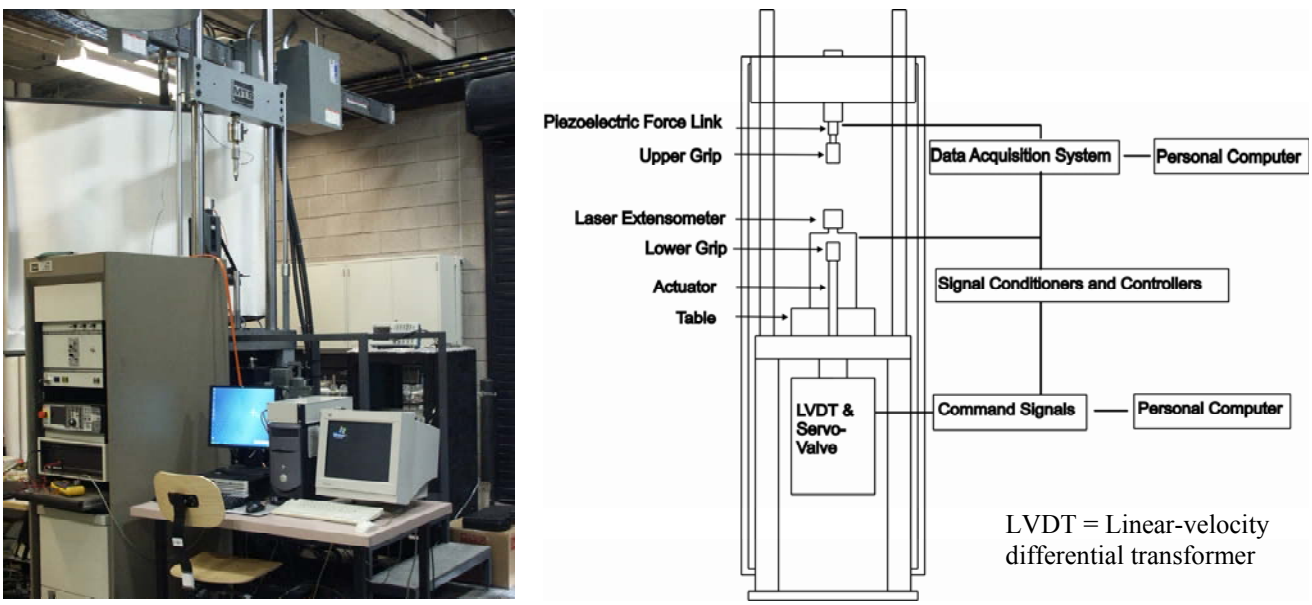

(a) (b)

Figure 32. High Strain Rate Test System: (a) Actual and (b) Schematic

3.2.1 The MTS Test Frame.

The MTS 5-kip servohydraulic test frame (figure 33(a)), operated in an open-loop mode, was used to perform high strain rate test. The velocity of the stroke/actuator is controlled by the servo valve (figure 33(b)). Different velocities were manually obtained by opening the servo valve to different levels. The more open the servo valve, the higher the velocity of the actuator. A slack adaptor (figure 33(c)) was used to facilitate the specimen setup and allowed the stroke to

accelerate to the needed test speed before the specimen was loaded. The current system is capable of developing cross-head velocities up to 550 inches/second.

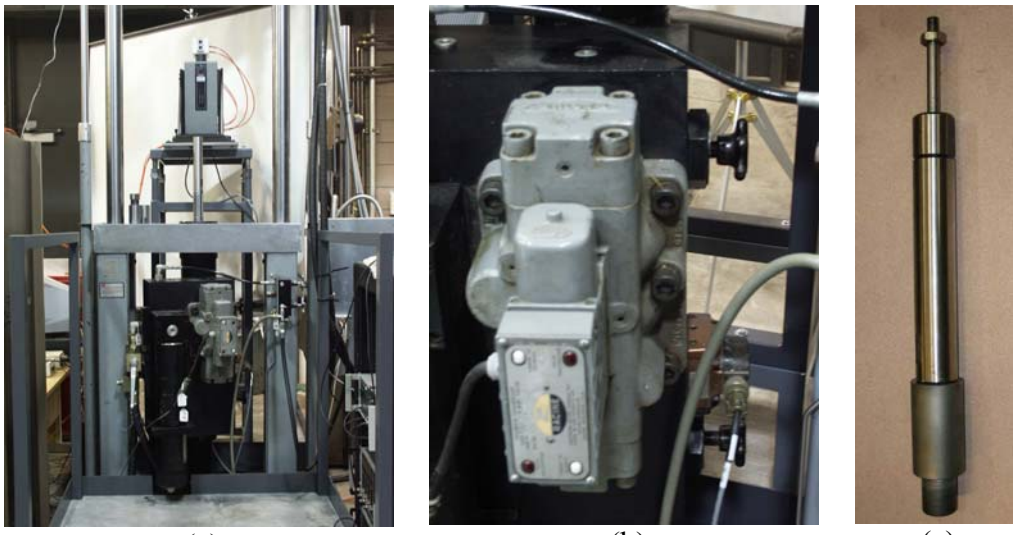

(a) (b) (c)

Figure 33. (a) MTS Test Machine, (b) Servo Valve, and (c) Slack Adaptor

3.2.2 Signal Conditioners and Control Panels.

The following sections discuss the signal conditioners and control panels used in this research.

3.2.2.1 FlexTest SE Controllers.

A state-of-the-art, new MTS FlexTest SE control panel (figure 34(a)) and personal computer (figure 34(b)) for controlling the test machine were installed and calibrated.

(a) (b)

Figure 34. (a) MTS FlexTest SE Controller and (b) Personal Computer

3.2.2.2 Dual-Mode Charge Amplifier.

A dual-mode charge amplifier (figure 35) was used for conditioning the signal from the piezoelectric force transducer (details are presented in section 3.2.4).

Figure 35. Kistler® 5010B Dual-Mode Charge Amplifier

The charge amplifier is a direct current amplifier with very high input impedance and capacitive negative feedback, intended to convert the electric charge from a piezoelectric transducer into a proportional voltage on the low-impedance amplifier output. The calibration factor setting (adjustment of transducer sensitivity of the amplifier) makes it possible to standardize the amplifier sensitivities. The overall measuring ranges of the charge amplifier are given in picocoulombs (pC) for each 10V output voltage. However, the range in practice is given differently—as mechanical units (mc) per volt of output voltage making allowance for the sensitivity of the connected transducer (calibration factor, expressed in pC per MU, where MU represents mechanical unit (e.g., psi, lb, g, etc.) and pC represents the effective capacitance of the transducer). There are three different options for time constants (long, medium, and short) on the charge amplifier. The time constants are determined by the bleeder resistance and the range capacitor, and therefore, are dependent on the measuring range. The time constant in the negative feedback circuit causes an exponential discharge of the range capacitor. The calibration factor calculated at a long-time constant was used in this study. All charge amplifiers have some drift on the output voltage. This drift is re-zeroed every time the reset/operate function on the charge amplifier is used. However, there are instances when it is not possible to the reset control drift. If the time period is long enough, amplifier drift may accumulate to produce an unacceptable offset in the signal. Enabling a time constant constrains the drift rate. This is because a time constant is effectively a high-pass filter and a linear drift has zero frequency and is thus blocked by the filtering action. The high-frequency pulses transmit right through the filter without distortion.

3.2.2.3 High-Rate Control Panel.

To obtain the high-speed function of the MTS machine, a high-rate control panel is needed (figure 36). The switch with the key on the left side is used to select the closed- or high-rate loop options. The blue button is the actuator reset button, which resets the actuator/stroke to its original position after a test. The yellow button is the arm button that, when lit, indicates the

system is ready. When the arm button is pressed, the red button on the right side of the panel is lit. The red fire button triggers the high-rate test when pressed.

Figure 36. High-Rate Control Panel

3.2.3 Grip.

To ensure low inertial forces in a high strain rate test, it is important to maintain the weight of the grips as low as possible while ensuring a rigid attachment of the specimens to the grips. A new gripping system for dynamic tests was designed using internal wedges that were held inside the female portion of the screw connectors. The grip wedges and gripping arrangement are shown in figure 37. The total weight of the grip system is 6.8 lb. Four steel wedges (1.0″ wide, 2″ long) were used to grip the specimen at both ends. The entire length of the wedge grip faces was serrated to improve the contact with the test specimen. These wedges are housed inside hollow connecting rods. The grip was tightened by turning the screw assembly that pushes the grip against two slanted surfaces inside the wedge. Care must be exercised to ensure that there is no relative sliding of the two grip faces as the wedge components slide and tighten.

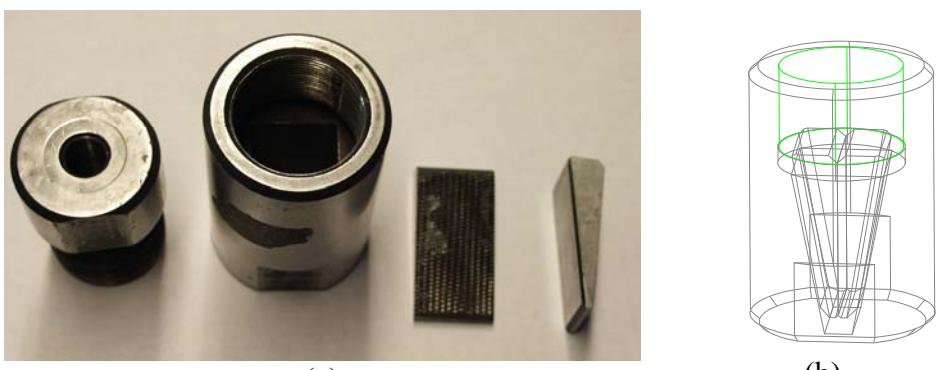

(a) (b)

Figure 37. Grip Set: (a) Actual and (b) Schematic

3.2.4 Force Measurement.

Strain gage-based load cells are too soft and compliant at high strain rates. The frequency response of a standard load cell may not be sufficient to detect and measure the events that occur in a short duration. In contrast, a piezoelectric force transducer, which is significantly stiffer than the conventional load cells, was used for the high strain rate tests. In the current tests, the force was measured by a Kistler 9041A piezoelectric force transducer with a capacity of 20,000 lb, as shown in figure 38. The piezoelectric force transducer was connected to the charge

amplifier (as discussed in section 3.2.2.2) to generate the force signal in terms of analog voltage output for the purpose of data acquisition.

Figure 38. Piezoelectric Force Transducer

3.2.5 Data Acquisition.

A four-channel data acquisition card was used on a dedicated computer for data acquisition purposes. This card was a 66-MHz/32-bit, high-speed digital input/output data acquisition module (Strategic Test Corporation, Woburn, MA), which allowed four data channels to be continuously transferred to the personal computer host at 200 MBytes/s. The card has 64-MBytes (32-MByte samples) memory as standard and can operate at the maximum sampling rate of 10 MBytes/s. All four channels on the data acquisition card (figure 39) were used to acquire the electrical signals. Two of the channels provided sinusoidal wave signals from a laser extensometer: one was an analog output from the piezoelectric force transducer and one was an analog output from the linear-velocity differential transform (LVDT) per stroke. The two connections on the left side are for external triggers that were not used in the current test. The internal trigger function of the card was used for triggering the test event. Using the SBench 5.3 software system, the signals from four channels stored in the onboard memory were displayed on the computer screen, digitized, and exported for further processing.

Figure 39. Four-Channel Data Acquisition Card

3.3 KEVLAR FABRIC.

3.3.1 Sample Preparation and Test Setup.

The size of the original Kevlar 49 fabric was too large to be used directly in the high strain rate test. The fabric had to be cut into specimens by using an electrical cutter. Much attention was given to ensure that there were exactly eight yarns in the section of G.L. Thin aluminum sheets were glued (using epoxy) on both ends of the specimen to reduce the stress concentration effect due to the gripping wedges, as shown in figure 40.

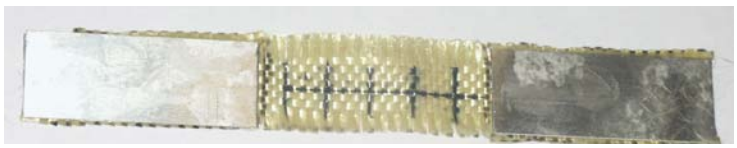

(a)

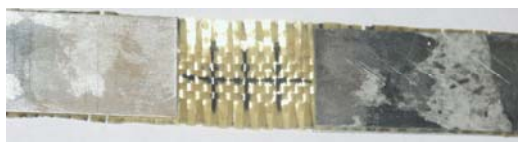

(b)

Figure 40. Constructed Test Specimens: (a) 2″ and (b) 1″ G.L.s

The high strain rate test setup is presented in figure 41. It consisted of a piezoelectric force link (load washer), two grips, a test specimen, a slack adaptor, and a Phantom high-speed digital camera with two high-intensity lamps. A specimen was placed in the upper and lower grips. Acceleration was imposed on the lower grip through the slack adaptor until the constant velocity was achieved. The slack adaptor has a hollow tube and a sliding bar. When the machine is in operation, the hollow tube travels freely with the actuator over a distance to reach a specified velocity before making contact with the cone-shaped surface of the sliding bar. The slack adaptor eliminates the inertia effect of the lower grip and actuator in its acceleration stage.

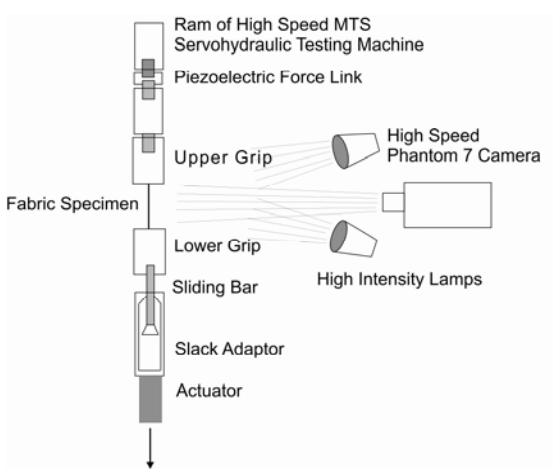

Figure 41. High Strain Rate Test Setup

3.3.2 Typical Stress-Strain Curve of Kevlar Fabric and Captured Images.

The signals from the load washer (LVDT of the actuator) were recorded at a 1-MHz sampling rate. These signals contain high-frequency noise, which requires filtering prior to obtaining the response of the test specimen. During the data processing, a low-pass filter with a cutoff frequency of 3 kHz was used to eliminate this noise. Figure 42 shows the stress-strain response of a test specimen obtained from a typical test. The behavior of the fabric has four distinct regions during loading: crimp, elastic, nonlinear failure, and post-peak. In the crimp region, the stress-strain graph shows a relatively large increase in strain for a very small increase in load. Woven fabrics inherently have crimp, and in this portion, the load essentially straightens the yarns by removing the crimp. As the load increases, the elastic region is approached, i.e., the straightened yarns start to take more load and the stress-strain graph exhibits an increased slope. Prior to the ultimate strength, the stress-strain response exhibits nonlinearity (nonlinear failure region), perhaps due to formation of the localized damage in yarns, and a rapid decrease in the stress beyond the ultimate strength that is characteristic of progressive yarn failure (post-peak region).

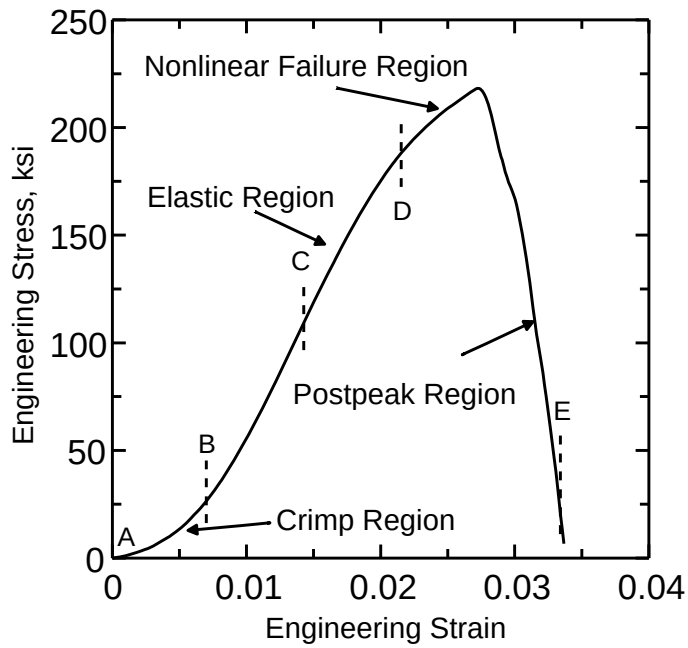

Figure 42. Four Regions of Stress-Strain Curve Obtained From a Typical Test

Using a Phantom 7.0 high-speed digital camera with 2-GB memory, tests can be recorded at a sample rate up to 15,000 frames per second (fps) with a 256- by 512-pixel resolution. In this work, the camera was set at 10,000 fps (time interval, 100 μs) with an exposure time of 95 μs and a resolution of 256 by 512 pixels. Two high-intensity lamps were used for illumination to capture high-quality images. Images taken at 100-μs intervals during a typical test are shown in figure 43 representing the stages of deformation during loading. A 25-mm G.L. specimen was tested at a nominal strain rate of 38 s^{-1} for a duration of about 0.9 ms. The nominal strain rate was calculated by dividing the actuator velocity (prior to loading the specimen) by the gage length of test specimen, as in equation 14.

$$\dot{\varepsilon}_{nominal} = \frac{V}{L} \tag{14}$$

Where V is the velocity of actuator prior to loading test specimen and L is the gage length of test specimen. As the sample was loaded, there was a uniform stretching of the fiber until the specimen failed. Various points identified as stage A through E in figure 42 correspond to the stage of the failure in the fabric.

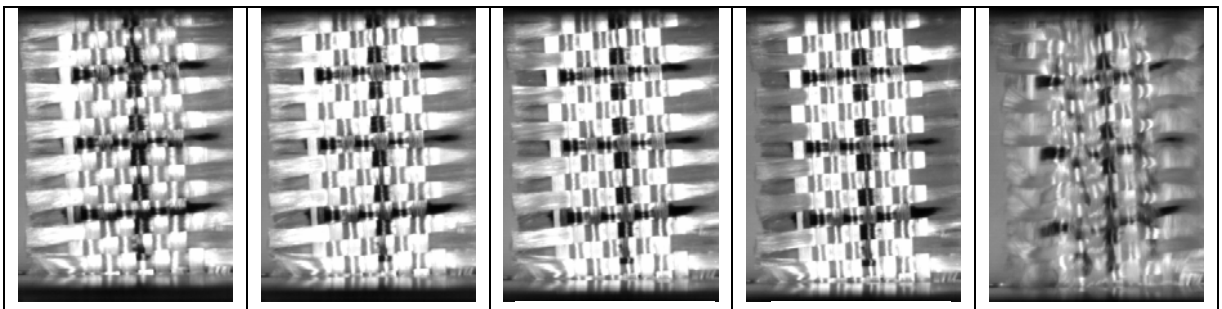

A = 0 ms	B = 0.2 ms	C = 0.4 ms	D = 0.6 ms	E = 0.9 ms

Figure 43. Images of 25-mm G.L. Specimens at a Nominal Strain Rate of 38 s^{-1}

3.3.3 Image Analysis of High Strain Rate Test.

3.3.3.1 Image Analysis Method.

To obtain an independent measure of strain distribution apart from the stroke displacement, images captured by the high-speed digital camera were analyzed. Five lines were marked on each specimen with a 2″ G.L. along the fill yarn direction at 0.375″ intervals, defining four sections, as shown in figure 44(a). For each specimen with a 1″ G.L., two sections, at 0.25″ intervals, were defined by three marked lines, as shown in figure 44(b). Deformation can be calculated using the images of the specimen at different time steps. Two images at two different moments were chosen: (1) the time when the specimen starts to deform and (2) the time corresponding to the last image before the specimen disintegrated. A MATLAB program was developed that uses image analysis to calculate the strain at each marked section by comparing these two images. Six points were chosen along each marked line in the fill yarn direction to obtain the coordinates of the chosen location in the first image, and similarly in the second image. By comparing the coordinate changes at each location, the deformation field and overall average strain can be obtained.

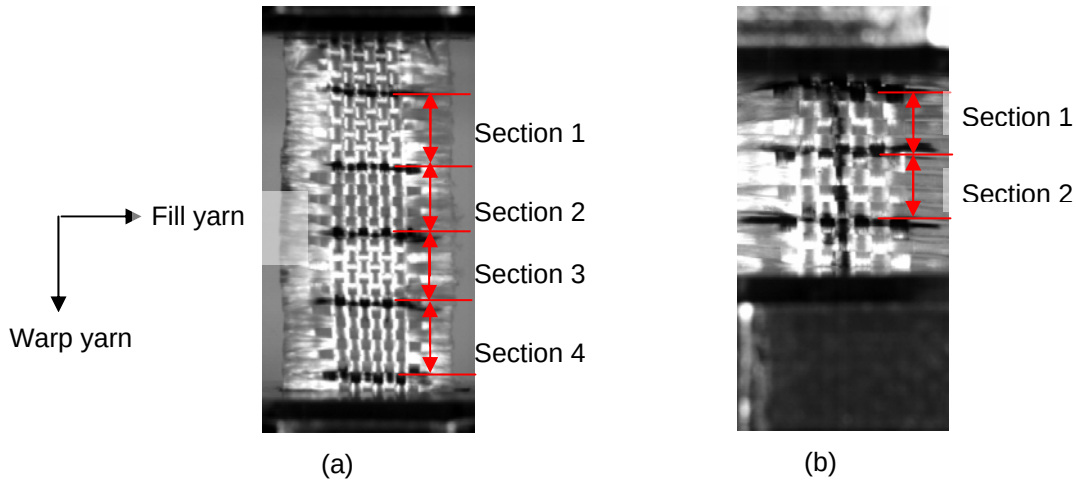

Figure 44. Specimen Sections: (a) 2″ and (b) 1″ G.L.s

The average strain rate from the image analysis can be calculated from the overall average strain rate, following equation 15.

$$\dot{\varepsilon}_{image} = \frac{\varepsilon_{image}}{T} \tag{15}$$

where ε_{image} is the overall average strain from the image analysis ($\dot{\varepsilon}_{image}$ is the strain rate from the image analysis algorithm) and T is the test duration.

In addition to the nominal strain rate, it is necessary to obtain the strain rate during specimen loading, hereinafter named the actual strain rate. The actual strain rate is defined as the maximum strain of the test specimen measured by the actuator LVDT, divided by the duration of the test, following equation 16.

$$\dot{\varepsilon}_{actual} = \frac{\varepsilon}{T} \tag{16}$$

where ε is the maximum strain measured by the actuator, LVDT and T is the test duration.

3.3.3.2 Image Analysis Results and Discussion.

The following sections discuss the results of the image analysis.

3.3.3.2.1 Comparison of Maximum Strain Between Image Analysis and LVDT Measurement.

By using the image analysis method, the average maximum strain can be calculated at each investigated strain rate, as shown in figure 45(a). The average maximum strain of the image analysis increases from 0.025 to 0.041 when the nominal strain rate increases from 25 to 170 s^{-1}. Figure 45(b) shows the correlation between the average maximum strain of the image analysis and the maximum strain of the LVDT measurement. The vertical error bars represent the

standard deviation of average maximum strain of image analysis at each level of strain rate. There is good correlation between the LVDT measurement and the image analysis results.

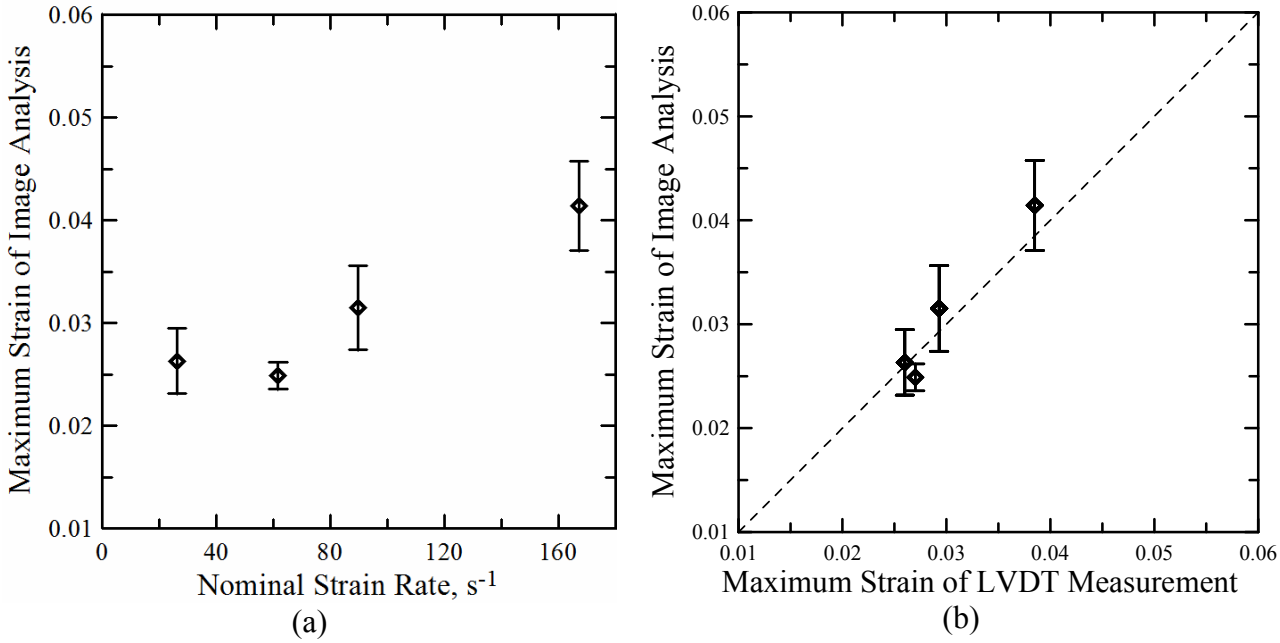

Figure 45. (a) Maximum Strain of Image Analysis vs Nominal Strain Rate and (b) Correlation of Maximum Strain Between Image Analysis and LVDT Measurement

3.3.3.2.2 Comparison of Strain Rate Between Image Analysis and LVDT Measurement.

Figure 46(a) shows the correlation between the average strain rate measured by image analysis and nominal strain rate, while figure 46(b) shows the correlation between the average strain rate measured by image analysis and actual strain rate. The vertical error bars in the graph represent standard deviation of the average strain rate measured by image analysis. When the nominal strain rate is below 40 s^{-1}, nominal strain rate, actual strain rate, and the average strain rate measured by image analysis are almost identical. When the strain rate is higher than 40 s^{-1}, the nominal strain rate is higher than the strain rate measured by image analysis. The average strain rate measured by image analysis matches the actual strain rate quite well. One possible reason that the nominal strain rate is lower than both the actual strain rate and the strain rate measured by image analysis is that the nominal strain rate is calculated based on the actuator velocity before the specimen is loaded. This velocity is actually higher than the actual actuator velocity during specimen loading because the reaction force of the specimen slows down the actuator.

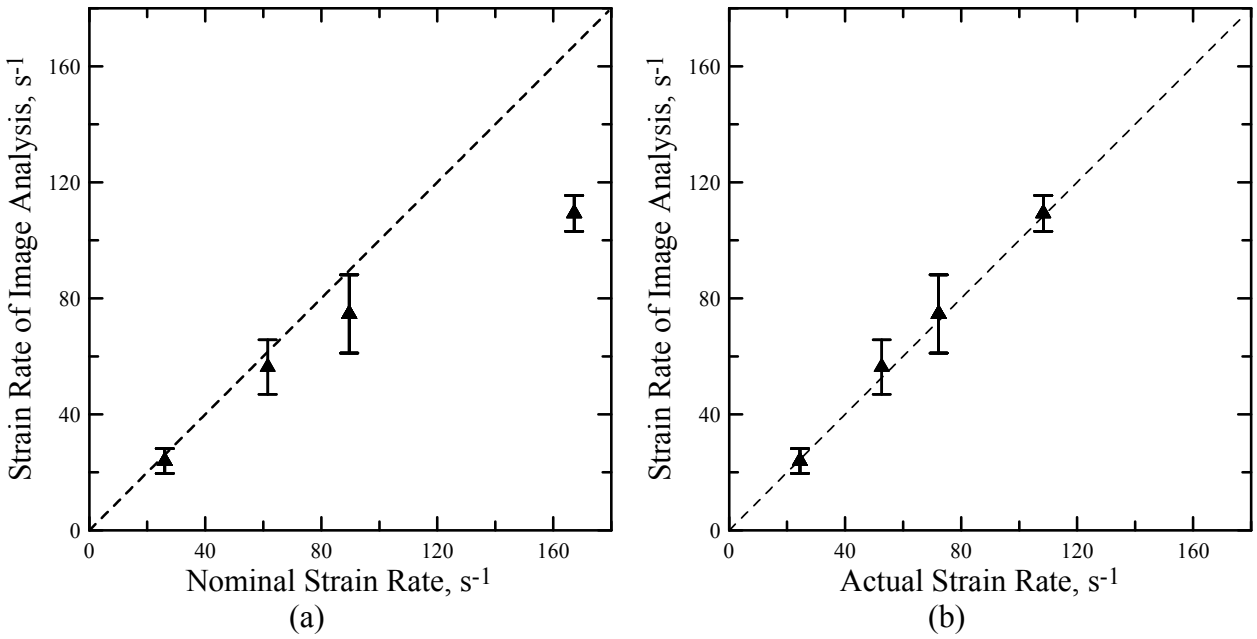

Figure 46. Correlation of Strain Rates Between Image Analysis and LVDT Measurement: (a) Strain Rate of Image Analysis vs Nominal Strain Rate and (b) Strain Rate of Image Analysis vs Actual Strain Rate

3.3.3.2.3 Comparison of Stress-Strain Curves Based on Image Analysis and LVDT Measurement.

As previously discussed, the maximum strain value could be obtained by image analysis; therefore, the strain time history of each test could be obtained by assuming a linear increment of strain value from zero to the maximum strain. Since the stress time history is known from the force time history calculation, the stress-strain curve at a different strain rate could be constructed based on strain values from the image analysis. Figure 47(a-d) shows comparisons of four typical sets of stress-strain curves based on the strain values measured by image analysis and LVDT at nominal strain rates of 21, 68, 101, and 170 s^{-1}, respectively. At a nominal strain rate of 21 s^{-1}, the maximum strain from the image analysis is about 0.025, which is quite close to the strain value (0.026) of the LVDT measurement, as shown in figure 47(a). At a nominal strain rate of 68 s^{-1}, the maximum strain from the image analysis is about 0.023, which is slightly lower than the LVDT measurement, as shown in figure 47(b). One possible reason is that the time interval of the images used for analysis is 0.1 ms, while the whole test duration is about 1 ms. Because, there are only about ten images recording the deformation history of the test specimen, the two images used for analysis might not exactly represent the start of deformation and the end of failure. There is negligible difference in the stress-strain curves in figure 47(c) and (d). Overall, the stress-strain curves based on image analysis agree well with those based on LVDT measurement.

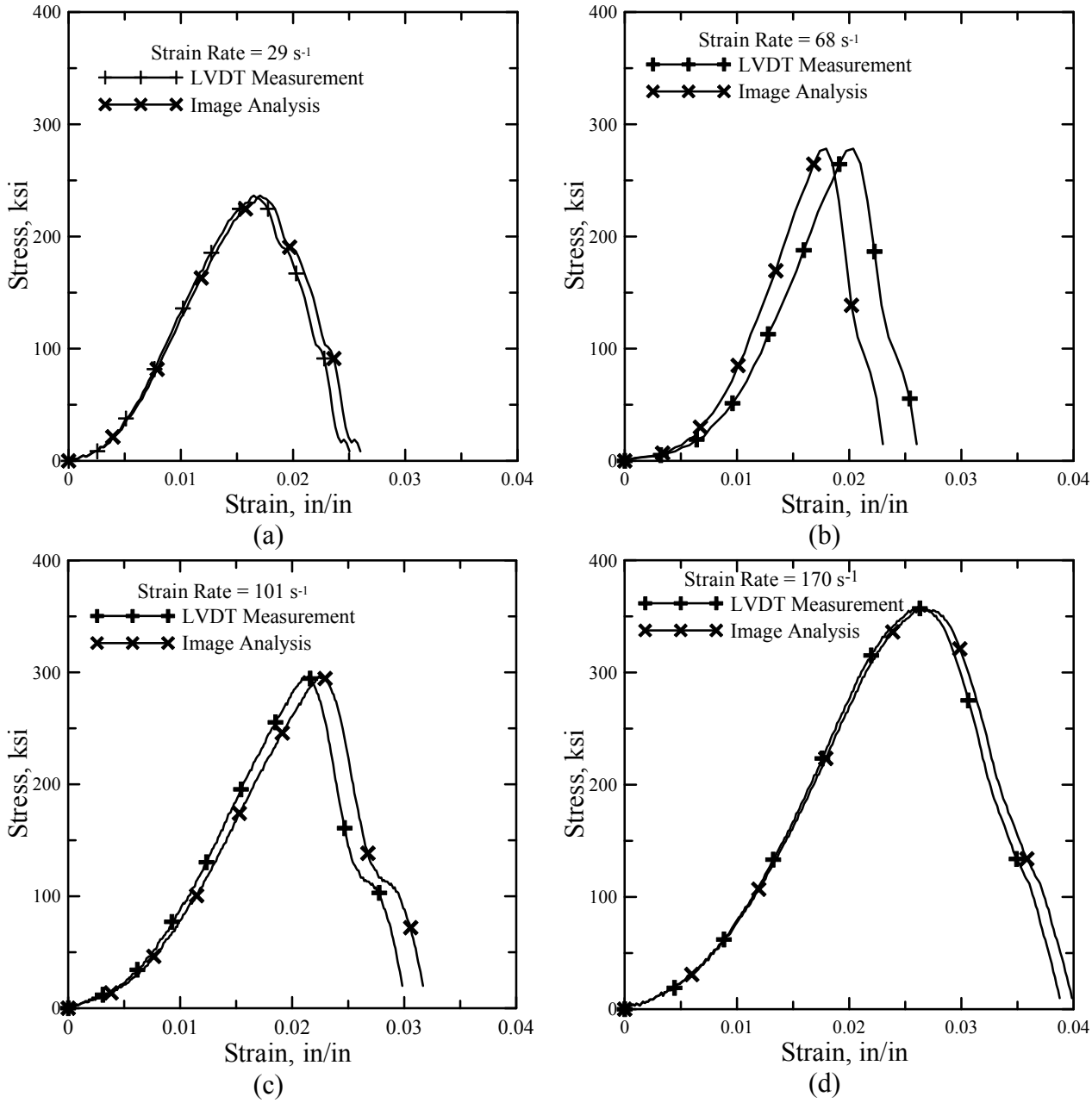

Figure 47. Comparison of Stress-Strain Curves Obtained by LVDT and Image Analysis at Nominal Strain Rates of (a) 21 s^{-1}, (b) 68 s^{-1}, (c) 101 s^{-1}, and (d) 170 s^{-1}

3.3.4 Kevlar Fabric Test Results and Discussion.

3.3.4.1 Response of 2″ G.L. Fabric Specimens.

Figures 48 to 50 show the stress time history and stress-strain curves of 2″ G.L. specimens at strain rates of 28, 66, and 96 s^{-1}. The tests were conducted in April 2007. At a strain rate of 28 s^{-1}, the average Young's modulus (computed based on these tests) was 21,264 ksi, the average tensile strength was 241 ksi, the average maximum strain was 0.028 in/in, the average ultimate

strain was 0.017 in/in, and the average toughness was 3,591 psi. The parameters for these samples are listed in table 9. At a strain rate of 66 s^{-1}, the average Young's modulus was 21,986 ksi, the average tensile strength was 277 ksi, the average maximum strain was 0.027 in/in, the average ultimate strain was 0.021 in/in, and the toughness was 2,909 psi. The parameters for these samples are listed in table 10. At a strain rate of 96 s^{-1}, the average Young's modulus was 22,561 ksi, the average tensile strength was 298 ksi , the average maximum strain was 0.028 in/in, the average ultimate strain was 0.019 in/in, and the average toughness was 3,720 psi. The parameters for these samples are listed in table 11.

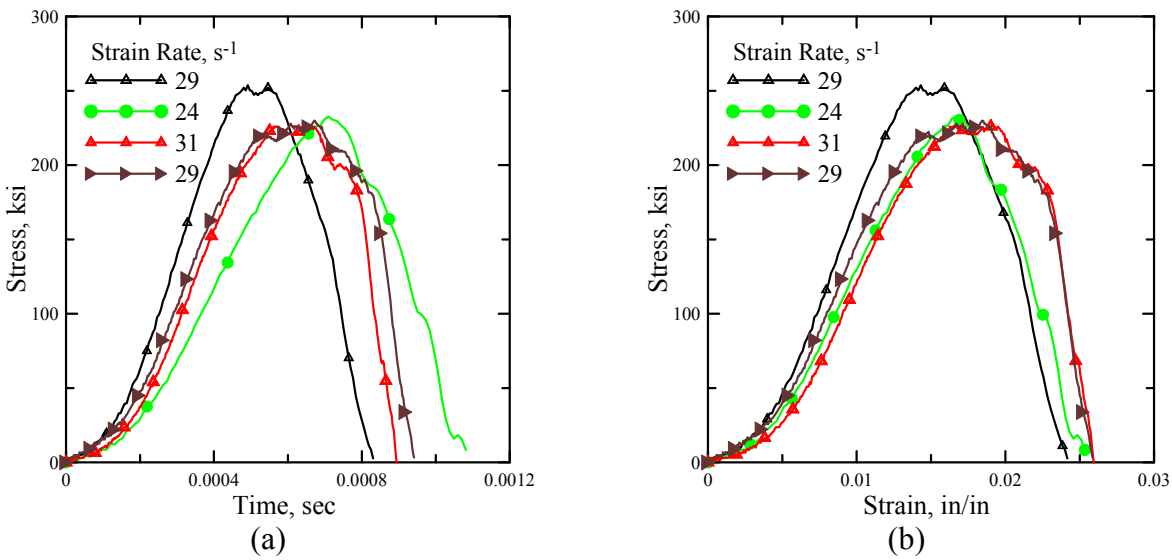

Figure 48. Response of 2″ Fabric at a Strain Rate of 28 s^{-1}: (a) Stress vs Time and (b) Stress vs Strain

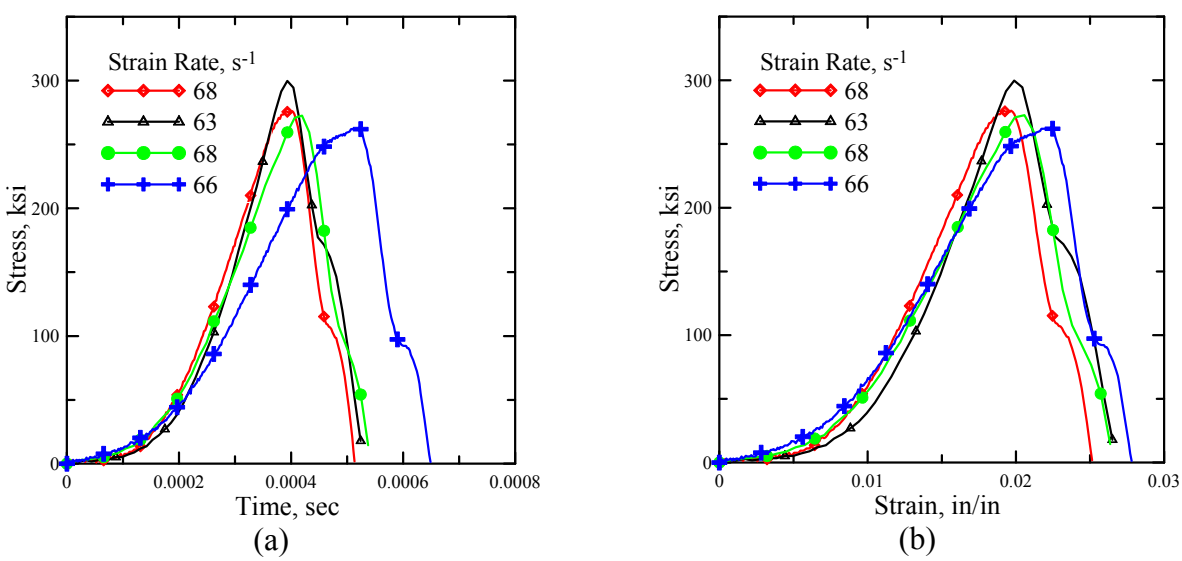

Figure 49. Response of 2″ Fabric at a Strain Rate of 66 s^{-1}: (a) Stress vs Time and (b) Stress vs Strain

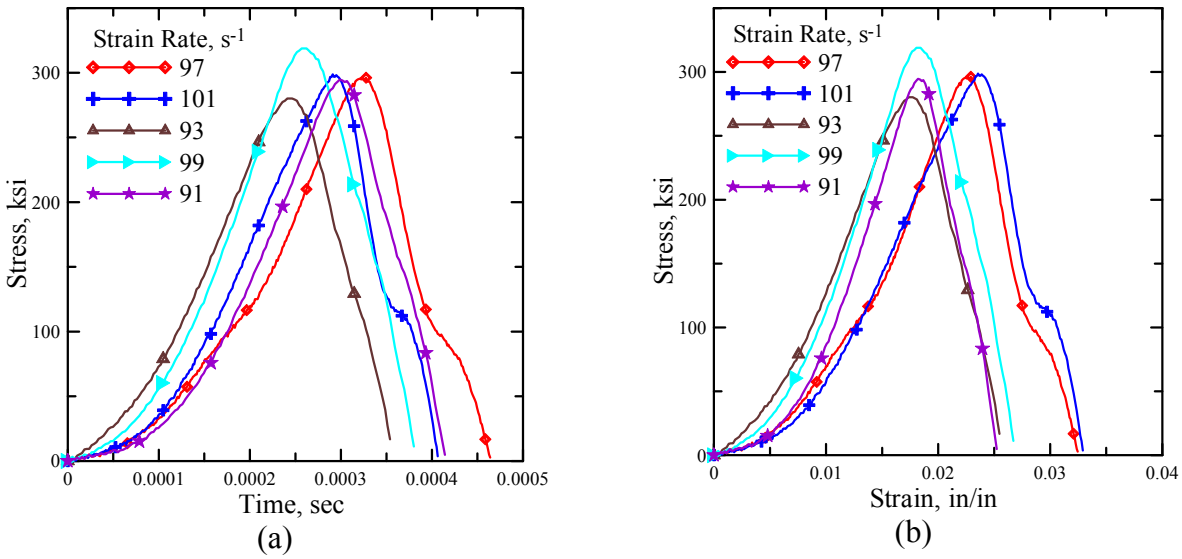

Figure 50. Response of 2″ Fabric at a Strain Rate of 96 s^{-1}: (a) Stress vs Time and (b) Stress vs Strain

Table 9. Summary of 2″ Fabric Tests at a Strain Rate of 28 s^{-1}

Test No.	Strain Rate (/s)	Young's Modulus (ksi)	Tensile Strength (ksi)	Maximum Strain (in/in)	Ultimate Strain (in/in)	Toughness (psi)
1	29	20,395	215	0.032	0.017	4168
2	24	18,408	265	0.030	0.020	4293
3	31	24,724	250	0.024	0.014	3101
4	29	21,529	232	0.025	0.017	2802
Average	28	21,264	241	0.028	0.017	3591
Standard deviation	3	2,643	22	0.004	0.003	750

Table 10. Summary of 2″ Fabric Tests at a Strain Rate of 66 s^{-1}

Test No.	Strain Rate (/s)	Young's Modulus (ksi)	Tensile Strength (ksi)	Maximum Strain (in/in)	Ultimate Strain (in/in)	Toughness (psi)
1	68	22,481	273	0.027	0.021	2895
2	63	20,953	263	0.028	0.022	3130
3	68	22,208	300	0.027	0.020	2819
4	66	22,304	273	0.027	0.021	2791
Average	66	21,986	277	0.027	0.021	2909
Standard deviation	2	698	16	0.001	0.001	154

Table 11. Summary of 2″ Fabric Tests at a Strain Rate of 96 s^{-1}

Test No.	Strain Rate (/s)	Young's Modulus (ksi)	Tensile Strength (ksi)	Maximum Strain (in/in)	Ultimate Strain (in/in)	Toughness (psi)
1	97	22,575	296	0.032	0.023	3807
2	101	21,211	297	0.030	0.021	3879
3	93	20,277	281	0.025	0.017	3775
4	99	24,825	319	0.027	0.018	3867
5	91	23,916	298	0.025	0.018	3273
Average	96	22,561	298	0.028	0.019	3720
Standard deviation	4	1,871	13	0.003	0.002	254

Figure 51 shows the stress time history and stress-strain curves of a 2″ fabric specimen at a strain rate of 91 s^{-1}. The tests were conducted in July 2007. The average Young's modulus (computed based on these tests) was 24,633 ksi, the average tensile strength was 298 ksi, the average maximum strain was 0.026 in/in, the average ultimate strain was 0.018 in/in, and the toughness was 3,445 psi. The parameters for these samples are listed in table 12.

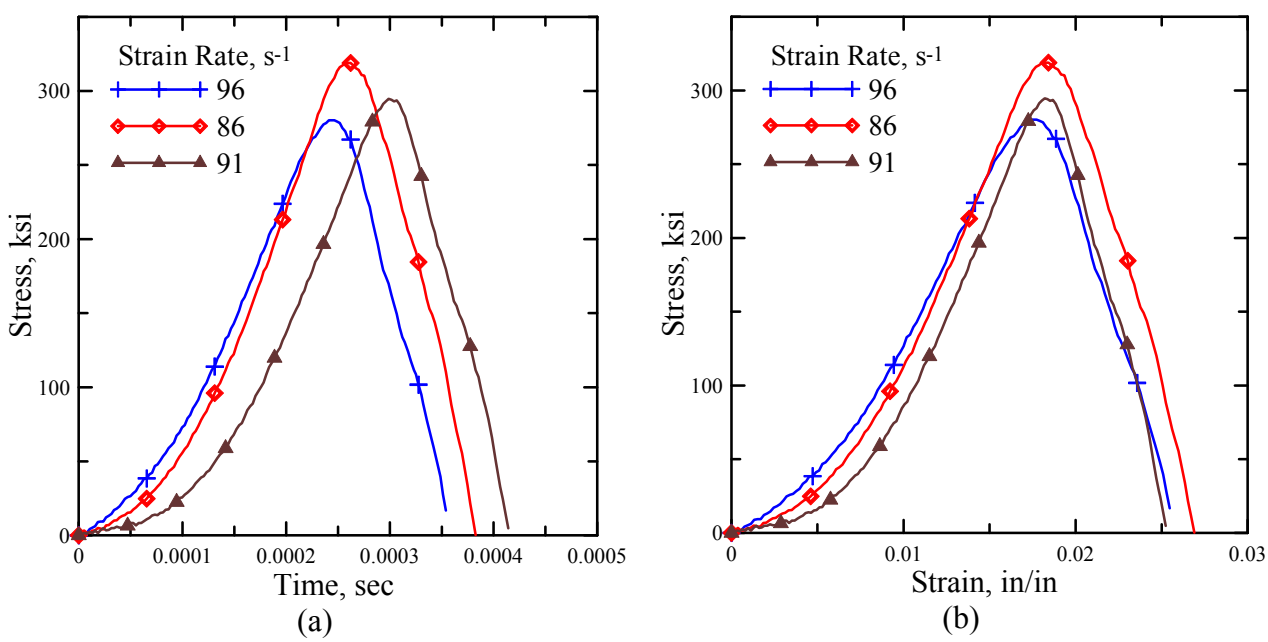

Figure 51. Response of 2″ Fabric at a Strain Rate of 91 s^{-1}: (a) Stress vs Time and (b) Stress vs Strain

Table 12. Summary of 2″ Fabric Tests at a Strain Rate of 91 s^{-1}

Test No.	Strain Rate (/s)	Young's Modulus (ksi)	Tensile Strength (ksi)	Maximum Strain (in/in)	Ultimate Strain (in/in)	Toughness (psi)
1	96	22,939	280	0.025	0.017	3433
2	86	24,825	319	0.027	0.018	3867
3	91	26,135	295	0.025	0.018	3036
Average	91	24,633	298	0.026	0.018	3445
Standard deviation	5	1,607	20	0.001	0.001	416

Figures 52 and 53 show the stress time history and stress-strain curves at a strain rate of 19 and 55 s^{-1}, respectively. The tests were conducted in April 2008. At a strain rate of 19 s^{-1}, the average Young's modulus was 17,317 ksi, the average tensile strength was 228 ksi, the average maximum strain was 0.031 in/in , the average ultimate strain was 0.021 in/in, and the toughness was 4,011 psi. The parameters for these samples are listed in table 13. At a strain rate of 55 s^{-1}, the average Young's modulus was 17,984 ksi, the average tensile strength was 286 ksi, the average maximum strain was 0.030 in/in, the average ultimate strain was 0.023 in/in, and the toughness was 3,898 psi. The parameters for these samples are listed in table 14.

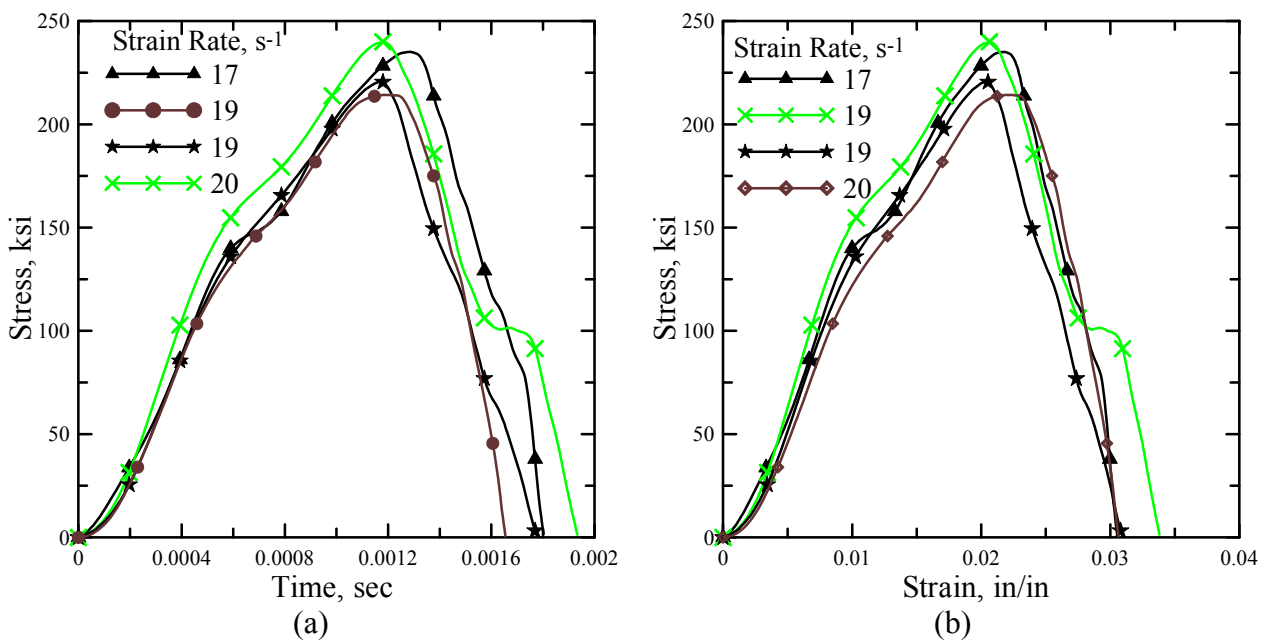

Figure 52. Response of 2″ Fabric at a Strain Rate of 19 s^{-1}: (a) Stress vs Time and (b) Stress vs Strain

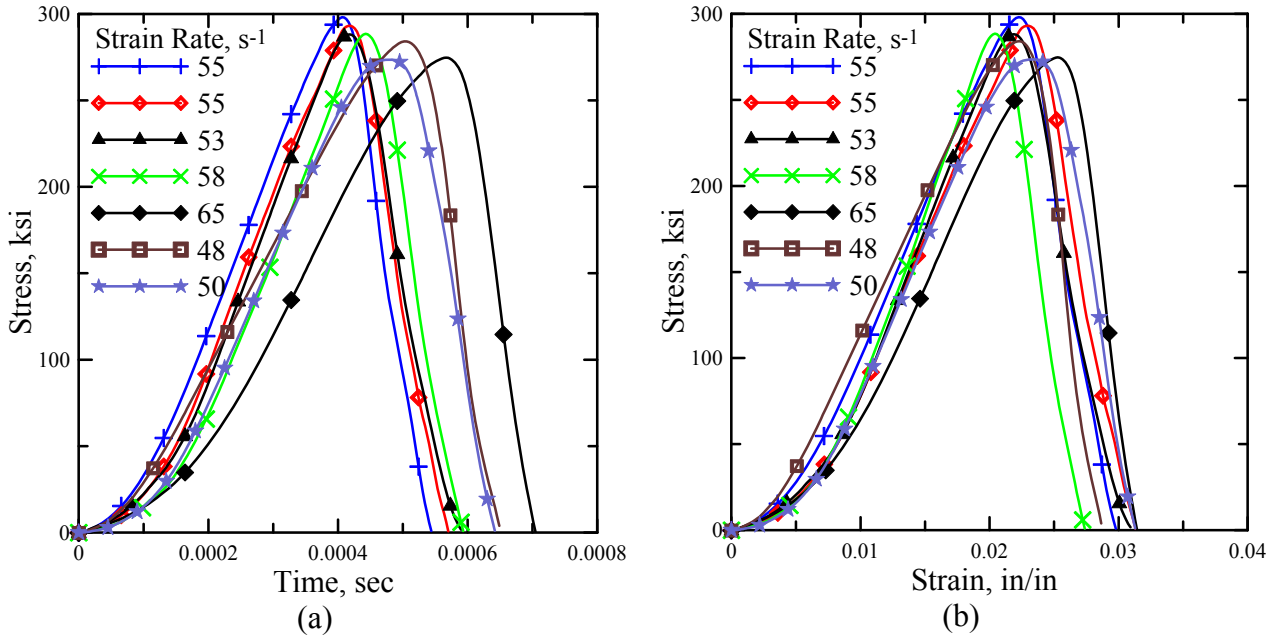

Figure 53. Response of 2″ Fabric at a Strain Rate of 55 s^{-1}: (a) Stress vs Time and (b) Stress vs Strain

Table 13. Summary of 2″ Fabric Tests at a Strain Rate of 19 s^{-1}

Test No.	Strain Rate (/s)	Young's Modulus (ksi)	Tensile Strength (ksi)	Maximum Strain (in/in)	Ultimate Strain (in/in)	Toughness (psi)
1	17	17,312	221	0.031	0.020	3665
2	19	16,316	214	0.031	0.022	3800
3	19	17,069	235	0.031	0.022	4102
4	20	18,571	240	0.034	0.021	4476
Average	19	17,317	228	0.031	0.021	4011
Standard deviation	1	937	12	0.002	0.001	360

Table 14. Summary of 2″ Fabric Tests at a Strain Rate of 55 s^{-1}

Test No.	Strain Rate (/s)	Young's Modulus (ksi)	Tensile Strength (ksi)	Maximum Strain (in/in)	Ultimate Strain (in/in)	Toughness (psi)
1	55	17,143	298	0.030	0.022	4063
2	55	18,186	293	0.031	0.023	4014
3	53	19,977	288	0.031	0.022	3829
4	58	20,265	288	0.027	0.020	3273
5	65	16,282	275	0.031	0.025	3982
6	48	16,353	284	0.029	0.022	4033
7	50	17,683	274	0.031	0.023	4094
Average	55	17,984	286	0.030	0.023	3898
Standard deviation	6	1,611	9	0.002	0.001	289

3.3.4.2 Response of 1″ G.L. Fabric Specimens.

Figures 54 and 55 show the stress time history and stress-strain curves of 1″ G.L. specimens at strain rates of 113 and 167 s^{-1}, respectively. These tests were conducted in July 2007. At a strain rate of 113 s^{-1}, the average Young's modulus was 22,450 ksi, the average tensile strength was 309 ksi, the average maximum strain was 0.032 in/in, the average ultimate strain was 0.021 in/in, and the average toughness was 4,901 psi. The parameters for these samples are listed in table 15. At a strain rate of 167 s^{-1}, the average Young's modulus was 21,934 ksi, the average tensile strength was 356 ksi, the average maximum strain was 0.038 in/in, the average ultimate strain was 0.026 in/in, and the average toughness was 6,633 psi. The parameters for these samples are listed in table 16.

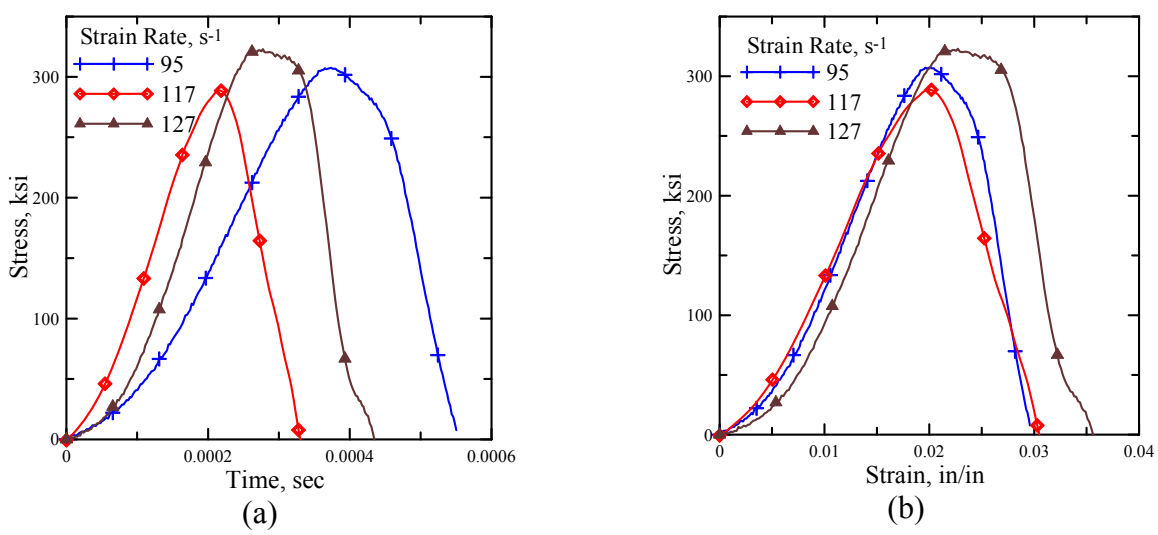

Figure 54. Response of 1″ Fabric at a Strain Rate of 113 s^{-1}: (a) Stress vs Time and (b) Stress vs Strain

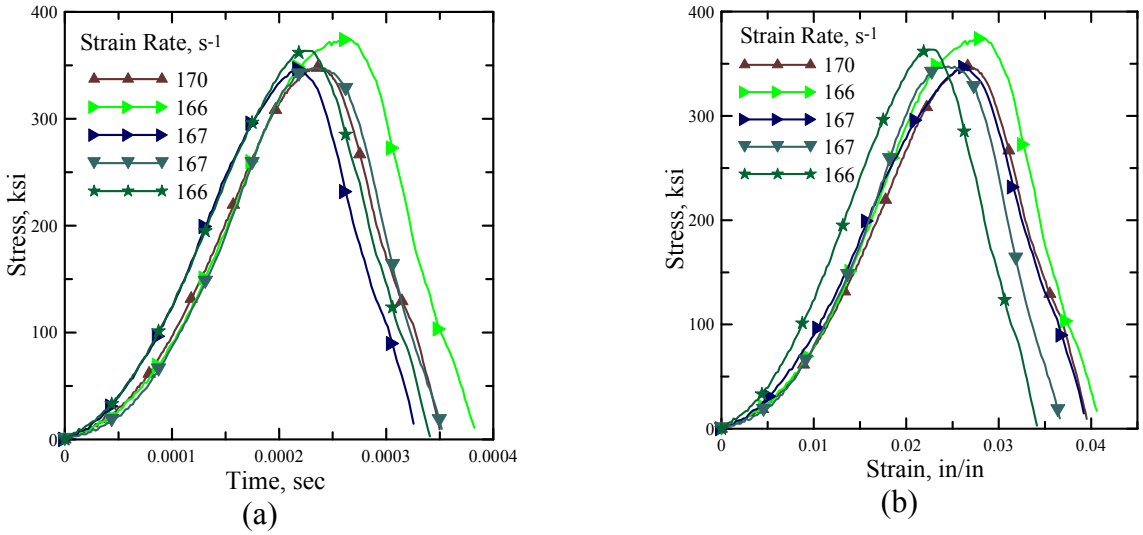

Figure 55. Response of 1″ Fabric at a Strain Rate of 167 s^{-1}: (a) Stress vs Time and (b) Stress vs Strain

Table 15. Summary of 1″ Fabric Tests at a Strain Rate of 113 s^{-1}

Test No.	Strain Rate (/s)	Young's Modulus (ksi)	Tensile Strength (ksi)	Maximum Strain (in/in)	Ultimate Strain (in/in)	Toughness (psi)
1	95	22,560	308	0.030	0.020	4693
2	117	22,117	297	0.029	0.019	4317
3	127	22,673	323	0.036	0.023	5693
Average	113	22,450	309	0.032	0.021	4901
Standard deviation	16	294	13	0.003	0.002	711

Table 16. Summary of 1″ Fabric Tests at a Strain Rate of 167 s^{-1}

Test No.	Strain Rate (/s)	Young's Modulus (ksi)	Tensile Strength (ksi)	Maximum Strain (in/in)	Ultimate Strain (in/in)	Toughness (psi)
1	170	20,735	348	0.040	0.027	6651
2	166	22,954	375	0.041	0.028	7505
3	167	20,860	347	0.039	0.026	6761
4	167	21,956	347	0.037	0.025	6106
5	166	23,164	363	0.034	0.022	6140
Average	167	21,934	356	0.038	0.026	6633
Standard deviation	2	1,134	13	0.003	0.002	570

Figures 56 and 57 show the stress time history and stress-strain curves of 1″ G.L. specimens at strain rates of 29 and 81 s^{-1}, respectively. The tests were conducted in April 2008. At a strain rate of 29 s^{-1}, the average Young's modulus was 16,693 ksi, the average tensile strength was 212 ksi, the average maximum strain was 0.029 in/in, the average ultimate strain was 0.021 in/in, and the average toughness was 3,476 psi. The parameters for these samples are listed in table 17. At a strain rate of 81 s^{-1}, the average Young's modulus was 16,836 ksi, the average tensile strength was 274 ksi, the average maximum strain was 0.035 in/in, the average ultimate strain was 0.022 in/in, and the average toughness was 4,391 psi. The parameters for these samples are listed in table 18.

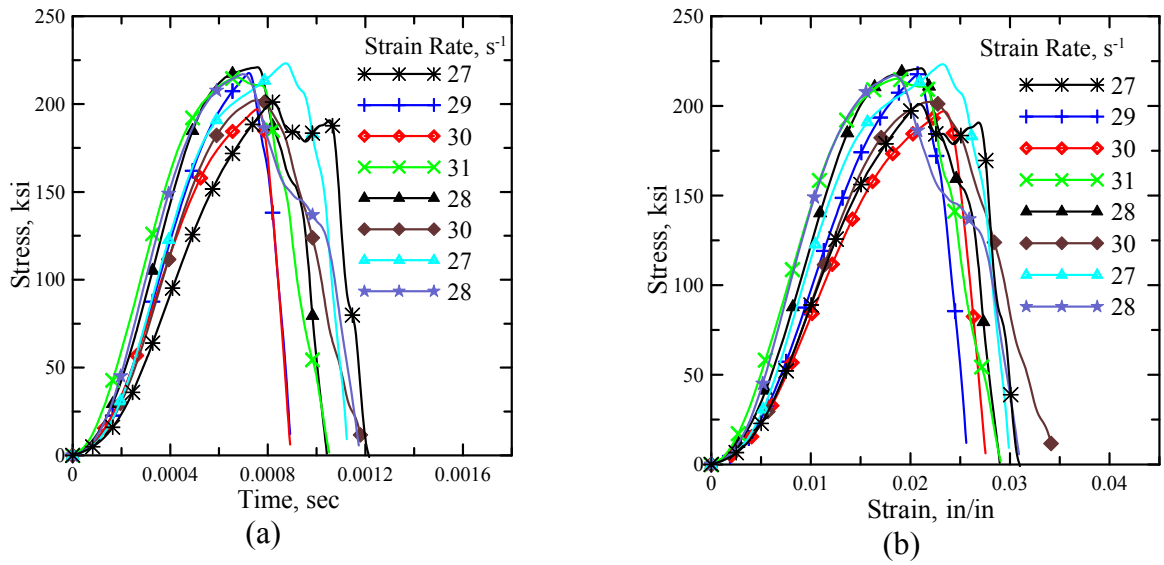

Figure 56. Response of 1″ Fabric at a Strain Rate of 29 s^{-1}: (a) Stress vs Time and (b) Stress vs Strain

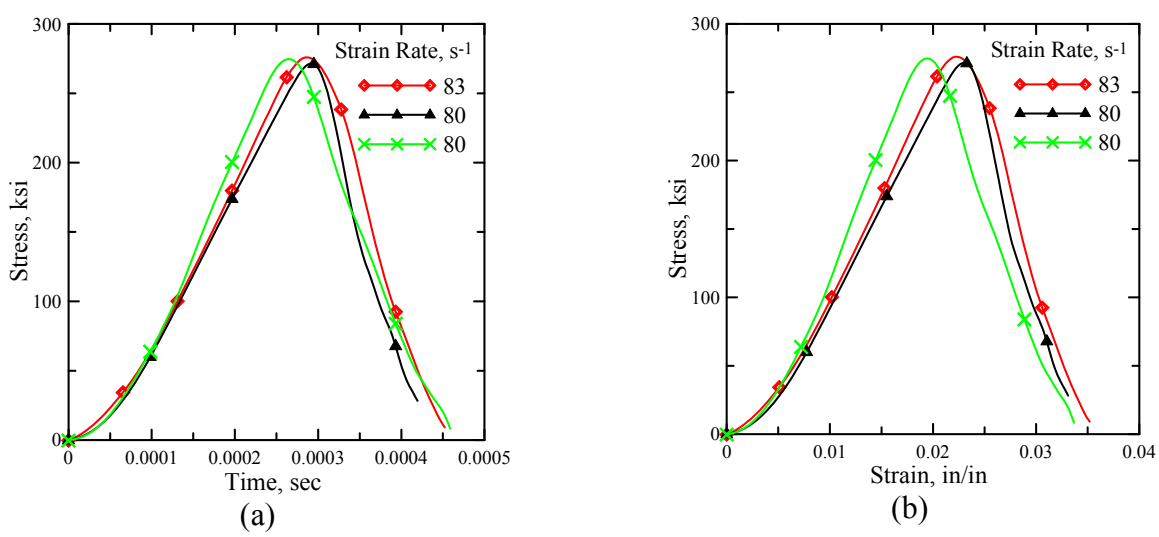

Figure 57. Response of 1″ Fabric at a Strain Rate of 81 s^{-1}: (a) Stress vs Time and (b) Stress vs Strain

Table 17. Summary of 1″ Fabric Tests at a Strain Rate of 29 s^{-1}

Test No.	Strain Rate (/s)	Young's Modulus (ksi)	Tensile Strength (ksi)	Maximum Strain (in/in)	Ultimate Strain (in/in)	Toughness (psi)
1	27	14,373	201	0.030	0.020	3494
2	29	15,462	218	0.026	0.021	2847
3	30	13,944	197	0.025	0.021	2651
4	31	18,726	221	0.029	0.021	3679
5	28	17,766	215	0.029	0.019	3663
6	30	15,557	202	0.035	0.022	3732
7	27	18,364	223	0.030	0.023	3876
8	28	19,353	217	0.031	0.018	3862
Average	29	16,693	212	0.029	0.021	3476
Standard deviation	1	2,101	10	0.003	0.002	467

Table 18. Summary of 1″ Fabric Tests at a Strain Rate of 81 s^{-1}

Test No.	Strain Rate (/s)	Young's Modulus (ksi)	Tensile Strength (ksi)	Maximum Strain (in/in)	Ultimate Strain (in/in)	Toughness (psi)
1	83	16,279	276	0.036	0.022	4658
2	80	15,064	272	0.033	0.023	4227
3	80	19,165	275	0.034	0.019	4288
Average	81	16,836	274	0.035	0.022	4391
Standard deviation	2	2,106	2	0.002	0.002	233

3.3.5 Key Parameters.

Figure 58(a-d) shows the dependence of the dynamic material properties, i.e., Young's modulus, tensile strength, maximum strain, and toughness on strain rates, respectively. The tests were conducted at two different G.L.s (L_0), which are shown in figure 58. There is an apparent dependence of the dynamic material properties on the strain rates.

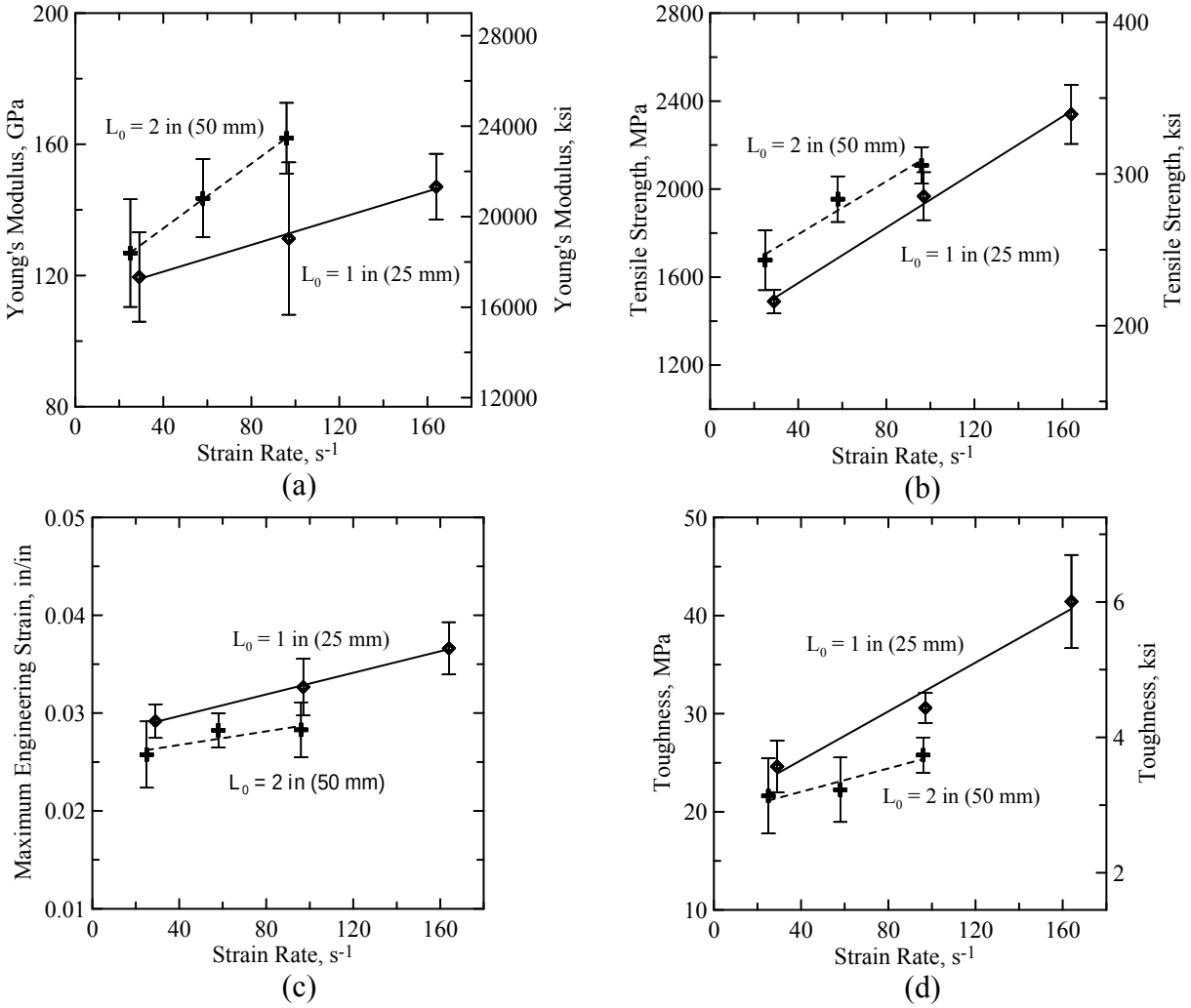

Figure 58. Strain Rate Effect on Dynamic Material Properties of Kevlar 49 Fabric: (a) Young's Modulus, (b) Tensile Strength, (c) Maximum Strain, and (d) Toughness

3.4 SINGLE YARN.

3.4.1 Specimen Preparation and Test Setup.

Similar to the fabric high-speed tests, thin aluminum sheets were glued with epoxy on both ends of the specimen to reduce the stress concentration at the gripping wedges. In these tests, only one yarn remained in the G.L. section, as shown in figure 59.

(a)

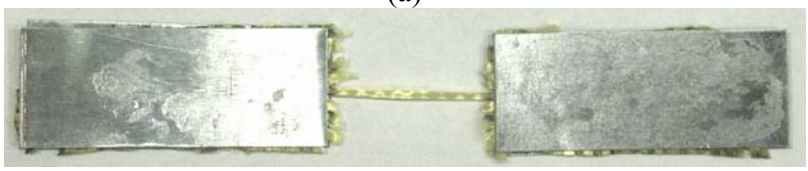

(b)

Figure 59. Single-Yarn Specimen: (a) 2″ and (b) 1″ G.L.s

The test specimen was assembled with the same gripping system that was used in the fabric test to ensure that the grip wedges were properly aligned while they were pressed in the socket. The grips were tightened from the end screw part using a torque wrench to ensure proper tightening. After placing the test specimen in a test frame, a Phantom high-speed camera was aligned to ensure that good-quality video could be obtained. The force and displacement data were recorded at a sampling rate of 1.0×10^6/s. Two low-pass filters were applied to eliminate signal noise. The cutoff frequency was 8 kHz for the displacement signal and 20 kHz for the force signal. A piezoelectric force link (Kistler 9041A, 20,000-lb capacity) and a dual-mode charge amplifier (Kistler 5010B) were used for the force measurement. In the technical data, the overall measuring ranges of the charge amplifier were given in pC for each 10V output voltage. The sensitivity was set at 18 pC/lb and the scale factor was set at 20 lb/V. The measurement resolution was limited by the charge amplifier floor noise, which was typically 5 milivolts. At 20-lb/V output scaling, the resolution was 20 lb/V × 0.005 V = 0.1 lb.

Figure 60(a) and (b) shows a single yarn captured by the high-speed camera during a test at a strain rate of 45 s^{-1}. The various markers A-F correlate the images with the stress-strain response. The sampling rate of the high-speed camera was set at 10,000 fps.

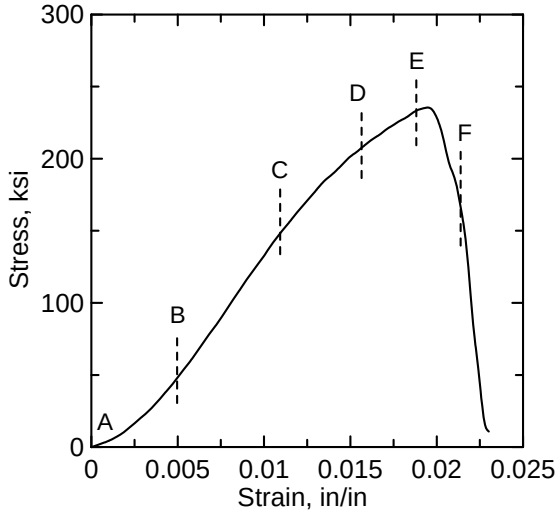

(a)

A = 0 ms B = 0.2 ms C = 0.4 ms D = 0.6 ms E = 0.7 ms F = 0.8 ms

(b)

Figure 60. (a) Stress-Strain Response of a Single Yarn and Identification of Points of Interest and (b) Twisted Yarn Images at a Strain Rate of 45 s^{-1} With a 100-μs Time Interval

3.4.2 Test Results and Discussion.

3.4.2.1 Response of 2″ G.L. Single-Yarn Specimens.

Figures 61 and 62 show the stress time history and stress-strain curves of 2″ G.L. single-yarn specimens at strain rates of 21 and 62 s^{-1}, respectively. At a strain rate of 21 s^{-1}, the average Young's modulus was 17,145 ksi, the average tensile strength was 229 ksi, the average maximum strain was 0.022 in/in , the average ultimate strain was 0.019 in/in, and the toughness was 2,726 psi. Table 19 lists these parameters for all the samples. At a strain rate of 62 s^{-1}, the average Young's modulus was 21,626 ksi, the average tensile strength was 274 ksi, the average maximum strain was 0.024 in/in, the average ultimate strain was 0.015 in/in, and the toughness was 3,417 psi. Table 20 lists these parameters for all the samples.

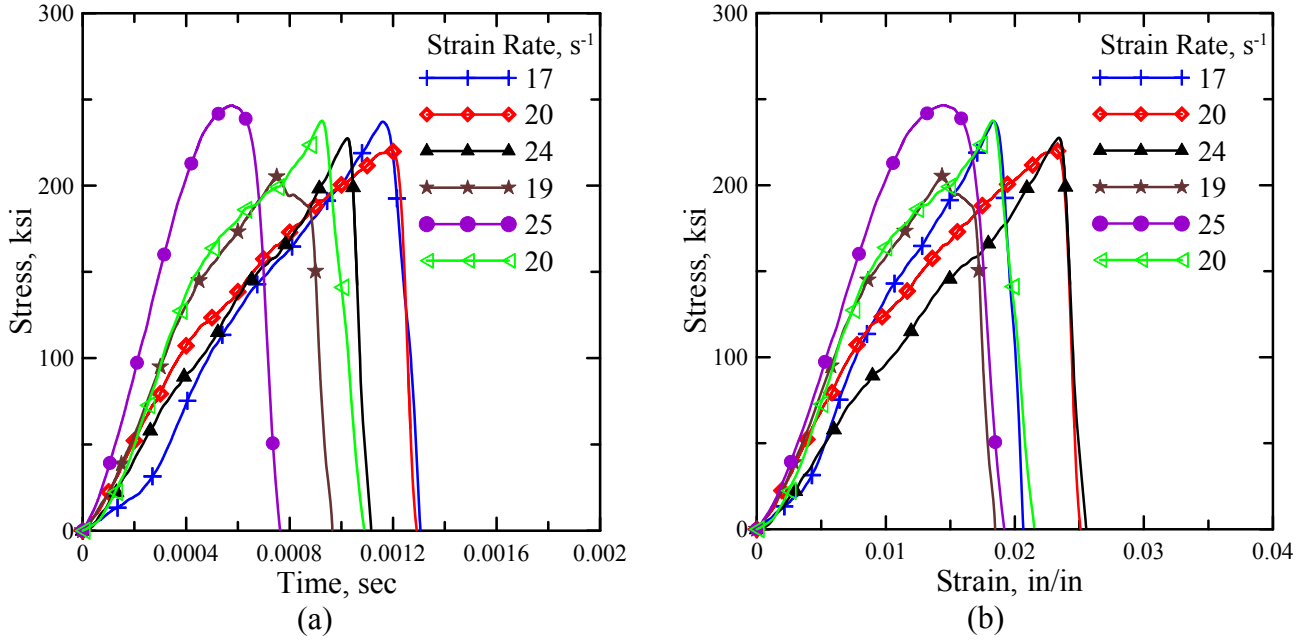

Figure 61. Response of 2″ Single Yarn at a Strain Rate of 21 s^{-1}: (a) Stress vs Time and (b) Stress vs Strain

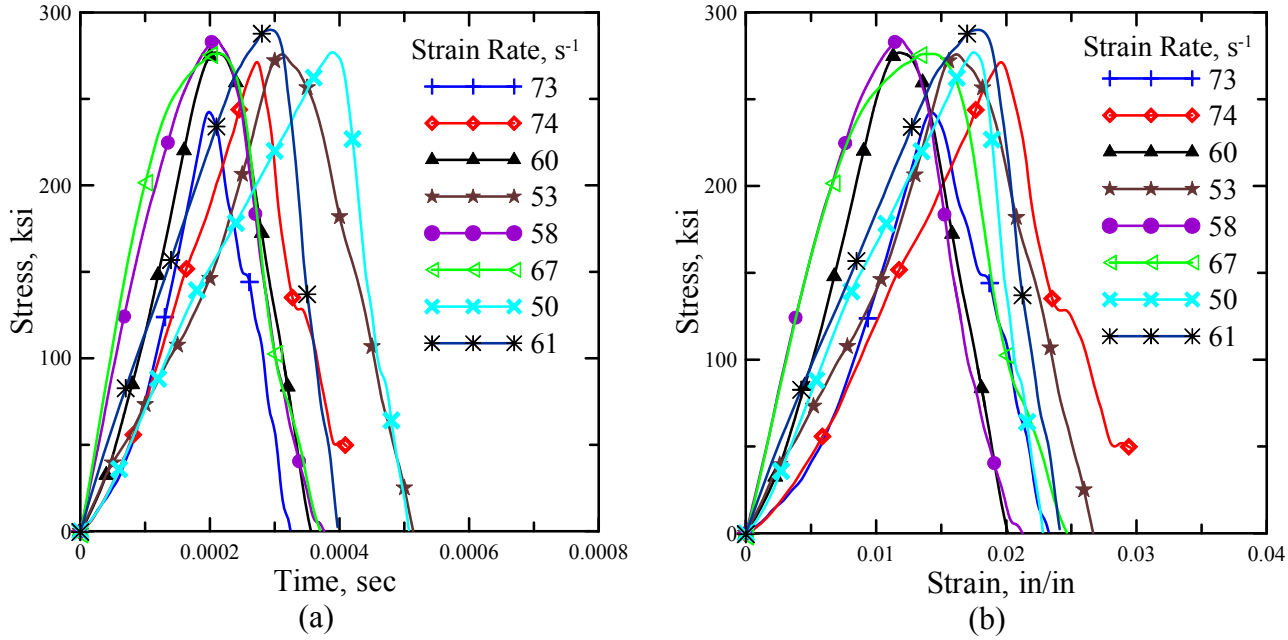

Figure 62. Response of 2″ Single Yarn at a Strain Rate of 62 s^{-1}: (a) Stress vs Time and (b) Stress vs Strain

Table 19. Summary of 2″ Single-Yarn Tests at a Strain Rate of 21 s^{-1}

Test No.	Strain Rate (/s)	Young's Modulus (ksi)	Tensile Strength (ksi)	Maximum Strain (in/in)	Ultimate Strain (in/in)	Toughness (psi)
1	17	13,444	237	0.021	0.018	2432
2	20	15,657	221	0.025	0.023	3271
3	24	12,455	228	0.026	0.023	2847
4	19	17,881	205	0.019	0.014	2217
5	25	22,736	246	0.019	0.014	2781
6	20	20,698	237	0.022	0.018	2809
Average	21	17,145	229	0.022	0.019	2726
Standard deviation	3	4,058	15	0.003	0.004	365

Table 20. Summary of 2″ Single-Yarn Tests at a Strain Rate of 62 s^{-1}

Test No.	Strain Rate (/s)	Young's Modulus (ksi)	Tensile Strength (ksi)	Maximum Strain (in/in)	Ultimate Strain (in/in)	Toughness (psi)
1	73	22,911	242	0.023	0.014	2491
2	74	16,285	271	0.030	0.020	3748
3	60	28,030	276	0.020	0.011	2893
4	53	14,132	275	0.027	0.016	3676
5	58	26,974	284	0.021	0.012	3289
6	67	30,336	276	0.024	0.014	4085
7	50	16,861	277	0.023	0.017	3249
8	61	17,478	290	0.024	0.018	3901
Average	62	21,626	274	0.024	0.015	3417
Standard deviation	9	6,230	14	0.003	0.003	539

3.4.2.2 Response of 1″ G.L. Single-Yarn Specimens.

Figures 63 through 65 show the stress versus time and stress versus strain curves of 1″ G.L. specimens at strain rates of 30, 47, and 100 s^{-1}, respectively. At a strain rate of 30 s^{-1}, the average Young's modulus was 15,823 ksi, the average tensile strength was 235 ksi, the average maximum strain was 0.025 in/in, the average ultimate strain was 0.021 in/in, and the toughness was 2,919 psi. Table 21 lists these parameters for all the samples. At a strain rate of 47 s^{-1}, the average Young's modulus was 16,000 ksi, the average tensile strength was 242 ksi, the average maximum strain was 0.026 in/in, the average ultimate strain was 0.019 in/in, and the toughness was 3,011 psi. Table 22 lists these parameters for all the samples. At a strain rate of 100 s^{-1}, the

average Young's modulus was 17,879 ksi, the average tensile strength was 247 ksi, the average maximum strain was 0.028 in/in, the average ultimate strain was 0.020 in/in, and the toughness was 3,754 psi. Table 23 lists these parameters for all the samples.

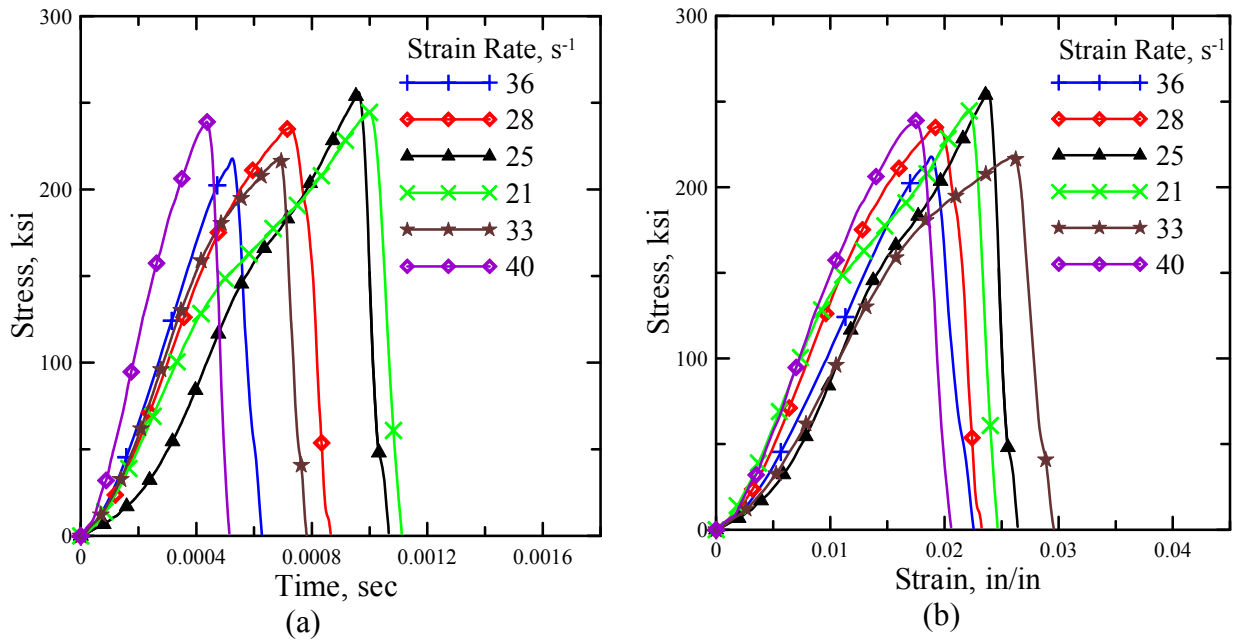

Figure 63. Response of 1″ Single Yarn at a Strain Rate of 31 s^{-1}: (a) Stress vs Time and (b) Stress vs Strain

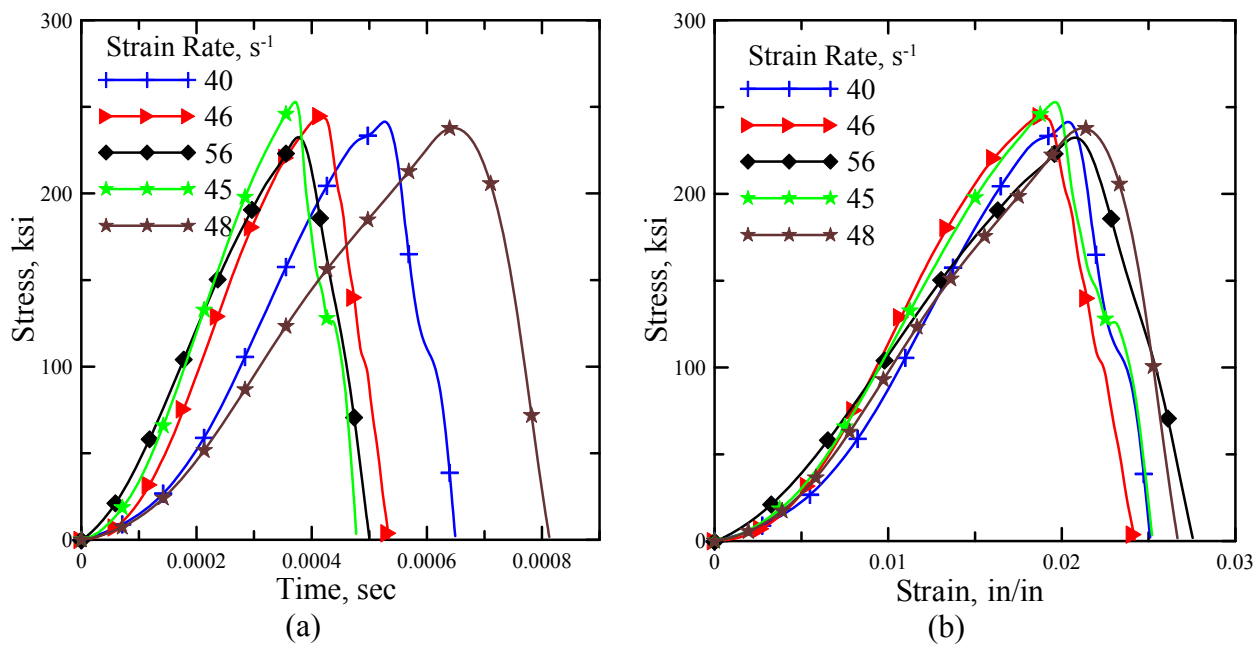

Figure 64. Response of 1″ Single Yarn at a Strain Rate of 47 s^{-1}: (a) Stress vs Time and (b) Stress vs Strain

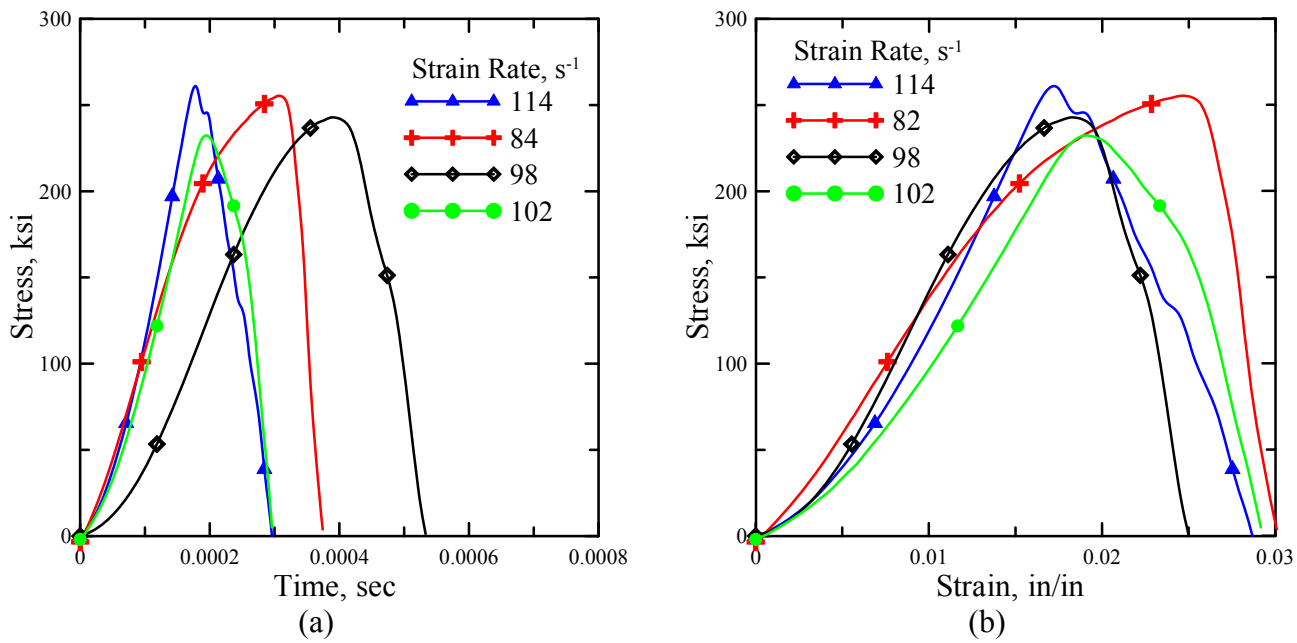

Figure 65. Response of 1″ Single Yarn at a Strain Rate of 100 s^{-1}: (a) Stress vs Time and (b) Stress vs Strain

Table 21. Summary of 1″ Single-Yarn Tests at a Strain Rate of 31 s^{-1}

Test No.	Strain Rate (/s)	Young's Modulus (ksi)	Tensile Strength (ksi)	Maximum Strain (in/in)	Ultimate Strain (in/in)	Toughness (psi)
1	36	14,477	218	0.023	0.019	2313
2	28	17,689	235	0.023	0.019	2912
3	25	14,975	256	0.026	0.024	3042
4	21	16,686	245	0.025	0.022	3272
5	33	13,737	218	0.029	0.026	3429
6	40	17,372	239	0.021	0.017	2545
Average	31	15,823	235	0.025	0.021	2919
Standard deviation	7	1,644	15	0.003	0.003	426

Table 22. Summary of 1″ Single-Yarn Tests at a Strain Rate of 47 s^{-1}

Test No.	Strain Rate (/s)	Young's aModulus (ksi)	Tensile Strength (ksi)	Maximum Strain (in/in)	Ultimate Strain (in/in)	Toughness (psi)
1	40	17,216	241	0.025	0.020	2779
2	46	17,010	245	0.024	0.019	2847
3	56	13,728	232	0.028	0.016	3266
4	45	16,890	253	0.025	0.020	2997
5	48	15,158	238	0.027	0.021	3164
Average	47	16,000	242	0.026	0.019	3011
Standard deviation	6	1,514	8	0.001	0.002	206

Table 23. Summary of 1″ Single-Yarn Tests at a Strain Rate of 100 s^{-1}

Test No.	Strain Rate (/s)	Young's Modulus (ksi)	Tensile Strength (ksi)	Maximum Strain (in/in)	Ultimate Strain (in/in)	Toughness (psi)
1	114	19,752	261	0.029	0.017	3590
2	98	19,088	243	0.025	0.018	3285
3	84	16,535	255	0.030	0.025	4617
4	102	16,140	230	0.029	0.019	3522
Average	100	17,879	247	0.028	0.020	3754
Standard deviation	12	1,807	14	0.002	0.004	590

3.4.3 Key Parameters Discussion and Summary.

Figure 66 shows the strain rate effect on Young's modulus, tensile strength, maximum strain, and toughness of a Kevlar 49 single yarn. The tests were conducted at two different G.L.s (L_0), which are shown in figure 66. There is an apparent dependence of the dynamic material properties on the strain rates.

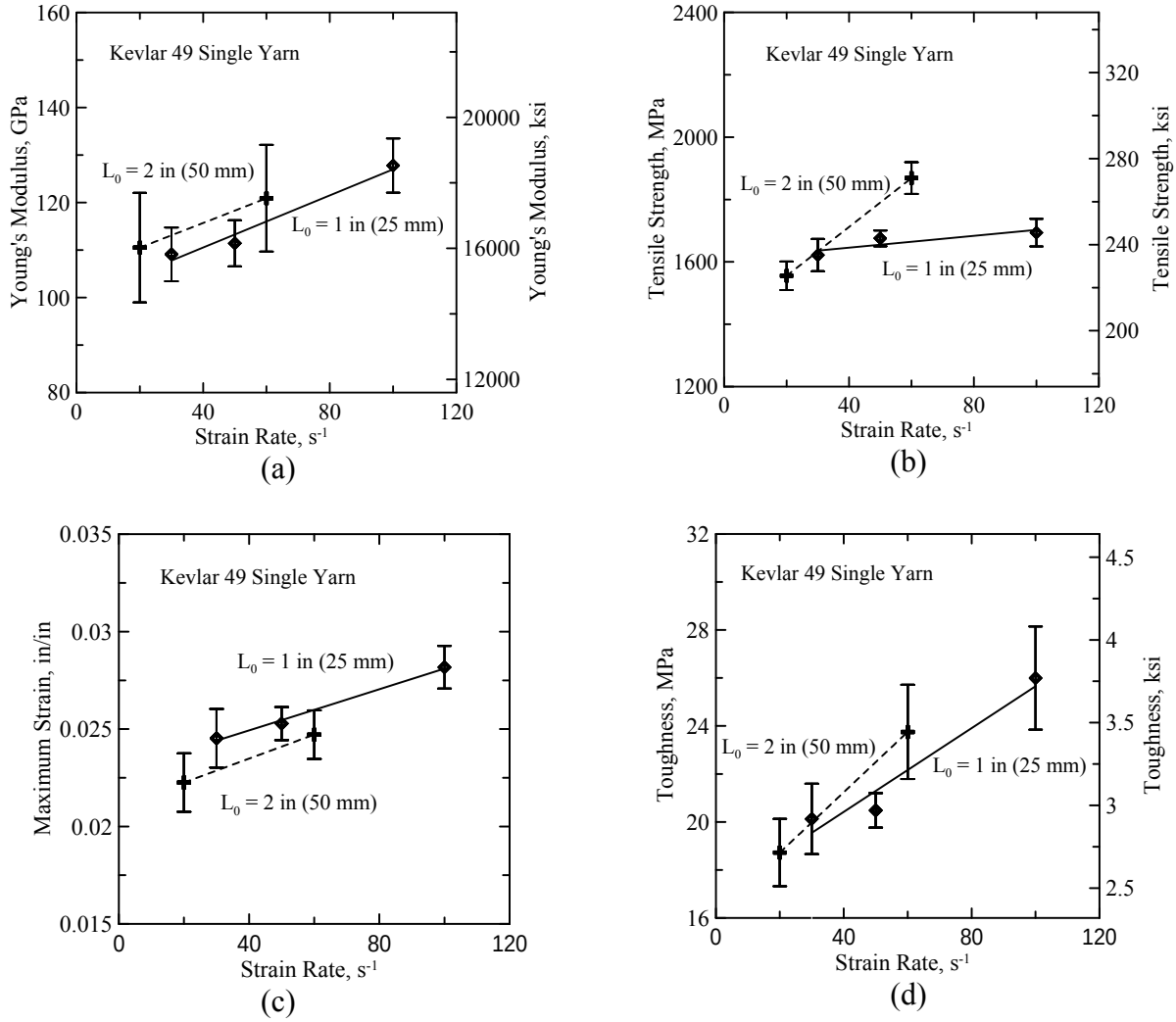

Figure 66. Strain Rate Effect on Dynamic Material Properties of Kevlar 49 Single Yarn: (a) Young's Modulus, (b) Tensile Strength, (c) Maximum Strain, and (d) Toughness

3.5 COMPARISON WITH PUBLISHED DATA.

Figure 67(a-d) shows the comparisons of Young's modulus, ultimate strength, maximum strain, and toughness values for Kevlar 49 fiber and fiber bundles available in published data with the values of single-yarn and fabric (8 yarns) specimens in this research. Only the average value of the test results in each strain rate category was plotted. There are very limited data available in the medium strain rate range. The Young's modulus of single yarn and fabric in the present study was higher than the value of a similar Kevlar 49 material in Xia, et al. [17], at corresponding strain rates, while the tensile strength was lower than the majority of the values in references 12-17. The maximum strain was lower than the values in Xia, et al. [17] and higher than in Amaniampong, et al. [15]. It is notable that the woven fabric had higher Young's modulus, tensile strength, maximum strain, and toughness than the single yarn. The mechanism of frictional contact between adjacent yarns was speculated to account for the added strength in the woven fabric case.

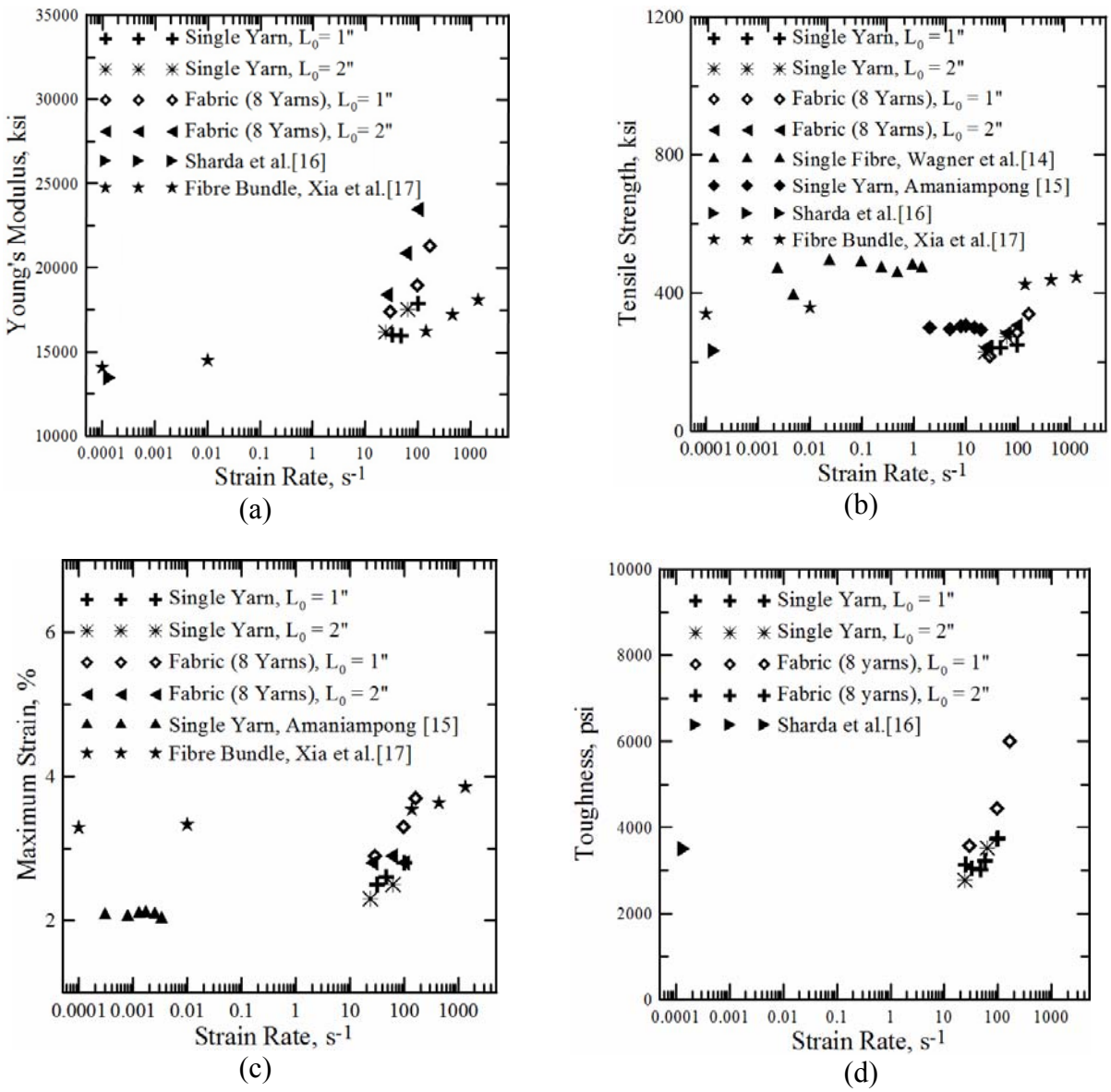

Figure 67. Comparison of Present Study With Literature Data: (a) Young's Modulus, (b) Tensile Strength, (c) Maximum Strain, and (d) Toughness

4. SINGLE-YARN PULLOUT TEST.

4.1 OVERVIEW.

Yarn slip in fabrics plays an important role in a variety of applications, especially in studying the impact of a projectile on woven ballistic armor, as described by Termonia, et al. [22], and in the forming of a fabric composite. Yarn slip also plays a key role in the concentration of yarn tensions near damaged regions in the fabric and in the propagation of damage, as described by Godfrey and Rossettos [23]. Early yarn pullout experiments include those of Sebastian, et al. [24], and Motamedi, et al. [25], who studied yarn pullout from plain-woven cotton fabrics. For these low-modulus fabrics, the yarn pullout response is largely governed by elastic deformations

in the pulled yarn and cross yarns. Martinez, et al. [26], studied the force required to completely pullout a single yarn from Kevlar fabrics held in place by static weights loaded over the full area of the fabric. They found that pullout force increased as fabric yarn count increased. Pan and Yoon [27] applied a modified Pan's theory to the yarn pullout process to reveal the effect of yarn interaction in fabrics, and showed the applications of this pullout technique in characterizing fabric mechanical behavior. Bazhenov [28] performed yarn pullout tests on aramid fabrics with various yarn counts and deniers. The experiments used a fabric-holding fixture that clamped the bottom edge of the fabric while leaving the transverse edges unconstrained. Bazhenov found that the maximum pullout force increased linearly with increasing sample length. The uncrimping portion of the curve was also observed to be linear with yarn displacement. Simons, et al. [3], devised an improved pullout test by clamping the fabric along its transverse edges. This design greatly simplifies the tests, as a series of pullout experiments can be performed without repositioning the grips at the edges of the fabric. Additionally, this arrangement allows for a variable transverse tension to be applied to the fabric, which may simulate the pullout process during a ballistic event more realistically. Experiments were performed on a wide range of fabric architectures and fiber types, including Kevlar 29, Spectra, and Zylon. The study found that the pullout forces strongly depend on the transverse preload and yarn count. Kirkwood, et al. [29], also conducted yarn pullout tests of Kevlar KM-2 fabric to study the mechanism of yarn pullout. The effects of fabric size, transverse tension, and multiple yarn pullout were investigated. Additionally, an empirical model was generated that replicates the pullout data to a high degree of accuracy. This model was used to correlate ballistic results with pullout damage in Kevlar fabric. King [30-32] employed a series of experimental studies of the tribological properties of Kevlar yarns and frictional resistance at different rates to gain a qualitative and quantitative understanding of the frictional forces that resist yarn slip.

During uncrimping, the yarn undergoing pullout progressively straightens and locally disturbs the nominal woven architecture [27]. This process progressively alters the visual appearance of the yarn as its uncrimped length increases and results in a nearly linear, force-displacement curve. When the uncrimping zone reaches the bottom edge of the specimen, the peak load point is reached. The entire yarn then begins to translate within the fabric, and the pullout force gradually decreases with displacement. The oscillations in the force-displacement curve during yarn translation correspond to the individual cross-yarns passed by the translating yarn. The pullout force typically approaches a value of zero as the total yarn displacement reaches a value equal to the sample length.

A series of single-yarn pullout tests of Kevlar 49 fabric were conducted at the Structures Laboratory at ASU to investigate the behavior of a single yarn during pullout. The following sections discuss the test setup, results, and simulation of single-yarn pullout behavior by using a close-form solution.

4.2 PULLOUT TEST.

4.2.1 Test Setup.

An MTS tensile test machine with two load cells with 50- and 300-lb capacities were used for yarn pullout tests. The 50-lb capacity load cell was used to measure pullout force, and the other was used to measure the preloaded transverse force. An edge-clamped, fabric-holding fixture was developed to serve as the bottom grip, and a manual grip was used to clamp the yarn undergoing pullout. The transverse tension was applied to the fabric through a sliding-edge clamp. By turning the screw nut on the threaded rod, different transverse tension forces can be applied to the fabric and be simultaneously measured by the 300-lb load cell. Clamping the fabric edges is accomplished through wrapping around a notch. The top and bottom edges of the fabric were unconstrained during the tests, as shown in figures 68 and 69.

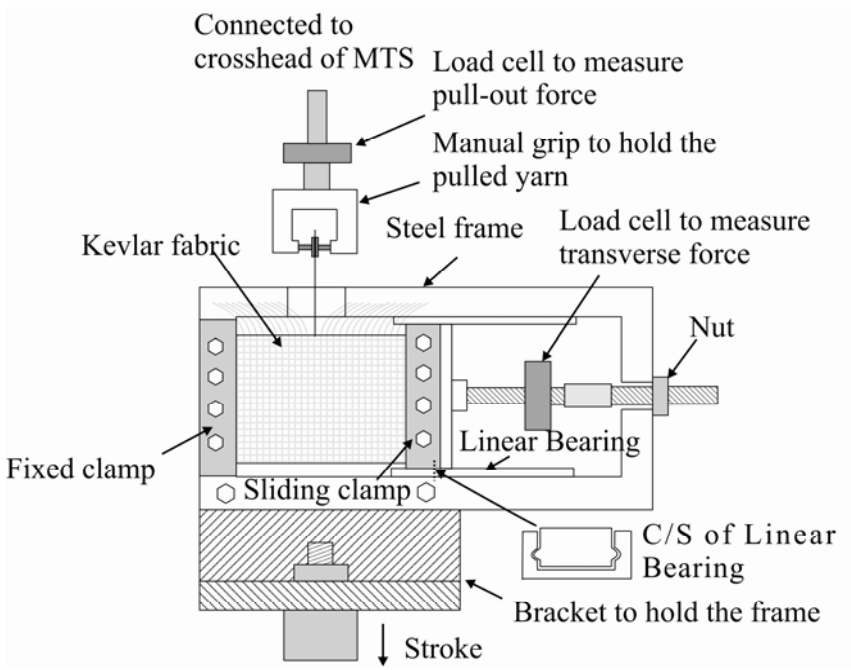

C/S = Cross-section

Figure 68. Experimental Setup of Yarn Pullout Tests

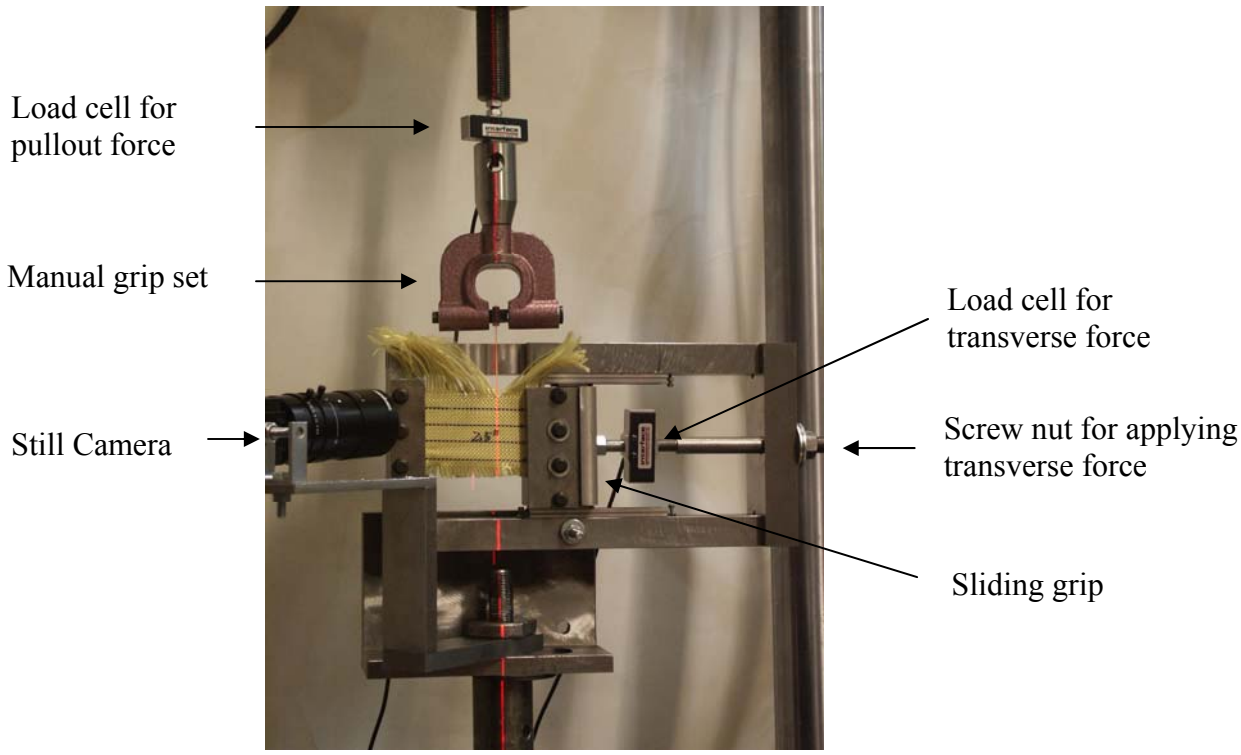

Figure 69. Photograph of Experimental Setup for Yarn Pullout Tests

Prior to the tests, transverse (fill) yarns were manually removed from the top edge of the fabric to expose 2.5″ of longitudinal (warp) yarns. The remaining part of the woven fabric was then clamped in the fixture. The 3.5″ fabric remained between the transverse grips after wrapping and clamping the transverse edges. The fabric length varied from 1.5″ to 3.5″. Using one Kevlar fabric clamped in the test fixture, five or six tests were conducted by choosing different individual yarns at different locations. For each test, the pulled yarn was aligned with a laser device to make sure that proper alignment could be achieved. All the tests were recorded by a still camera.

4.2.2 Description of Yarn Pullout.

"Yarn uncrimping" can be defined as the first stage of the yarn pullout process, corresponding to the part of the force-displacement curve up to the peak force point. The subsequent bulk motion of the yarn through the fabric can be referred to as "yarn translation," corresponding to the portion of the force-displacement curve past the peak force point. "Yarn pullout" is considered to comprise both of these processes because yarn translation cannot occur without first uncrimping the yarn [27]. Figure 70 shows the schematic of the yarn during a pullout test.

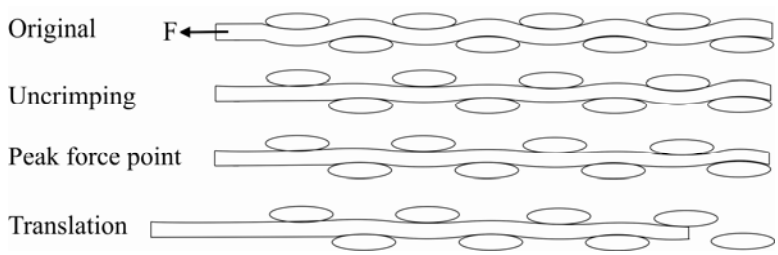

Figure 70. Yarn Behavior During Pullout

Figure 71 shows a representative single-yarn pullout force versus displacement curve. During uncrimping, the yarn undergoing pullout progressively straightens and locally disturbs the nominal woven architecture [29]. When the uncrimping zone reaches the bottom edge of the specimen, the peak load point is reached. The entire yarn then begins to translate within the fabric, and the pullout force gradually decreases with displacement. The oscillations in the force-displacement curve during yarn translation correspond to the individual cross-yarns passed by the translating yarn. The pullout force typically approaches a value of zero as the total yarn displacement reaches a value equal to the sample length. It should be noticed that the pre-applied transverse load is not constant during pullout. It reaches maximum value when the pullout force reaches the peak load, and then drops gradually with oscillations until the end of test. At the end, the transverse force is slightly lower than the initial preloaded value because when the yarn was totally pulled out, the fill yarns were allowed to straighten more and relax the preloaded transverse force. Figure 72 shows the same test results but with a different scale for transverse force. It clearly indicates the same phenomena discussed above. It also shows that the oscillations after peak load of both curves are in phase with each other and these two curves have the same amount of oscillations.

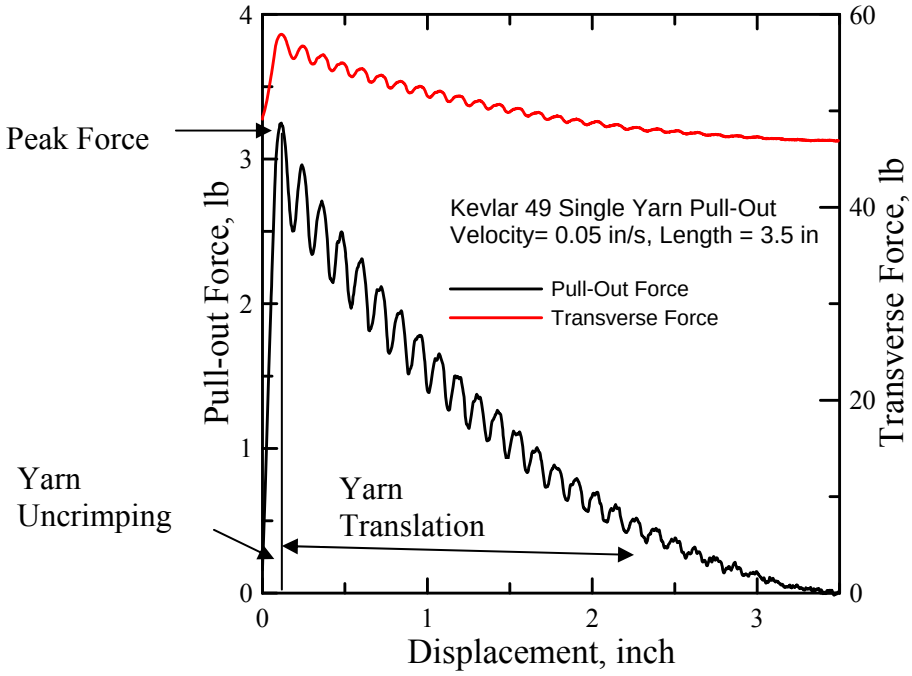

Figure 71. Representative Single-Yarn Pullout Force vs Displacement Curve

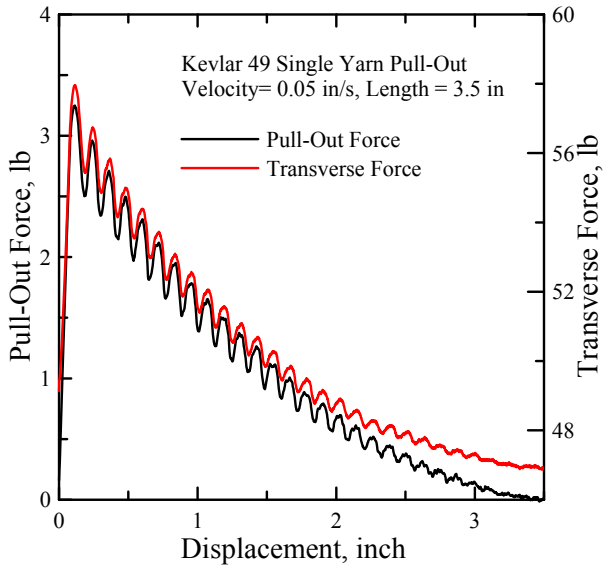

Figure 72. Comparison of Pullout Force With Transverse Force

A closer examination reveals that there are approximately 25 or 26 individual peaks representing yarn being pulled through approximately 57 or 58 fill yarns and the pullout force drops to zero, even though a small length of yarn is still embedded in the specimen. The post-peak pullout force drops more rapidly at the beginning and behaves nonlinearly. To be more quantitative, the peak value of each visible individual peak and corresponding displacement value were collected, as shown in figure 73. Figure 74 shows the difference between the displacement values of adjacent peaks. Clearly, the difference is quite close to a constant value. The average of the differences is 0.1186″, which is quite close to yarn period, and 0.1176″, which is equal to 2 divided by 17 (ply count is 17x17 per inch for the Kevlar 49 fabric tested).

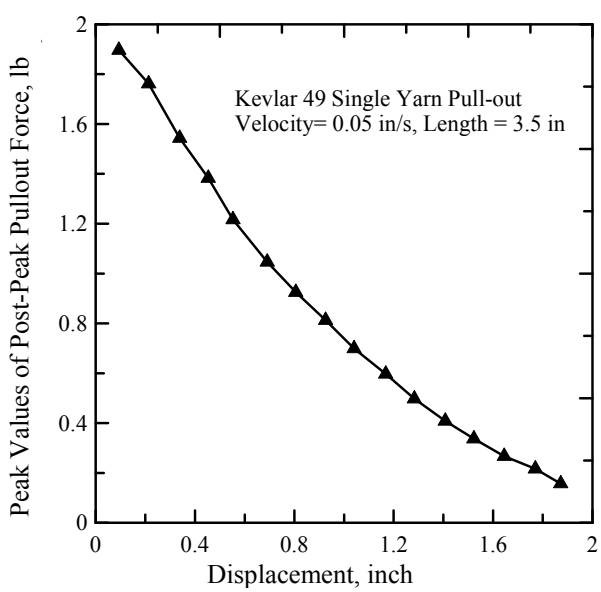

Figure 73. Peak Values of Post-Peak Pullout Force

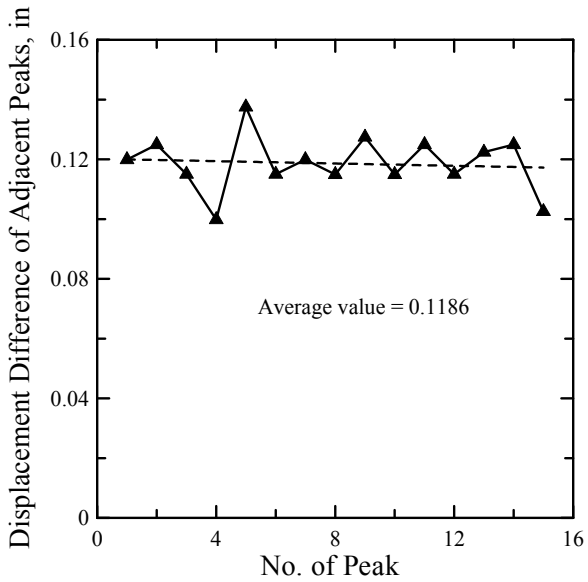

Figure 74. Displacement Differences of Adjacent Peaks

4.2.3 Test Results and Discussion.

This section lists typical test results of Kevlar 49 specimens with different pullout lengths. All the curves show similar behavior.

4.2.3.1 Typical Pullout Force Versus Displacement Curves.

Figures 75 through 77 show the pullout force and transverse force versus pullout length (displacement) of 2.0″, 2.5″, and 3.5″ specimens, respectively. These three tests were conducted with about 47-lb preloaded transverse force.

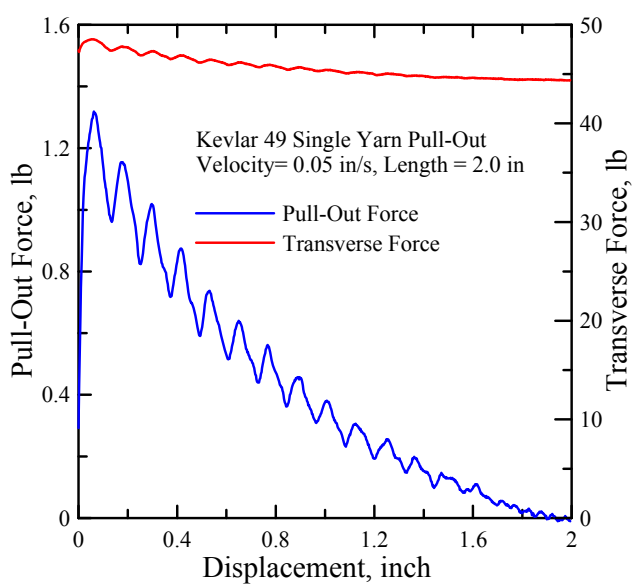

Figure 75. Pullout and Transverse Force vs Displacement Curves of a 2.0″ Specimen

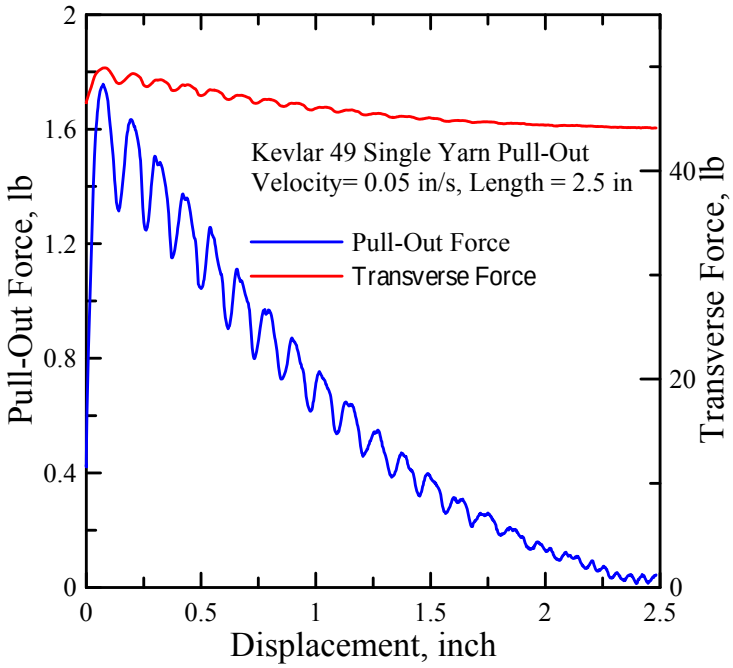

Figure 76. Pullout and Transverse Force vs Displacement Curves of a 2.5″ Specimen

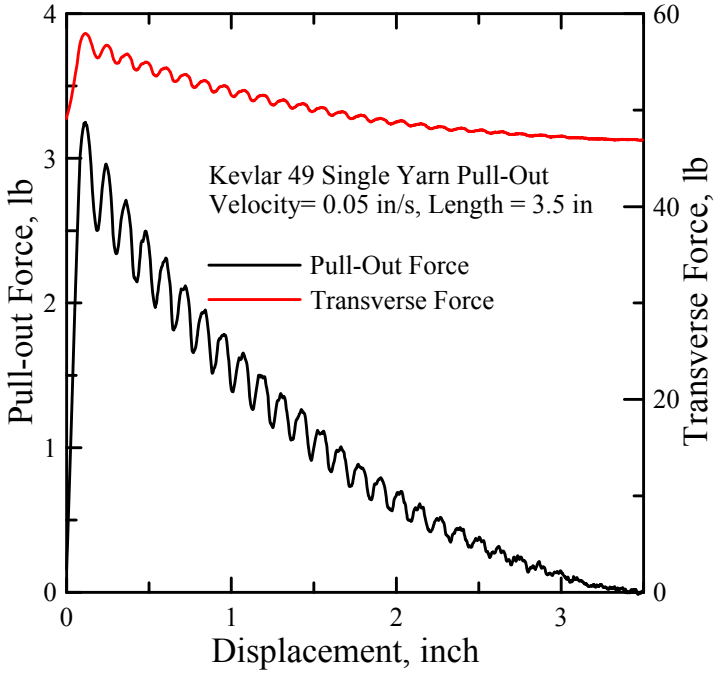

Figure 77. Pullout and Transverse Force vs Displacement Curves of a 3.5″ Specimen

4.2.3.2 Pullout Behavior of a 2.0″ Specimen.

Figure 78 shows the pullout force and transverse force versus displacement of a 2.0″ specimen with different transverse force (Ft) levels. The peak pullout force increases with increasing transverse force.

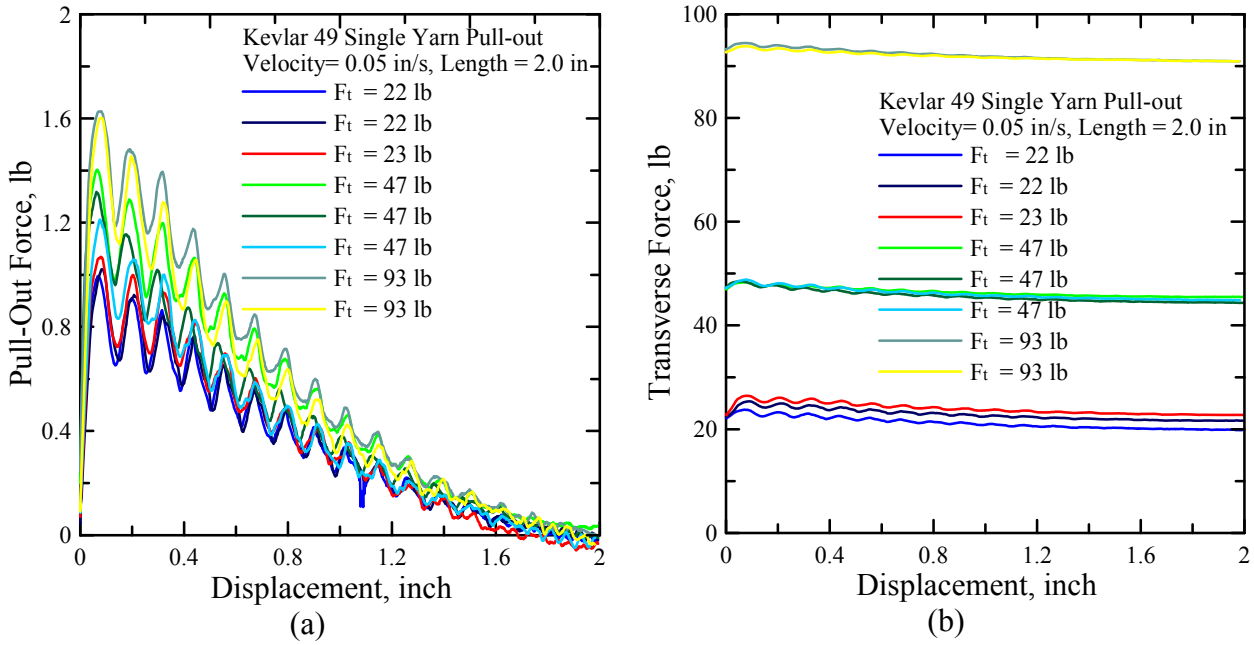

Figure 78. Behavior of a 2.0″ Specimen: (a) Pullout Force vs Displacement Curves and (b) Transverse Force vs Displacement Curves

4.2.3.3 Pullout Behavior of 2.5″ Specimen.

Figure 79 shows the pullout force and transverse force versus displacement of a 2.5″ specimen with different transverse force levels. The peak pullout force increases with increasing transverse force.

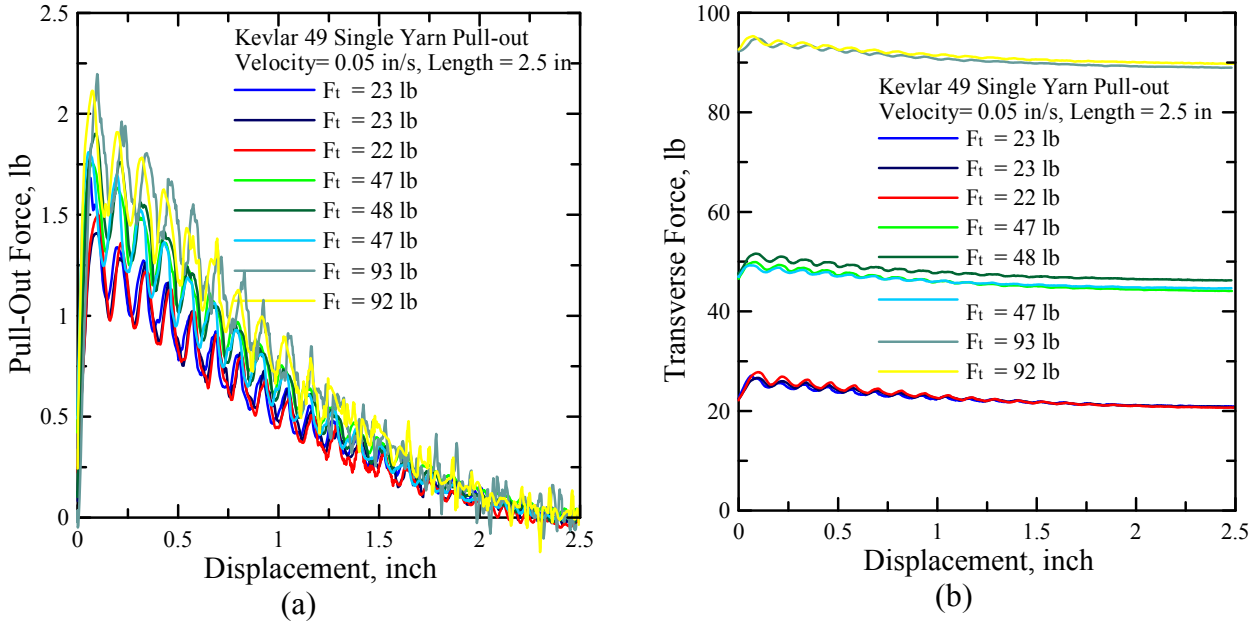

Figure 79. Behavior of a 2.5″ Specimen: (a) Pullout Force vs Displacement Curves and (b) Transverse Force vs Displacement Curves

4.2.3.4 Pullout Behavior of a 3.5″ Specimen.

Figure 80 shows the pullout force and transverse force versus displacement of a 3.5″ specimen with different transverse force levels. The peak pullout force increases with increasing transverse force.

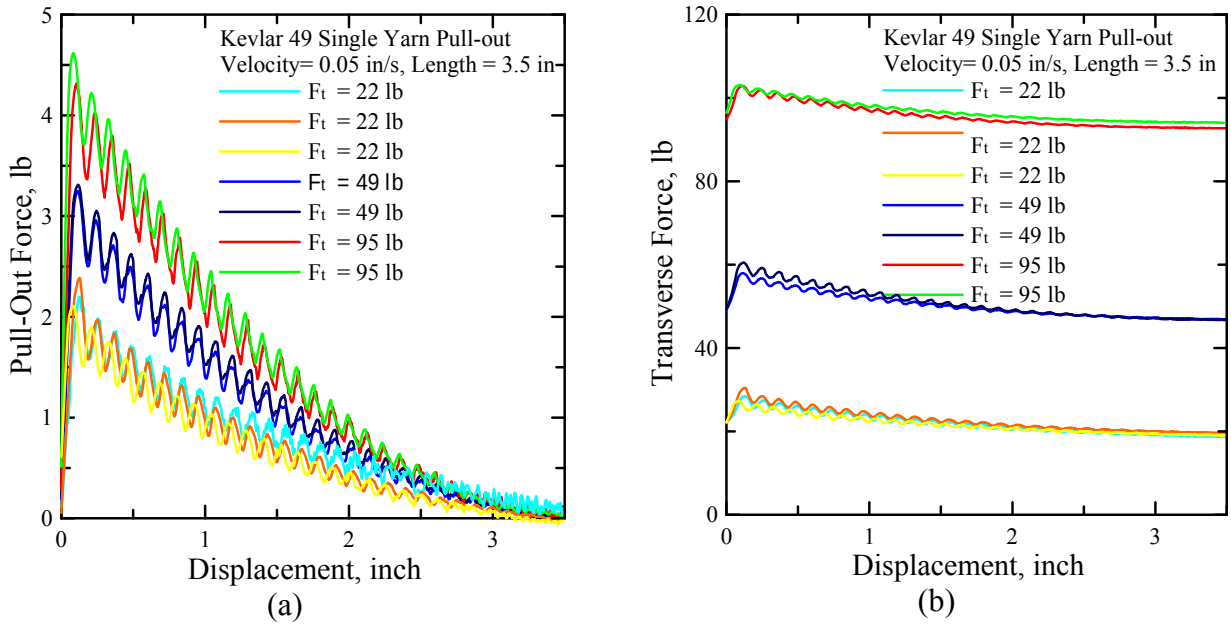

Figure 80. Behavior of a 3.5″ Specimen: (a) Pullout Force vs Displacement Curves and (b) Transverse Force vs Displacement Curves

4.2.3.5 Pullout Behavior With Different Transverse Loads.

To show the effect of specimen length, figures 81 to 83 indicate the pullout force versus displacement curves of three different specimen sizes with 27-, 52- and 97-lb peak transverse force, respectively. The peak transverse force in the plot is the average of all the peak transverse forces of each test category. The figures clearly show that the peak pullout force increases with increasing specimen length.

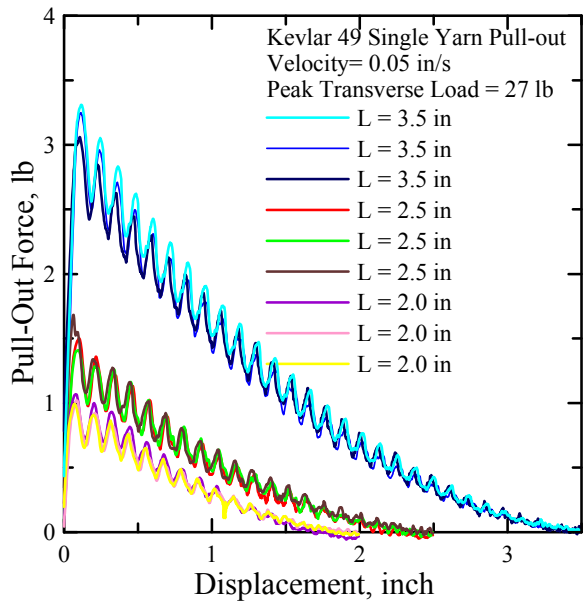

Figure 81. Pullout Force vs Displacement Curves With 27-lb Peak Transverse Force

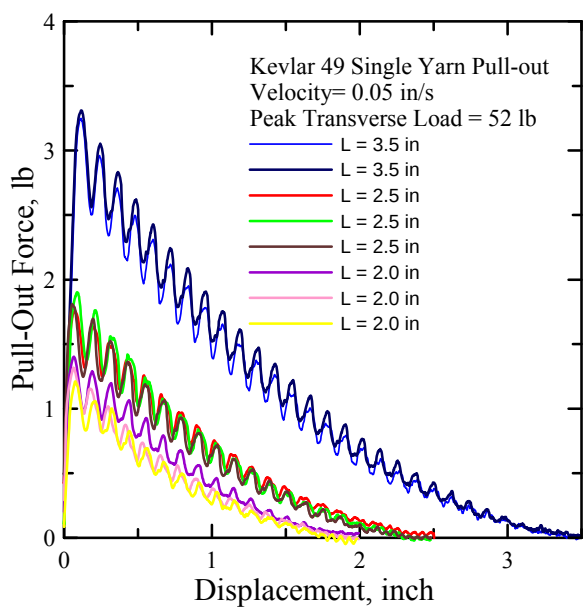

Figure 82. Pullout Force vs Displacement Curves With 52-lb Peak Transverse Force

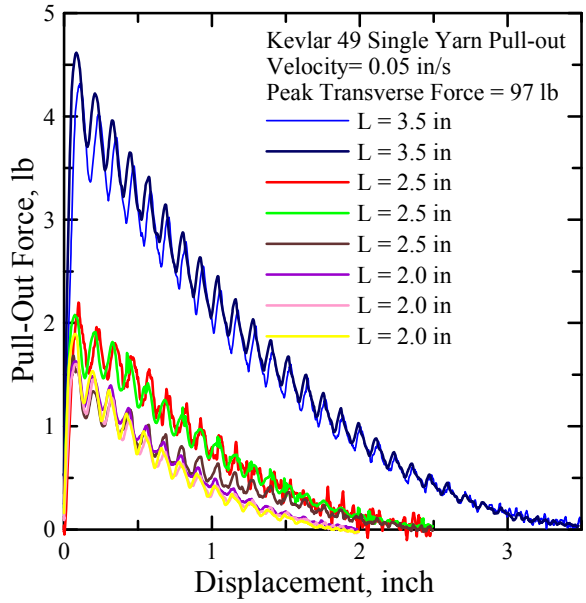

Figure 83. Pullout Force vs Displacement Curves With 97-lb Peak Transverse Force

4.2.3.6 Discussion of Peak Pullout Force.

Figure 84 indicates the relation between peak pullout force and specimen length at three different transverse force levels. The peak transverse force in the plot is the average of all the peak transverse forces of each test category. The peak pullout force increases linearly with increasing specimen length at each peak transverse force level.

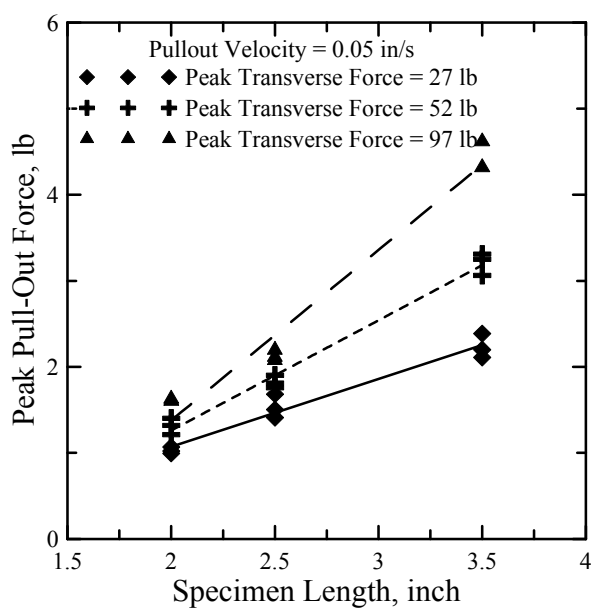

Figure 84. Peak Pullout Force vs Specimen Length

Figure 85 indicates the relation between peak pullout force and peak transverse force per yarn for three different specimen sizes. Peak pullout force increases linearly with increasing peak transverse force per yarn for each specimen length.

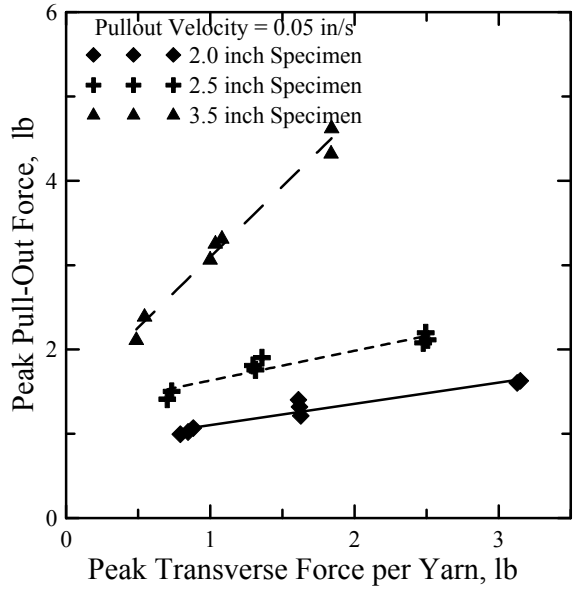

Figure 85. Peak Pullout Force vs Peak Transverse Force per Yarn

Figure 86 shows the relation between peak pullout force per unit length, normalizing the peak pullout force with respect to specimen length, and peak transverse force per yarn. The linear relation of peak pullout force per unit length and peak transverse force per yarn is still predominant.

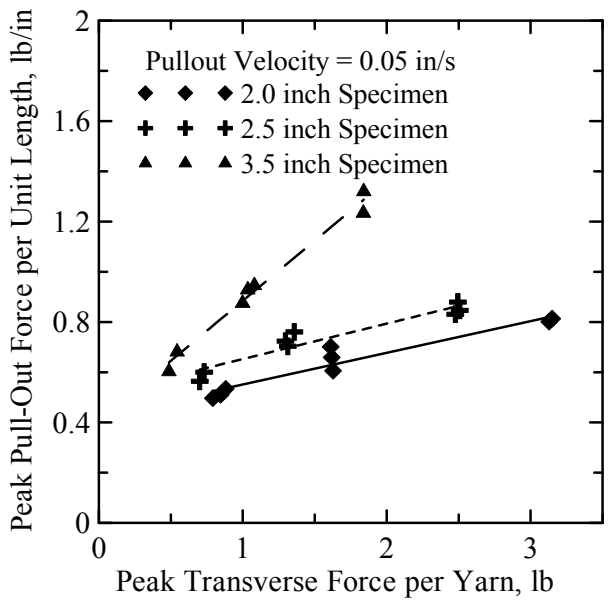

Figure 86. Peak Pullout Force per Unit Length vs Peak Transverse Force per Yarn

Figures 87 and 88 show the relations between the energy needed to pull the yarn out and specimen length and the energy needed to pull the yarn out per unit length and specimen length, respectively. The energy needed to pull the yarn out increases linearly with increasing specimen length at each transverse force. The energy needed to pull the yarn out per unit length versus specimen length also has the same phenomena.

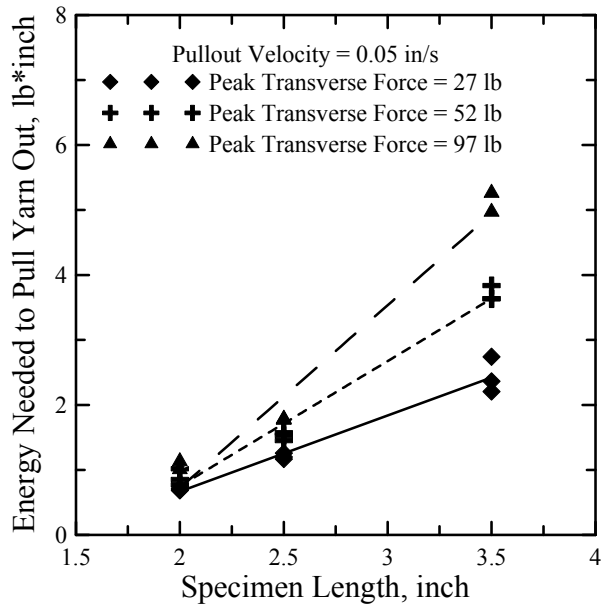

Figure 87. Energy Needed to Pull the Yarn Out vs Specimen Length

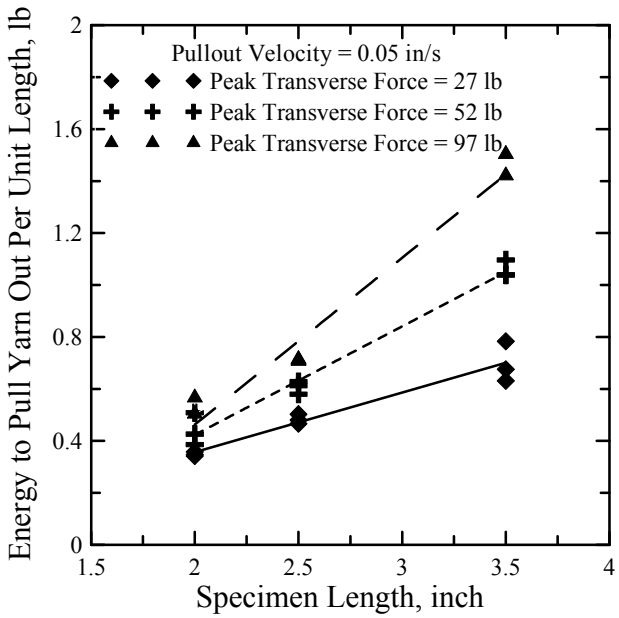

Figure 88. Energy Needed to Pull the Yarn Out per Unit Length vs Specimen Length

4.3 PULLOUT MODEL AND CURVE FITTING.

4.3.1 Analytical Model.

4.3.1.1 Mathematical Derivation.

A fabric pullout model was developed based on earlier work by Naaman, et al. [33 and 34], with changes to account for the boundary effects and the work by Sueki, et al. [35].

Figure 89 shows a typical simplified pullout-slip response obtained by pulling one yarn from the fabric. The characteristic of the curve can be divided into two zones based on various stages of shear stress distribution in the yarn. Initially, the curve shows a linear response corresponding to the uncrimping of the pulled yarn (stage I). When the load reaches the peak load, the yarn starts to translate (stage II). The mechanism of shear stress, force distribution, and derivations for each stage will be explained in the next section.

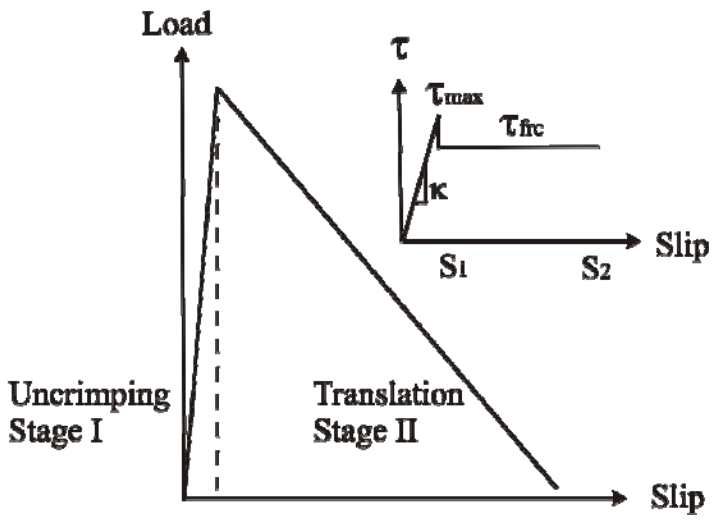

Figure 89. Pullout-Slip Response and Shear Strength Diagram

4.3.1.2 Basic Equations.

This section discusses the basic equations of the model developed to simulate the behavior of yarn pullout from fabric. The model is based on the assumption that the fabric is a continuum matrix, except the pulled yarn. The yarn interface and matrix are defined by the shear strength properties diagram (figure 89).

Static equilibrium requires that along the embedded length of the yarn in the matrix, the tensile forces in the longitudinal yarn (F^L) be transferred to the adjacent transverse yarns (F^T) through the interface and reacted against the restraint plate by normal compressive matrix stresses. This relationship expressed in the differential form is

$$\frac{dF^L}{dx} = -\frac{dF^T}{dx} = \psi\tau \tag{17}$$

where ψ is the equivalent circumference of the yarn and τ is the shear stress at the yarn-matrix interface. For small loads, the local shear stress behaves linear elastic as a function of slip with slope κ defined from the shear strength diagram (figure 89), and the slip S is defined by the difference of the elongation of the yarn δ_L and its adjacent neighbors δ_T

$$\tau = \kappa S = \kappa\left(\delta_L - \delta_T\right) = \kappa\int_0^x \left[\varepsilon_L(x) - \varepsilon_T(x)\right]dx \tag{18}$$

where $\varepsilon_L = \dfrac{F}{A_y E_y}$, $\varepsilon_T = -\dfrac{F}{K^T}$, A is the cross-section area, E is Young's modulus, and the subscripts y and T refer to longitudinal and transverse yarns, respectively. K^T refers to the frictional shear stiffness of a yarn placed in the transverse direction to the pullout. Substituting equation 18 in 17 and taking the derivative with respect to x yields the differential equation for the yarn pullout force

$$\frac{d^2F}{dx^2} - \beta^2 F = 0 \tag{19}$$

where $\beta^2 = \psi\kappa Q$ and $Q = \dfrac{1}{A_y E_y} + \dfrac{1}{K^T}$. The general solution of the second differential equation has the following form.

$$F(x) = C_1 e^{\beta x} + C_2 e^{-\beta x} \tag{20}$$

The axial force distribution is obtained by applying the force boundary conditions $F(0) = 0$ and $F(L) = P$ in equation 20 and by taking a derivative with respect to x, shear stress distribution is obtained.

$$F(x) = P\frac{\sinh(\beta x)}{\sinh(\beta L)} \tag{21}$$

$$\tau(x) = \frac{P\beta}{\psi}\frac{\cosh(\beta x)}{\sinh(\beta L)} \tag{22}$$

4.3.1.2.1 Pullout Response in Uncrimping Stage I.

Loading beyond the elastic limit is initiated when the shear stress exceeds the maximum shear strength $\tau_{max.}$ This leads to uncrimping for a length of d on the right-hand side of figure 90(a) while the pulled yarn is still in the original configuration on the left portion *(L-d)*. The shear stress distribution is governed by a constant frictional stress τ_{frc} along the uncrimping zone in addition to the maximum strength value τ_{max} at the uncrimping and crimping junction. The algorithm for the modeling is based on incrementally increasing the uncrimping length and calculating the applied force from the shear stress distribution. The resistant to pullout load P_1 is

calculated by the summation of the two forces: the crimping-resistant force $P_{1b,\max}$ and the uncrimping-resistant force P_d.

$$P_1 = P_d + P_{1b,\max} = \tau_{frc}\psi d + \frac{\tau_{\max}\psi}{\beta}\tanh(\beta(L-d)) \tag{23}$$

where $P_{1b,\max} = \frac{\tau_{\max}\psi}{\beta}\tanh(\beta(L-d))$. The force boundary conditions for the nonlinear stage are slightly modified ($F(0)=0$, $F(L-d)=P_{1b,\max}$, and $F(L)=P_1$) according to the crimping and uncrimping zones. Applying these boundary conditions in equation 20, force distributions in the crimping and uncrimping zones can be obtained.

$$\begin{aligned} F_b(x) &= P_{1b,\max}\frac{\sinh(\beta x)}{\sinh(\beta(L-d))}, && 0 \le x \le L\text{-}d \\ F_d(x) &= P_{1b,\max} + \tau_{frc}\psi\left(x-L+d\right), && L\text{-}d \le x \le L \end{aligned} \tag{24}$$

Slip at the end of the yarn is obtained for the crimping and uncrimping zones.

$$\begin{aligned} S(L)_1 &= \int_0^{L-d}\left[\frac{F_b(x)}{A_yE_y}+\frac{F_b(x)}{A_mE_m}\right]dx + \int_{L-d}^{L}\left[\frac{F_d(x)}{A_yE_y}+\frac{F_d(x)}{A_mE_m}\right]dx \\ &= \frac{P_{1b,\max}Q}{\beta}\frac{\left[\cosh(\beta(L-d))-1\right]}{\sinh(\beta(L-d))} + \frac{1}{2}Qd\left(\tau_{frc}\psi d + 2P_{1b,\max}\right) \end{aligned} \tag{25}$$

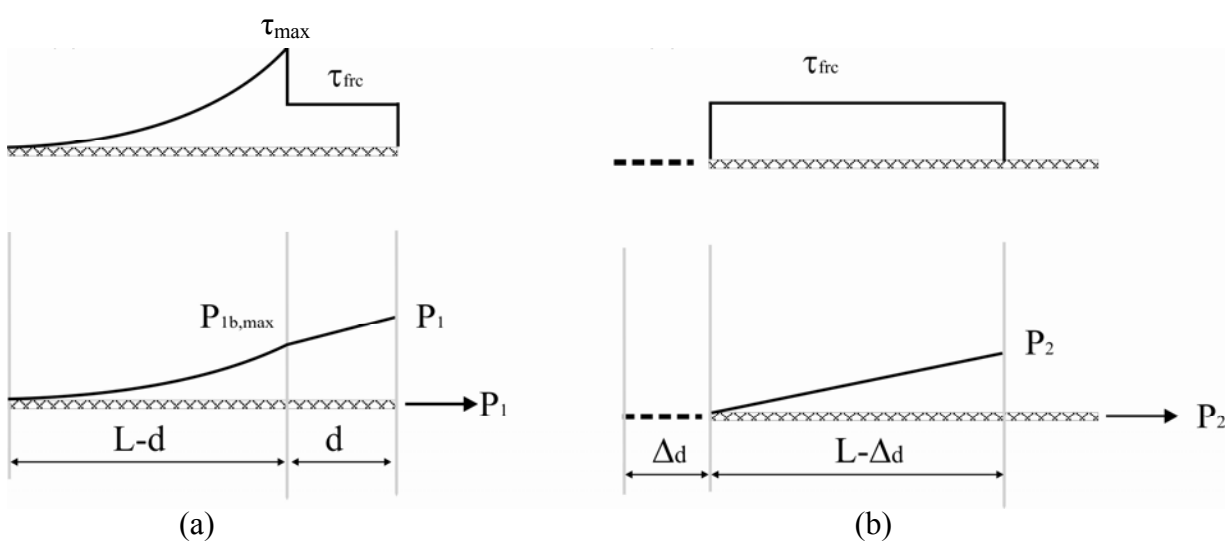

Figure 90. Shear Stress and Force Distribution Along Yarn for (a) Stage I (Uncrimping Stage) and (b) Stage II (Translation Stage)

4.3.1.2.2 Pullout Response in Translation Stage II.

Stage II is defined as translation response (figure 90(b)). It is assumed that at the time the yarn is completely uncrimped and starts to translate ($\Delta_d \geq 0$), the shear resistance still remains τ_{frc}.

It can be shown that during the this stage ($\Delta_d \geq 0$), the embedded length reduces to (L-Δ_d) and the dynamic pullout force at the end is

$$P_2 = \tau_{frc}\psi(L - \Delta_d) \tag{26}$$

From figure 90(b) and static equilibrium, force distribution can be written as

$$F(x) = P_2 + \tau_{frc}\psi(x - \mathrm{L} + \Delta_d) = \tau_{frc}\psi x, \quad 0 \leq \mathrm{x} \leq \mathrm{L}\text{-}\Delta_d \tag{27}$$

The slip at the end of the yarn is also calculated in the same way as equation 24.

$$S(L)_2 = \int_0^{L-\Delta_d} \left[\frac{F(x)}{A_f E_f} + \frac{F(x)}{A_m E_m} \right] dx = \frac{\tau_{frc}\psi Q}{2}(L - \Delta_d)^2 \tag{28}$$

The total slip at the end of the yarn measured in the translation stage, comes from the slip at the end of stage I $S(L)$ and the translation in stage II:

$$S_{total}(L)_2 = S(L)_1 + S(L)_2 \tag{29}$$

It should be noted that the measured sliding displacement in stage II $D_{measured}(L)$ from experiment consists of the total slip given by equation 30 and the rigid-body displacement Δ_d

$$D_{measured}(L)_2 = S(L)_1 + S(L)_2 + \Delta_d \tag{30}$$

4.3.1.3 Algorithms for Pullout Simulations.

The pullout response obtained from experiment can be simulated using the analytical model described in the preceding section. The simulation procedure can be summarized as follows:

- In uncrimping stage I, incrementally impose the uncrimping length d and calculate the corresponding load P_1 and slip $S(L)_1$ from equations 23 and 25. It is assumed that stage I ends and the translation mode begins when the computed slip $S(L)_1$ starts to decrease.

- In translation stage II, the load and total slip P_2 and $S(L)_2$ are calculated by equations 26 and 28 and the measured sliding displacement, which includes rigid-body displacement, is defined by equation 30 in simulation.

4.3.1.4 Contact Between Pulled and Fill Yarns.

The contact area between the pulled and fill yarns is not constant during pullout. This assumes the contact area at each cross-over joint is half the circumference of the warp yarn for unit length when the pulled yarn is stationary, which is A_1, shown in figure 91. As the yarn is displaced, the existed undulation becomes out of phase with the undulation imposed by the weave. When the phase shift reaches the point where the imposed undulation is exactly opposed to the set undulation (i.e., after the slipping yarn has slipped a distance equal to the spacing of the fill yarns), the contact area is minimum, A_2, as shown in figure 91.

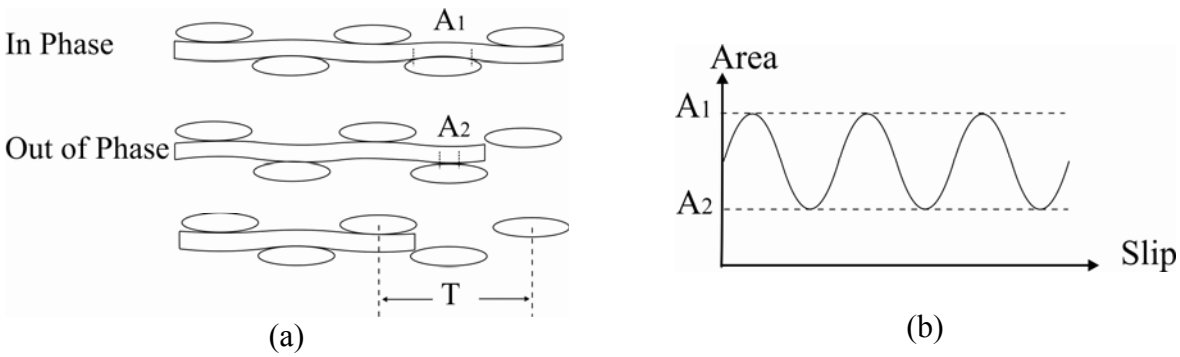

Figure 91. Contact Area During Yarn Translation: (a) Contact Area at Different Stages and (b) Sinusoidal Function Describing the Contact Area Change During Pullout With Maximum Value A_1 and Minimum Value A_2

Figure 92 shows the geometry of Kevlar fabric with the cutting plane along the warp direction. Using an image analysis method, the cross-section of warp yarn can be approximated by an ellipse with a semi-major axis of 0.0258″ and a semi-minor axis of 0.00334″, as shown in figure 93.

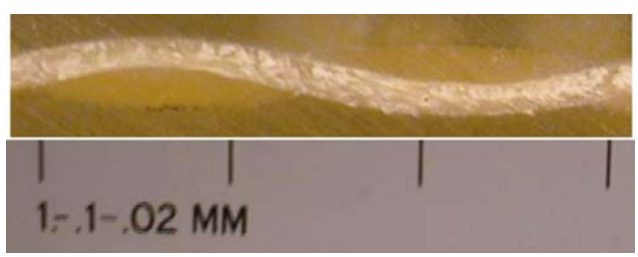

Figure 92. Cross-Section of Kevlar Fabric

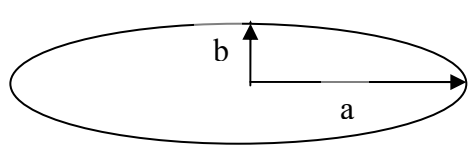

Figure 93. Cross-Section of Warp Yarn

The circumference of the warp yarn is calculated by

$$C \approx \pi\left[3(a+b)-\sqrt{(3a+b)(a+3b)}\right] \tag{31}$$

The area of the cross-section of warp yarn is calculated by

$$A = \pi ab \tag{32}$$

where a is the semi-major axis and b is the semi-minor axis of the ellipse.

As the contact area changes from C_1 to C_2 during pullout, it follows a sinusoidal function with a constant period, which is the difference of displacements of adjacent peaks of the force-displacement curve. To simulate the oscillation behavior after peak load, the effective contact area C_{ef} at stage II (translation) is defined as

$$C_{ef} = \frac{C}{2} + C_0\left[\sin(\frac{2\pi}{T}S)-1\right] \tag{33}$$

where C is circumference of the warp yarn, C_0 is the amplitude of sinusoidal function, T is the period of oscillation (T = 0.1176 inch), and S is the slip distance. The value of C_{ef} is between C_1 and C_2, $C_{ef} \in \left[\frac{C}{2}, \frac{C}{2} - 2C_0\right]$.

Table 24 lists the geometry parameters used for the model.

Table 24. Geometry Parameter for Simulation

Semi-Major Axis, a (in.)	Semi-Minor Axis, b (in.)	Cross-Section Area, A (in^2)	Perimeter, C (in.)	Effective Diameter, ϕ (in.)
0.0258	0.00334	2.7 (10^{-4})	0.1057	0.0168

4.3.2 Pullout Curve Fitting.

Figures 94 to 96 show the shear stress of interface versus slip (pullout length) for different specimen lengths at three different peak transverse force levels. Each curve represents one typical test. The maximum shear stress (τ_{max}) and friction shear stress (τ_{frc}) slightly increase with increasing specimen length. Maximum shear stress (τ_{max}) increases from 9.8 to 14 psi and friction shear stress (τ_{frc}) increases from 7.5 to 9.5 psi when the peak transverse force is approximately 27 lb. When the peak transverse force is approximately 52 lb, τ_{max} and τ_{frc} of the 2.0″ and 2.5″ specimens are almost identical; but for the 3.5″ specimen, they increase from 14 to 19 psi and from 11 to 14 psi, respectively. Similarly when the peak transverse force is approximately 97 lb, τ_{max} and τ_{frc} are almost the same for the 2.0″ and 2.5″ specimens, and for the 3.5″ specimen, they increase from 17 to 25 psi and from 13 to 19 psi, respectively.

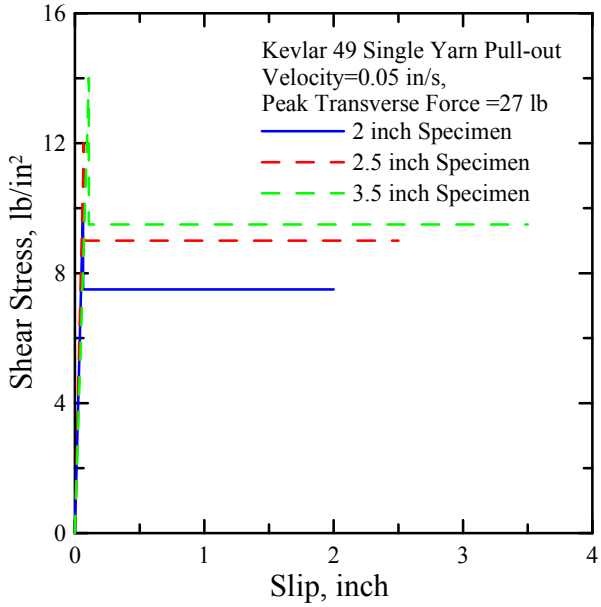

Figure 94. Shear Stress vs Slip at 27-lb Peak Transverse Force for Different Specimen Lengths

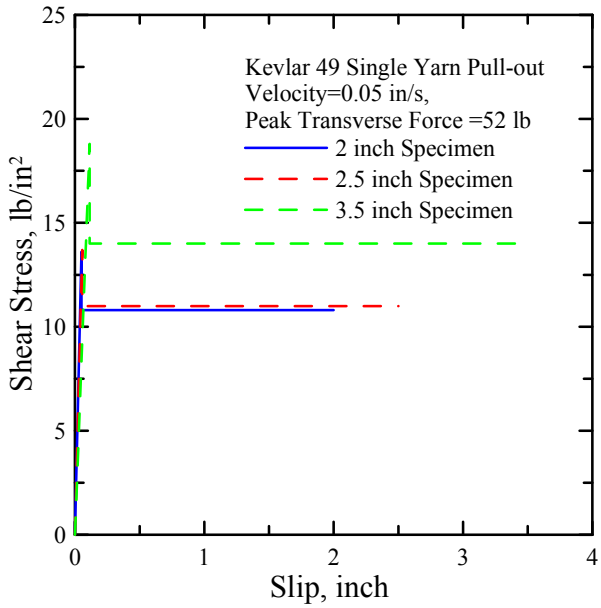

Figure 95. Shear Stress vs Slip at 52-lb Peak Transverse Force for Different Specimen Lengths

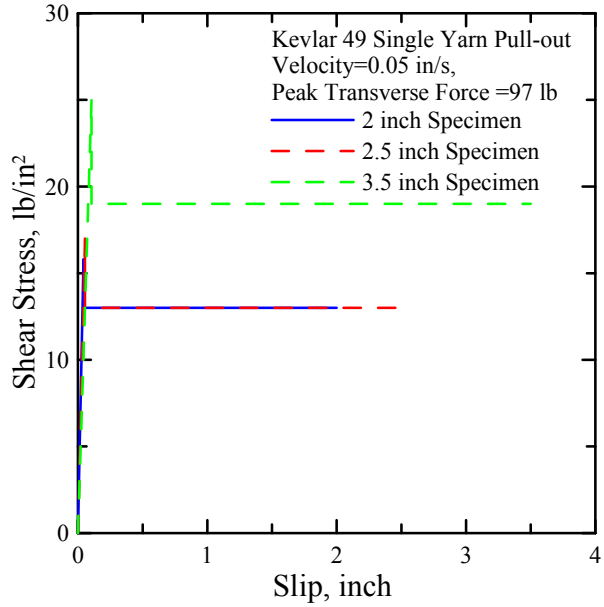

Figure 96. Shear Stress vs Slip at 97-lb Peak Transverse Force for Different Specimen Lengths

Figures 97 to 99 indicate the shear stress versus slip of 2.0″, 2.5″, and 3.5″ specimens at different preloaded transverse forces. Each figure shows three typical curves of shear stress distribution at three transverse force levels. These curves clearly show that both maximum shear stress and friction shear stress increase with increasing transverse force.

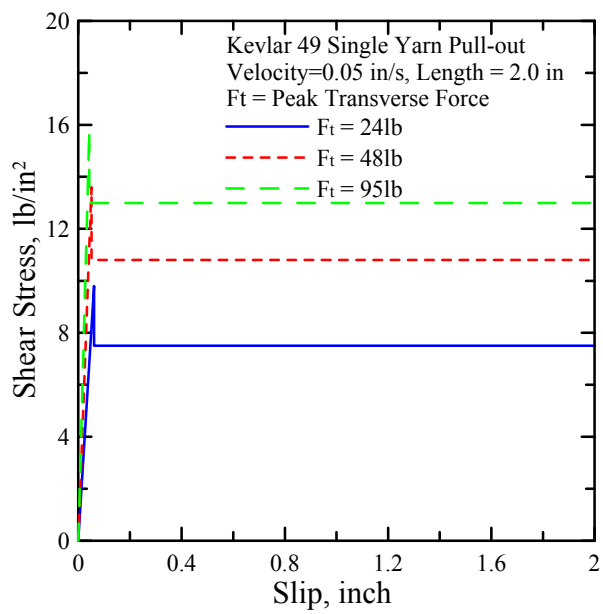

Figure 97. Shear Stress vs Slip of 2.0″ Specimens at Different Transverse Forces

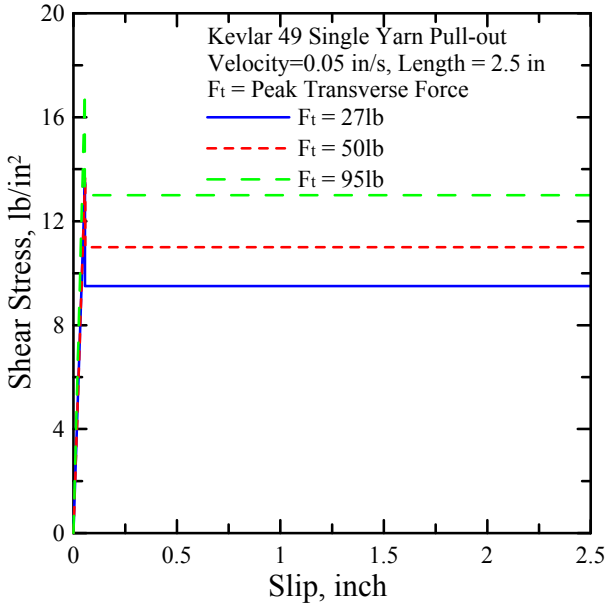

Figure 98. Shear Stress vs Slip of 2.5″ Specimens at Different Transverse Forces

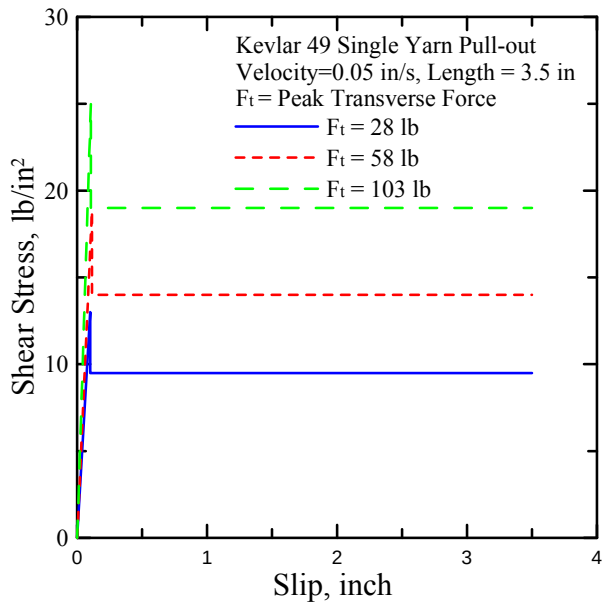

Figure 99. Shear Stress vs Slip of 3.5″ Specimens at Different Transverse Forces

Figures 100 and 101 clearly show the effect of specimen length on the maximum shear stress and friction shear stress at different transverse forces. Both maximum shear stress and friction shear stress slightly increase with specimen length. It also shows that they increase with increasing peak transverse force.

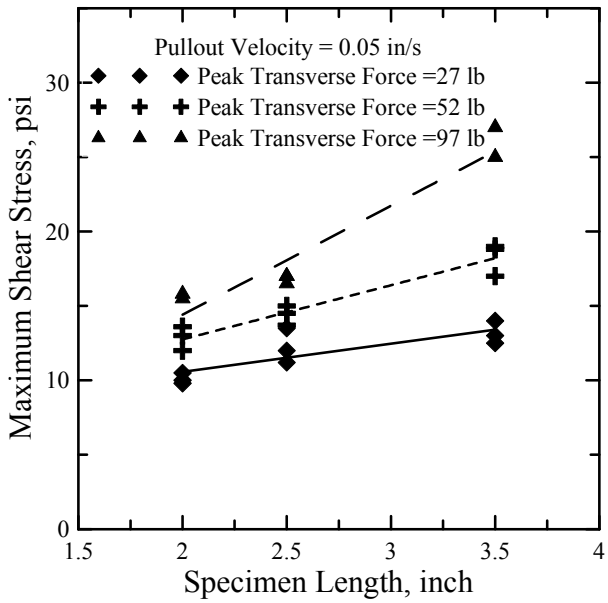

Figure 100. Maximum Shear Stress vs Specimen Length at Different Transverse Forces

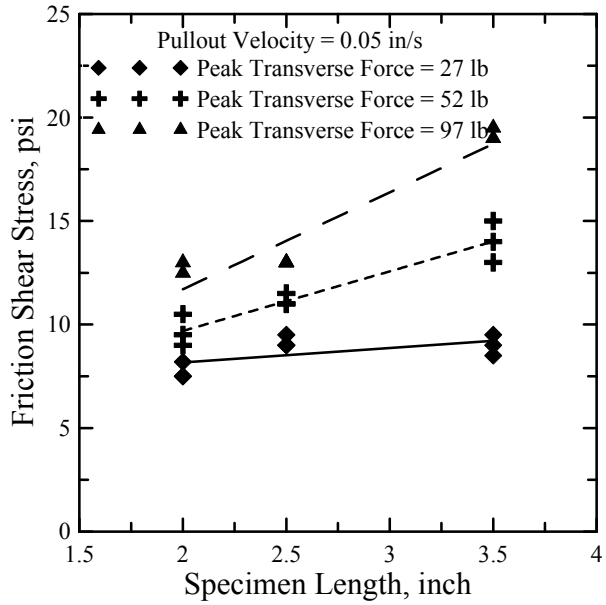

Figure 101. Friction Shear Stress vs Specimen Length at Different Transverse Forces

Figures 102 to 104 show the test data compared to simulation results for one typical test of 2.0″, 2.5″, and 3.5″ long specimens, respectively. The simulation matched the test data well, except the post-peak portion drops linearly and the test data drops nonlinearly. This happened because the friction shear stress was assumed to be constant in the model.

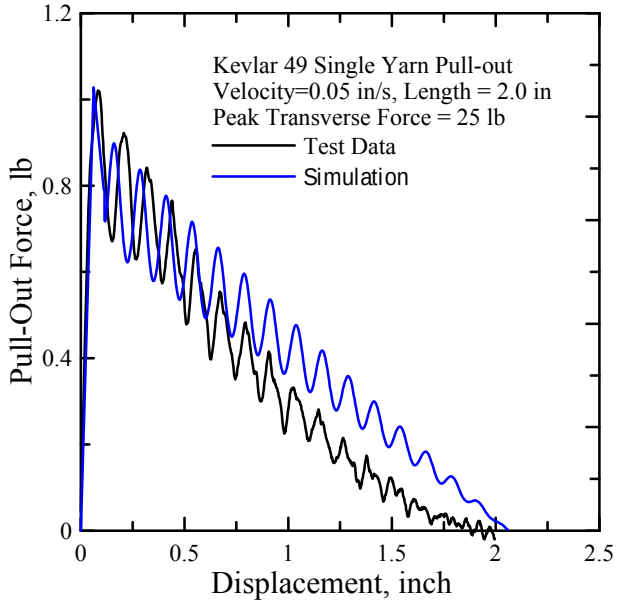

Figure 102. Comparison of Test Data and Simulation for a 2.0″ Specimen

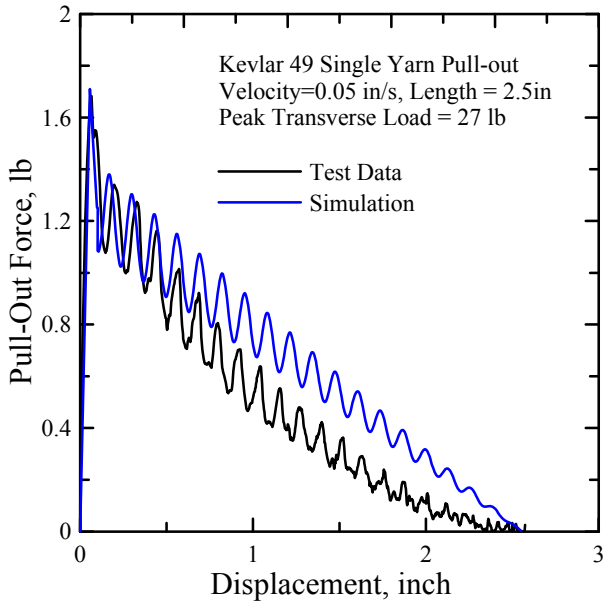

Figure 103. Comparison of Test Data and Simulation for a 2.5″ Specimen

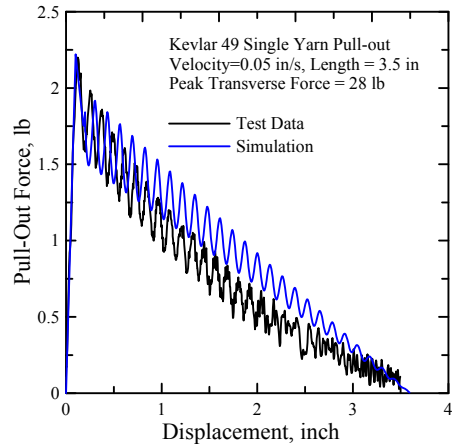

Figure 104. Comparison of Test Data and Simulation for a 3.5″ Specimen

Nominal shear stress τ_{nom} is defined as

$$\tau_{nom} = \frac{F_{\max}}{\pi \phi L} \tag{34}$$

where F_{max} is the maximum pullout force, ϕ is the effective diameter of a single yarn, and L is the total pullout length of a single yarn.

Figure 105 indicates the correlation between maximum shear stress ($\tau_{\max}$), friction shear stress (τ_{frc}), and nominal shear stress (τ_{nom}). Nominal shear stress lies between $\tau_{\max}$ and τ_{frc} as expected because it is the average stress value at maximum pullout force. Note that as the nominal shear stress increases, both the maximum and frictional shear stresses increase as well.

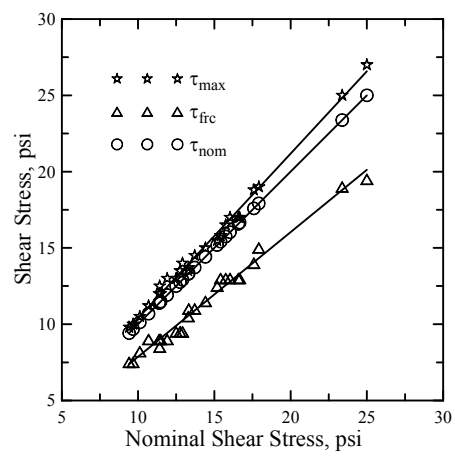

Figure 105. Correlation of Shear Stress and Nominal Shear Stress

All the tests and simulation results are listed in table 25, including the specimen length, number of yarns, pullout rate, peak pullout force, transverse force, nominal shear strength, and maximum shear stress.

Table 25. Single-Yarn Pullout Test and Simulation Results

Test No.	Specimen Length (in.)	Number of Yarns	Pullout Rate (in/s)	Transverse Load (lb)				Peak Pullout Force (lb)	Stroke at Peak Force (in.)	Energy Needed to Pull Yarn Out (lb*inch)	τ_{nom} (psi)	τ_{max} (psi)	τ_{frc} (psi)
				Initial	Maximum	Final	Average						
1	2.0	30	0.05	22.2	23.8	20.0	22.0	0.99	0.067	0.68	9.4	9.8	7.5
2	2.0	30	0.05	22.4	25.4	21.6	23.1	1.02	0.082	0.69	9.7	10.0	7.5
3	2.0	30	0.05	22.9	26.4	22.6	24.0	1.07	0.080	0.72	10.1	10.5	8.2
4	2.0	30	0.05	47.0	48.3	45.4	46.9	1.40	0.064	1.02	13.3	13.6	10.8
5	2.0	30	0.05	47.4	48.5	44.6	46.8	1.32	0.063	0.85	12.5	13.0	9.5
6	2.0	30	0.05	47.3	48.8	44.8	47.0	1.21	0.076	0.77	11.5	11.8	9.0
7	2.0	30	0.05	93.3	94.5	90.8	92.8	1.63	0.080	1.13	15.4	15.8	13.0
8	2.0	30	0.05	92.7	93.9	90.9	92.5	1.60	0.081	1.01	15.2	15.5	12.5
10	2.5	38	0.05	22.5	27.1	21.4	23.6	1.68	0.063	1.26	12.8	13.5	9.5
11	2.5	38	0.05	22.4	26.6	20.9	23.3	1.41	0.095	1.20	10.7	11.2	9.0
12	2.5	38	0.05	22.2	27.8	20.6	23.5	1.50	0.103	1.17	11.4	12.0	9.0
13	2.5	38	0.05	46.6	49.9	44.2	46.9	1.76	0.074	1.57	13.3	13.7	11.0
14	2.5	38	0.05	47.7	51.6	46.1	48.5	1.90	0.089	1.53	14.4	15.0	11.5
15	2.5	38	0.05	47.0	49.3	44.5	46.9	1.81	0.054	1.45	13.7	14.5	11.0
17	2.5	38	0.05	92.3	94.8	88.9	92.0	2.20	0.098	1.77	16.7	17.0	13.0
18	2.5	38	0.05	92.6	95.3	89.9	92.6	2.12	0.072	1.78	16.0	17.0	13.0
19	2.5	38	0.05	91.6	94.1	89.6	91.8	2.08	0.072	1.79	15.7	16.5	13.0
20	3.5	56	0.05	22.2	28.4	18.4	23.0	2.20	0.122	2.74	11.9	13.0	9.5
21	3.5	56	0.05	22.0	30.5	20.1	24.2	2.39	0.130	2.36	12.9	14.0	9.5
22	3.5	56	0.05	22.3	27.3	18.7	22.8	2.11	0.082	2.21	11.4	12.5	8.5
23	3.5	56	0.05	47.8	55.9	42.4	48.7	3.06	0.105	3.63	16.6	17.0	13.0
24	3.5	56	0.05	49.1	58.0	46.8	51.3	3.25	0.115	3.64	17.6	18.8	14.0
25	3.5	56	0.05	49.4	60.5	46.6	52.2	3.31	0.115	3.84	17.9	19.0	15.0
27	3.5	56	0.05	95.0	102.9	92.7	96.9	4.32	0.105	4.97	23.4	25.0	19.0
28	3.5	56	0.05	96.5	103.1	93.8	97.8	4.62	0.084	5.26	25.0	27.0	19.5

Note: 1. The peak transverse force per yarn is the value of maximum transverse force divided by the number of yarns.
2. The energy needed to pull the yarn out is the area of pullout force versus displacement (pullout length) curve.

5. CONCLUSIONS AND RECOMMENDATIONS.

A methodology to build a micromechanical model of Kevlar® fabric was developed. This methodology is general enough to be used for other fabric materials. This essentially starts with approximating the Kevlar weave geometry using simple geometric shapes like ellipse and sinusoidal curves. Optical microscopy was used to take images of sectioned fabric potted in epoxy. A program in MATLAB® was developed that can be used to digitize these images and provide estimates of the parameters associated with geometric functions. An experimental procedure to perform single-yarn tensile tests was developed, and experiments were performed with gage lengths (G.L.) varying from 2″ to 17″. The Weibull analysis of this data clearly indicated the effect of G.L. on the Kevlar yarn properties.

The mechanical properties of Kevlar 49 fabric and single yarn were investigated by conducting several sets of experiments, i.e., high strain rate tests of swath and single yarn and single-yarn pullout tests. A high strain rate test system was developed, including an MTS high-rate loading frame, signal conditioner and controllers, a laser extensometer, a high-speed digital camera, and a high-speed data acquisition system. A test procedure and data analysis method was proposed for the high strain rate tests. This type of test equipment and method are limited in strain rate to about 200 s^{-1}. The accuracy of the strain measurement was validated by comparing the strain values with the results obtained by image analysis. Kevlar® 49 fabric of two G.L.s (1″ and 2″) was tested at strain rates ranging from 25 to 170 s^{-1}. The dynamic material properties, i.e., Young's modulus, tensile strength, maximum strain, and toughness, were found to be dependent on strain rate within the range of the strain rates investigated. The maximum strain from the stroke measurement agreed well with that from the image analysis. Kevlar 49 single-yarn specimens of two G.L.s (1″ and 2″) were tested at strain rates ranging from 20 to 100 s^{-1}. The dynamic material properties of Kevlar 49 single-yarn specimens of both sizes were found to be sensitive to strain rates ranging from 20 to 100 s^{-1}. For both specimens, Young's modulus, tensile strength, maximum strain, and toughness increased when the strain rate increased.

A series of single-yarn pullout tests of Kevlar 49 fabric was conducted for three specimen lengths (2″, 2.5″, and 3.5″) at three levels of pre-applied transverse force of approximately 22, 47, and 94 lb. The peak pullout force and energy needed to pull one yarn out highly depends on the specimen length and transverse preload. An analytical model can be used to simulate the force-displacement response of the yarn uncrimping and subsequent yarn translation. The maximum shear strength and frictional shear strength were obtained by fitting the simulation response to the experimental results. Both shear strength parameters depend on the specimen size and the level of transverse preload.

While modest progress has been made in improving the predictive capabilities of the Kevlar material model via new experiments and changes to the constitutive model, further improvements are possible. These improvements are listed below.

- Picture-Frame Shear Test. The shear modulus behavior is based on results from picture-frame shear tests. The shear resistance increases with an increase in shear strain. At low shear strains, the fabric has little resistance to shear deformation. The yarns rotate and the warp and fill directions are no longer orthogonal. At some point, there is a very rapid increase in the shear stress value. This is caused by the re-orientation and packing of the

fabric yarns as the shear strain increases. Close examination of the fabric's deformation during the picture-frame tests revealed that the fabric was wrinkling at the edges during the initial stages of loading and experienced buckling during the final stages of loading. Further tests and examination of the results are necessary to understand and improve the shear behavior predictive capability of the model.

- Biaxial Test. It is assumed that the stress-strain relationships are decoupled so that any stress component is a function of only one strain component. In other words, the in-plane behavior of the fabric is not a function of the Poisson's effect. Limited fabric tests have shown that if the fabric is held in the fill direction and a load is applied in the warp direction, stresses develop in the fill direction. More thorough biaxial tests are necessary to gage the Poisson's effect to obtain rational continuum-equivalent values of Poisson's ratio covering the various behavioral zones in a fabric swatch, i.e., crimp, pre-peak, post-peak, and ultimately, failure.

- High Strain Rate Test. Little information is available on the strain rate behavior of Kevlar 49. The strain rate behavior used in the current model was based on published data where strain rates up to 1500/s are considered. Results from finite element analysis show that fabrics are subjected to strain rates as high as 20,000/s for very short durations, and 5,000-10,000/s can exist for much longer durations. More tests in both the intermediate strain rate regime (500-1,500/s) and the high strain rate regime (10,000-20,000/s) are necessary to understand how Kevlar fabrics behave under a high rate of loading.

6. REFERENCES.

1. Rajan, S.D., Mobasher, B., Sharda, J., Yanna, Y., Deenadayalu, D., Lau, D., and Shah, D., "Explicit Finite Element Modeling of Multilayer Composite Fabric for Gas Turbine Engine Containment Systems, Part 1: Static Tests and Modeling." FAA report DOT/FAA/AR-04/40,P1, November 2004.

2. Pereira, J.M. and Revilock, D.M., "Explicit Finite Element Modeling of Multilayer Composite Fabric for Gas Turbine Engine Containment Systems, Part 2: Ballistic Impact Testing," FAA report DOT/FAA/AR-04/40,P2, November 2004.

3. Simons, J., Erlich, D., and Shockey, D., "Explicit Finite Element Modeling of Multilayer Composite Fabric for Gas Turbine Engine Containment Systems, Part 3: Model Development and Simulation of Experiments," FAA report DOT/FAA/AR-04/40,P3, November 2004.

4. Gomuc, R., "Explicit Finite Element Modeling of Multilayer Composite Fabric for Gas Turbine Engine Containment Systems, Part 4: Model Simulation for Ballistic Tests, Engine Fan Blade-Out and Generic Engine," FAA report, DOT/FAA/AR-04/40,P4, November 2004.

5. Rajan, S.D., Mobasher, B., Sankaran, S., Naik, D., and Stahlecker, Z., "Explicit Finite Element Modeling of Multilayer Composite Fabric for Gas Turbine Engine Containment

Systems, Phase II, Part 1: Fabric Material Tests and Modeling," FAA report DOT/FAA/AR-08/37,P1, February 2009.

6. Simons, J., Erlich, D., and Shockey, D., "Explicit Finite Element Modeling of Multiayer Composite Fabric for Gas Turbine Engine Containment Systems, Phase II, Part 3: Material Model Development and Simulation of Experiments," FAA report DOT/FAA/AR-08/37,P3, February 2009.

7. Vintilescu, I.V., "Explicit Finite Element Modeling of Multilayer Composite Fabric for Gas Turbine Engine Containment Systems, Phase II, Part 4: Model Simulation for Ballistic Tests, Engine Fan Blade-Out, and Generic Engine," FAA report DOT/FAA/AR-08/37,P4, February 2009.

8. Zohdi, T.I. and Powell, D., "Multiscale Construction and Large-Scale Simulation of Structural Fabric Undergoing Ballistic Impact," *Computer Methods in Applied Mechanics and Engineering*, Vol. 195, 2006, pp. 94-109.

9. Verzemnieks, J., "Lightweight Ballistic Protection of Flight-Critical Components on Commercial Aircraft, Part 3: Zylon Yarn Tests," DOT/FAA/AR-04/45,P3, July 2005.

10. Zohdi, T.I. and Steigmann, D.J., "The Toughening Effect of Microscopic Filament Misalignment on Macroscopic Fabric Response," *International Journal of Fracture*, Vol. 115, 2002, pp. L9–L14.

11. Shockey, D.A., Elrich, D.C., and Simons, J.W., "Improved Barriers to Turbine Engine Fragments: Interim Report II," DOT/FAA/AR-99/8, II, May 1999.

12. Schwartz, P., Wagner, H.D., and Phoenix, S.L., "A Study of Statistical Variability in the Strength of Single Aramid Filaments," *Journal of Composite Material*, No. 18(4), 1984, pp. 312-338.

13. Schwartz, P., Netravali, A., and Sembach, S., "Effects of Strain Rate and Gauge Length on the Failure of Ultra-High Strength Polyethylene Fibers," *Textile Research Journal*, Vol. 56, 1986, pp. 502-508.

14. Wagner, H.D., Aronhime, J., and Marom, G., "Dependence of Tensile Strength of Pitch-Based Carbon and Para-Aramid Fibres on the Rate of Strain," *Proceeding of the Royal Society of London*, A428, 1990, pp. 493-510.

15. Amaniampong, G. and Burgoyne, C.J., "Statistical Variability in the Strength and Failure Strain of Aramid and Polyester Yarns," *Journal of Material Science*, Vol. 29, 1994, pp. 5141-5152.

16. Sharda, J., Deenadayalu, C., Mobasher, B., and Rajan S.D., "Modeling of Multilayer Composite Fabrics for Gas Turbine Engine Containment Systems," *ASCE Journal of Aerospace Engineering*, Vol. 19, No. 1, 2006, pp. 38-45.

17. Xia, Y. and Wang, Y., "The Effects of Strain Rate on the Mechanical Behaviour of Kevlar Fibre Bundles: An Experimental and Theoretical Study," *Composites Part A*, Vol. 29A, 1999, pp. 1411-1415.

18. Mulkern, T.J. and Raftenberg, M.N., "Kevlar KM2 Yarn and Fabric Strength Under Quasi-Static Tension," Army Research Laboratory, 2002, ARL-TR-2865, AD-A408883.

19. Yang, H.H., *Kevlar Aramid Fiber*, Chichester, U.K.: John Wiley, 1993.

20. Cheng, M. and Chen, W., "Mechanical Properties of Kevlar® KM2 Single Fiber," *Journal of Engineering Material and Technology*, Vol. 127, No. 2, 2005, pp. 197-203.

21. Farsi, D.B., Nemes, J.A., and Bolduc, M., "Study of Parameters Affecting the Strength of Yarns," *Journal de Physique IV*, Vol. 134, France, 2006, pp. 1183-1188.

22. Termonia, Y., "Impact Resistance of Woven Fabrics," *Textile Research Journal*, Vol. 74, No. 8, 2004, pp. 723-729.

23. Godfrey, T.A. and Rossettos, J.N., "The Onset of Tear Propagation at Slits in Stressed Uncoated Plain Weave Fabrics," *Journal of Applied Mechanics-Transactions of the ASME*, Vol. 66, No. 4, 1999, pp. 926-933.

24. Sebastian, S.A.R.D., Bailey, A.I., Briscoe, B.J., and Tabor, D., "Effect of a Softening Agent on Yarn Pullout Force of a Plain Weave Fabric," *Textile Research Journal*, Vol. 56, 1986, pp. 604-611.

25. Motamedi, F., Bailey, A.I., Briscoe, B.J., and Tabor, J., "Theory and Practice of Localized Fabric Deformations," *Textile Research Journal*, Vol. 59, 1989, pp. 160–172.

26. Martinez, M.A., Navarro, C., Cortes, R., and Rodriguez, J., and Sanchez-Galvez, V., "Friction and Wear Behaviour of Kevlar® Fabrics," *Journal of Materials Science*, Vol. 28, 1993, pp. 1305–1311.

27. Pan, N. and Yoon, M., "Behavior of Yarn Pullout From Woven Fabrics: Theoretical and Experimental," *Textile Research Journal*, Vol. 63, No. 11, 1993, pp. 629-637.

28. Bazhenov, S., "Dissipation of Energy by Bulletproof Aramid Fabric," *Journal Materials Science*, Vol. 32, 1997, pp. 4167-4173.

29. Kirkwood, M.K., Kirkwood, J.E., Lee, Y.S., Egres, R.G., and Wagner, N.J., "Yarn Pullout as a Mechanism for Dissipation of Ballistic Impact Energy in Kevlar® KM-2 Fabric, Part I: Quasi-Static Characterization of Yarn Pullout," *Textile Research Journal*, Vol. 74, No. 10, 2004, pp. 920-928.

30. King, M.J., "An Energy-Based Constitutive Model for the In-Plane Mechanical Behavior of Woven Fabrics," M.S. Thesis, Massachusetts Institute of Technology, 2003.

31. King, M.J., Jearanaisilawong, P., and Socrate, S., "A Continuum Constitutive Model for the Mechanical Behavior of Woven Fabrics," *International Journal of Solids and Structures*, Vol. 42, 2004, pp. 3867-3896.

32. King, M.J., "A Continuum Constitutive Model for the Mechanical Behavior of Woven Fabrics Including Slip and Failure," Ph.D. Thesis, Massachusetts Institute of Technology, 2006.

33. Naaman, E.A., Namur, G.G., Alwan, J.M., and Najm, H.S., "Fiber Pullout and Bond Slip I: Analytical Study," *Journal of Structural Engineering*, Vol. 117, 1991, pp. 2769-2790.

34. Naaman, E.A., Namur, G.G., Alwan, J.M., and Najm, H.S., "Fiber Pullout and Bond Slip II: Experimental Validation," *Journal of Structural Engineering*, Vol. 117, 1991, pp. 2791-2800.

35. Sueki, S., Soranakom, C., Mobasher, B., and Peled, A., "Pullout-Slip Response of Fabrics Embedded in a Cement Paste Matrix", *Journal of Materials in Civil Engineering*, Vol. 19, No. 9, 2007, pp. 718-727.